Springer Theses
Recognizing Outstanding Ph.D. Research

Anoop Kumar Singh

High Resolution Palaeoclimatic Changes in Selected Sectors of the Indian Himalaya by Using Speleothems

Past Climatic Changes Using Cave Structures

Springer

Springer Theses

Recognizing Outstanding Ph.D. Research

Aims and Scope

The series "Springer Theses" brings together a selection of the very best Ph.D. theses from around the world and across the physical sciences. Nominated and endorsed by two recognized specialists, each published volume has been selected for its scientific excellence and the high impact of its contents for the pertinent field of research. For greater accessibility to non-specialists, the published versions include an extended introduction, as well as a foreword by the student's supervisor explaining the special relevance of the work for the field. As a whole, the series will provide a valuable resource both for newcomers to the research fields described, and for other scientists seeking detailed background information on special questions. Finally, it provides an accredited documentation of the valuable contributions made by today's younger generation of scientists.

Theses are accepted into the series by invited nomination only and must fulfill all of the following criteria

- They must be written in good English.
- The topic should fall within the confines of Chemistry, Physics, Earth Sciences, Engineering and related interdisciplinary fields such as Materials, Nanoscience, Chemical Engineering, Complex Systems and Biophysics.
- The work reported in the thesis must represent a significant scientific advance.
- If the thesis includes previously published material, permission to reproduce this must be gained from the respective copyright holder.
- They must have been examined and passed during the 12 months prior to nomination.
- Each thesis should include a foreword by the supervisor outlining the significance of its content.
- The theses should have a clearly defined structure including an introduction accessible to scientists not expert in that particular field.

More information about this series at http://www.springer.com/series/8790

Anoop Kumar Singh

High Resolution Palaeoclimatic Changes in Selected Sectors of the Indian Himalaya by Using Speleothems

Past Climatic Changes Using Cave Structures

Doctoral Thesis accepted by
the Kumaun University, Uttarakhand, India

Springer

Author
Dr. Anoop Kumar Singh
Centre of Advanced Study (CAS)
in Geology
Kumaun University
Nainital, Uttarakhand
India

Supervisor
Prof. B. S. Kotlia
Centre of Advanced Study (CAS)
in Geology
Kumaun University
Nainital, Uttarakhand
India

ISSN 2190-5053 ISSN 2190-5061 (electronic)
Springer Theses
ISBN 978-3-319-73596-2 ISBN 978-3-319-73597-9 (eBook)
https://doi.org/10.1007/978-3-319-73597-9

Library of Congress Control Number: 2017962981

Printed on acid-free paper

This Springer imprint is published by Springer Nature
The registered company is Springer International Publishing AG
The registered company address is: Gewerbestrasse 11, 6330 Cham, Switzerland

Supervisor's Foreword

The Himalaya not only influences the rainfall pattern in India but also obstructs the path of the cold winds coming from the north because of altitude and location. The Inner Asian high-pressure systems and winter Westerlies are main components of the Himalayan climate, and a combined impact of rainfall, latitude, and altitude mainly affects the climate pattern. The region mainly experiences two seasons, i.e., summer (June to September) and winter (October to May). The Indian Summer Monsoon (ISM) decreases toward northwest India where Western Disturbances (WDs) play a major role in the annual precipitation. Therefore, the role of the WDs cannot be overlooked while using any archive or proxy for the past climatic changes in the Indian Himalaya. Taking this into account as well as knowing that the high-resolution palaeoclimatic records are scarce from the Indian Himalaya, Anoop Kumar Singh was given an assignment on high-resolution past climatic changes in selected sectors of the Indian Himalaya employing cave speleothems, particularly for the last ~15 ka period and undoubtedly the results should be very helpful to develop the models for ISM variability and WDs through an improved understanding of the monsoon–climate interaction.

The doctoral thesis encompasses study of six cave stalagmites, chronology of which was constructed on the basis of 35 U/Th and 5 AMS dates. Other proxies used were SEM analysis, XRD, and Mg/Ca ratio in order to differentiate calcite from aragonite, in addition to about 1500 samples for $\delta^{18}O$ and $\delta^{13}C$ isotopes for reconstructing past precipitation model. Three major events were identified, e.g., Older Dryas (OD), Bølling–Allerød (BA) period, and Younger Dryas (YD) at ca. 14.3–13.9, 13.9–12.7, and 12.7–12.2 ka BP, respectively. While comparing NW Himalayan record with Central Himalaya, there appears a similar trend in general but a shift in the duration of YD event, proving that the past climate of these two sectors also does not co-vary. The study also showed a gradual reduction in the precipitation from 4.0 ka BP onward for about a millennium with a peak arid period between 3.2 and 3.1 ka BP—a period correlated with fall of the Harappan–Indus civilization which finally collapsed due to severe scarcity of water reserves at 3.1 ka BP.

Considering very high variability in the $\delta^{18}O$ and $\delta^{13}C$ values, Anoop believes that the precipitation in the Himalayan foothills was a result of two sources of moisture and therefore he suggests that the WDs contributed significantly in the total rainfall during the Holocene period in the Indian Himalaya. This must be a reason for anti-correlation in the climatic pattern from Mid-Holocene onward between Himalaya and Peninsular India, the former received substantial precipitation from WDs.

Interestingly, the LIA in the Indian Himalaya was wetter compared to that in the post-LIA period. This is because during ISM break conditions, the moisture winds moved directly from the south to the Himalayan foothills and the WDs extended to the southern edge of the Tibet Plateau. As a result, during this period, the Himalayan southern slopes received high precipitation than the core monsoon zone.

I was deeply impressed by Anoop's excellent and matchless depth of understanding of the Holocene climatic process. During the doctoral programme, he visited several well-known laboratories in India and abroad as well as attended several training programmes to get skilled in this subject, refine his research, and get exposed to variety of climate archives and proxies.

Nainital, India
August 2017

Prof. B. S. Kotlia

Parts of this thesis have been published in the following journal articles:

1. Kotlia BS, Singh AK, Zhao J, Duan W, Tan M, Sharma AK, Raza W (2017) Stalagmite based high resolution precipitation variability for past four centuries in the Indian Central Himalaya: Chulerasim cave re-visited and data re-interpretation. Quaternary International 444 (A): 35–43
2. Kotlia BS, Singh AK, Sanwal J, Raza W, Ahmad SM, Joshi LM, Sirohi M, Sharma AK, Sagar N (2016) stalagmite inferred high resolution climatic changes through Pleistocene-Holocene transition in Northwest Indian Himalaya. Journal of Earth Science and Climate Change 7:3 http://dx.doi.org/10.4172/2157-7617.1000338
3. Kotlia BS, Singh AK, Joshi LM, Dhaila BS (2015) Precipitation variability in the Indian Central Himalaya during last ca. 4,000 years inferred from a speleothem record: Impact of Indian Summer Monsoon (ISM) and Westerlies. Quaternary International 371: 244–253
4. Joshi LM, Kotlia BS, Ahmad SM, Wu C-C, Sanwal J, Raza W, Singh AK, Shen C-C, Long T, Sharma AK (2017) Reconstruction of Indian monsoon precipitation variability between 4.0 and 1.6 ka BP using speleothem $\delta^{18}O$ records from the Central Lesser Himalaya, India. Arabian Journal of Geosciences http://dx.doi.org/10.1007/s12517-017-3141-7

Acknowledgements

For me, doing the research work was a real lifelong experience. This thesis is a crop of helping hands and support of a number of individuals. Foremost, I am extremely grateful to Prof. B. S. Kotlia for supervising the thesis and for being the driving force behind the present study. His cosmic supervision, motivation, support, and appreciation in every way was unforgettable.

I would like to convey my sincere thanks to Prof. A. K. Sharma, Head, Department of Geology, Kumaun University, Nainital for providing me the departmental facilities. I sincerely thank Prof. Santosh Kumar, Dean, Faculty of Science for his fruitful suggestions. I am pleased in recording my sincere gratitude to Director, CSIR-National Geophysical Research Institute, Hyderabad for providing the laboratory and other necessary facilities during the analytical procedures. My heartiest thanks to Prof. Augusto Mangini, University of Heidelberg (Germany) for providing most of the U/Th dates.

I gratefully acknowledge Dr. Lalit M. Joshi for his multiple help, emotional support, and constant backup that cannot be expressed in words. I am highly indebted to Mr. Bachi S. Dhaila for his kind support and encouragement during my research period. It is my great pleasure to express my sincere gratitude to Dr. Syed Masood Ahmad, Mr. Netramani Sagar, Mr. Waseem Raza, Mr. Tabish Raza from NGRI, Hyderabad, and Dr. Mahjoor Lone (presently at National Taiwan University Taipei, Taiwan) for their generous help during sample analysis. In addition, I express my sincere thanks to G. Suseela, Sadia Farnaaz, Shiva, Shivasis, and Santosh from NGRI, Hyderabad for helping me during the isotopic analysis. I am beholden to Prof. D. C. Pande (Registrar and Chief Warden Kumaun University, Nainital) for moral support and help in various ways in completing the thesis. I am also obliged to the ISRO, Ahmedabad for financial assistance. Additionally, I am also grateful to the MoES (MoES/P.O./Geosci/43/2015), New Delhi for the financial help during later half of my research period.

Nainital, India
August 2017

Anoop Kumar Singh

Contents

Abbreviations

$\delta^{18}O$	Stable oxygen isotope ratio ($^{18}O/^{16}O$) in a sample relative to that in a standard
$\delta^{13}C$	Stable carbon isotope ratio ($^{13}C/^{12}C$) in a sample relative to that in a standard
AMS	Accelerator Mass Spectrometry Radiocarbon Dating
ASM	Asian Monsoon System
BA	Bølling–Allerød
EASM	East Asian Summer Monsoon
EDS	Energy Dispersive X-ray Analysis
ENSO	El Niño–Southern Oscillations
GNIP	Global Network of Isotopes in Precipitation
IOD	Indian Ocean Dipole
ISM	Indian Summer Monsoon
ITCZ	Inter-Tropical Convergence Zone
LIA	Little Ice Age
LLJ	Low-Level Jet streams
Mg/Ca	Magnesium/Calcium ratio
NAO	North Atlantic Oscillation
OD	Older Dryas
SEM	Scanning Electron Microscope
U/Th	Uranium–Thorium dating
XRD	X-ray Diffraction
WDs	Westerlies or Western Disturbances
YD	Younger Dryas

Chapter 1
Introduction

Monsoon is one of the complex rain bearing features of Earth's climate. The Asian Monsoon System (ASM) is a large and most extensive monsoon pattern in the world as well as important component of global climate system (Morrill et al. 2006). It strongly affects most of the nations of south and south-east Asia. The ASM has two dominant monsoon patterns, e.g., East Asian Summer Monsoon (EASM) and Indian Summer Monsoon (ISM). The EASM is a monsoonal stream that carries wet air from the Indian and Pacific Oceans to East Asia and affects parts of Japan, Koreas, Taiwan, Philippines, Hongkong, Indo-china and much of mainland China (Webster et al. 1998; Trenberth et al. 2000; Ding and Chan 2005). It is derived by temperature difference between the Pacific Ocean and the Asian continent. The ISM pattern of the Indian subcontinent, different from the rest of Asia decides the economic and agricultural growth of India and its dramatic pattern and intensity are great challenge for climatologists to reconstruct the past climatic conditions and also future predictions.

The ISM arrives from southwest direction (Arabian Sea) to land, and brings rain to most parts of the Indian subcontinent (Rao 1976; Agnihotri et al. 2002; Gadgil 2003) during the months of June–September and contributes about 80% precipitation of the total annual rainfall (Gadgil 2003) while remaining is received from winter monsoon, e.g., North East monsoon (NE monsoon) and Westerlies (WDs). The ISM splits into two branches (Fig. 1.1), (i) The Arabian Sea branch and, (ii) Bay of Bengal branch. It is divided into three different streams on arriving in the mainland of India. The first stream strikes the elevated Western Ghats (Ananthakrishnan et al. 1967; Rao 1976; Ananthakrishnan and Soman 1988; Soman and Kumar 1993; Chakraborty et al. 2006; Rao et al. 2010; Goswami 2012) at almost right angle (Fig. 1.1) and provides extremely heavy rainfall. The second stream enters Narmada-Tapi troughs and reaches Central India. It does not cause much rain near the coast but is very much responsible for precipitation in the Indo-Gangetic Plains. The third stream moves in a North-Easterly route parallel to the Aravalli Range. Since the orientation of the Aravalli Range is parallel to the direction of prevailing monsoon winds, it does not offer a major blockage in Rajasthan. The Bay of Bengal branch is main cause of

A. K. Singh, *High Resolution Palaeoclimatic Changes in Selected Sectors of the Indian Himalaya by Using Speleothems*, Springer Theses,
https://doi.org/10.1007/978-3-319-73597-9_1

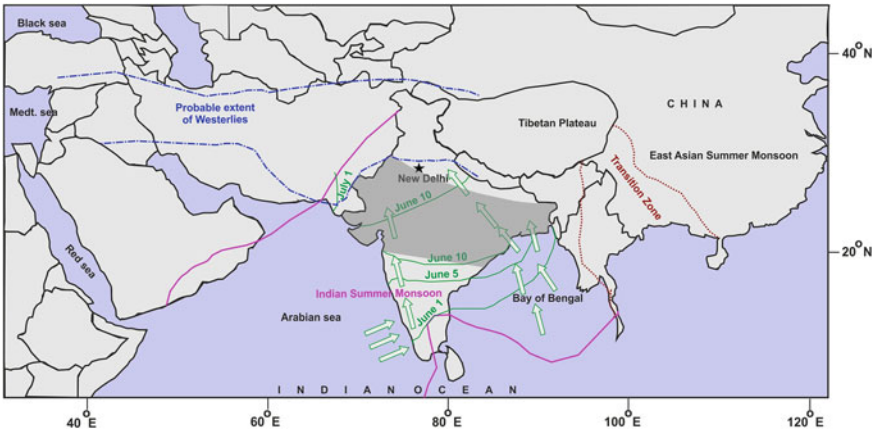

Fig. 1.1 Extent of present day ISM and WDs (after Kotlia et al. 2015)

precipitation in Northeast India and further moves towards the Indo-Gangetic Plain. It is divided into two distinct streams; first stream of Bay of Bengal branch hits the western coast of Burma where Arakan and Tenasserim mountains receive heavy rainfall (Gadgil 2003). Another southerly stream crosses the Ganga-Brahmaputra delta and reaches Meghalaya. This moves towards southern slopes of Assam hills. The rain bearing winds decrease from south to north and east to west.

The NE monsoon (October–December) brings rain to several places in south India (Prasad and Enzel 2006). The ISM withdraws from the extreme north-west end of the country in September, from the Peninsula by October and from the extreme south-eastern tip by December. The NE Monsoon contributes mainly to coastal Andhra Pradesh and Tamil Nadu-Pondicherry.

Westerlies or Western Disturbances (WDs) bring heavy rainfall/snow fall in low lying areas in western Himalayan region, particularly over Northwest India. The WDs are active in the winter months (November–February) and are important for Rabi crops (wheat). The WDs (between 30° and 60° latitude) originate mostly from the Mediterranean Sea and move eastward towards India across Afghanistan/Pakistan (Benn and Owen 1998; Kotlia et al. 2015). They split into two branches in Asia due to orographic barrier of the Himalaya and the Tibetan Plateau (Pang et al. 2014).

1.1 Indian Summer Monsoon (ISM) Variability

It is shown that the ISM rainfall over India occurs in intermittent spells of active and break cycles (Ramamurthy 1969; Sikka and Gadgil 1980; Krishnamurthy and Kinter 2003).

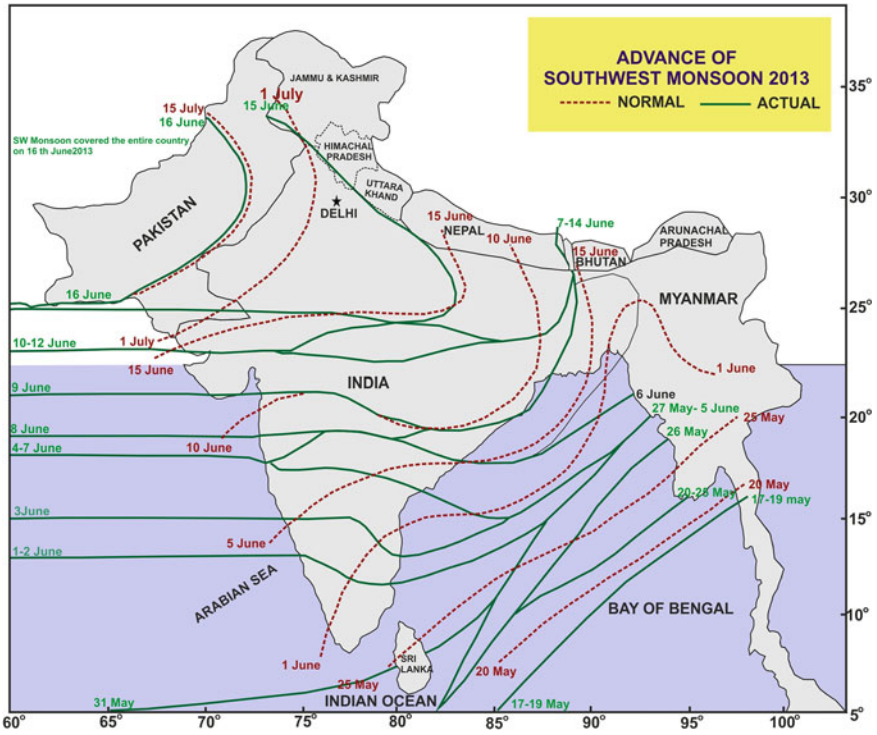

Fig. 1.2 Advance of the ISM within 15 days in the year 2013

The break spells or intervals of droughts (Sikka 1980) are described as interruption of several days in the peak ISM months. The active spells are defined as development of the ISM disturbances (wet and flood periods) in a short period (Murakami 1976). The ISM intensity depends on many parameters, e.g., coupled heating-cooling between land and sea, Inter-Tropical Convergence Zone (ITCZ), El Niño-Southern Oscillations (ENSO), North Atlantic Oscillations (NAO) etc. For example, the ISM covered the entire country before 15 days from regular schedule in the year 2013 (Fig. 1.2), during which several parts of North India (Uttarakhand) and NE India witnessed floods. It was an El Niňo year (Weaker monsoon year) but the amount of precipitation in June was totally different. Thus, it is very much difficult to predict the behaviour and intensity of monsoon. Some other examples are floods in Mumbai (2005), Uttarakhand (2013), Kashmir (2014) (Singh et al. 2014) and the droughts in NE India, Bihar and Jharkhand in 2013 (Indian Meteorological Department report 2013).

1.2 Origin of Monsoon over Indian Subcontinent

Three different traditional theories are related to the origin of the monsoon, e.g., Dynamic theory, Thermal Theory and Jet Stream Theory.

1.2.1 Dynamic Theory

The southeast trade winds of the Southern Hemisphere and the northeast trade winds of the Northern Hemisphere meet up each other near the Equator. The meeting place of these winds is known as the ITCZ which shifts north and south of Equator with the change of season (Gupta et al. 2003; Bookhagen et al. 2005). When the sun shines vertically (summer season) over the Tropic of Cancer then the ITCZ shifts (20°–25°N) northwards. Due to this behaviour, the ISM moves from the Arabian Sea and bring rains over the Indian subcontinent in the months of July–September. In winter, the ITCZ shifts towards Southern Hemisphere, thus the wind directions are inverted from the high pressure cell over the Tibetan Plateau in the northeast towards the Indian Ocean.

The NE monsoon is based on shift of the ITCZ southward (increased heating of Bay of Bengal) causing monsoon in Orissa, some of Andhra and Tamil Nadu regions in November–December. The variation of monsoon in the Indian subcontinent is a result of heating-cooling pattern between Himalaya and southern Indian Ocean (Hastenrath 1987; Webster 1987; Anderson and Prell 1993). Thus, there seems a complex link between the ISM and NE monsoons regarding their origin, behaviour and amount (Pant and Rupa Kumar 1997; Krishnamurthy and Shukla 2000; Krishnan et al. 2000; Krishna et al. 2005; Clift and Plumb 2008).

1.2.2 Thermal Theory

This is based on three physical processes. The first process is uneven temperature difference of land and sea (Chen et al. 2003), which causes a pressure differential that drives the winds from high pressure to low pressure. The rotary motion of earth which forces moving winds to turn towards the right in the Northern Hemisphere and to the left in Southern Hemisphere is the second physical process. Finally, the change in the state of water from liquid to vapour which determines the strength and location of the monsoon rains. The discharge of latent heat also acts as a significant role in forming the low pressure over the Thar Desert. In the thermal theory, the sun shines vertically over the Tropic of Cancer resulting in high temperature and low pressure on Indian subcontinent while the pressure is still sufficiently high over Arabian Sea and Bay of Bengal (Flohn 1957; Chang 2004; Wang 2006).

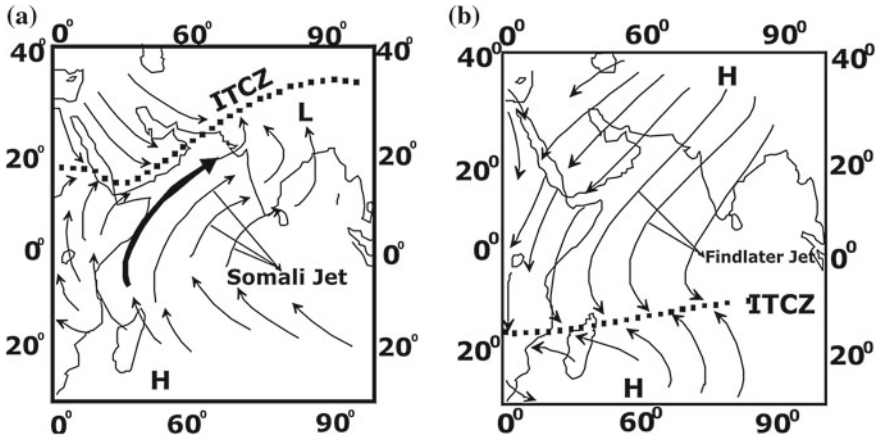

Fig. 1.3 **a** Behaviour of Somali Jet during summer, **b** Retreat of ISM with Findlater Jet in winter

For the NE monsoon, the origin conditions are reversed. The high pressure system develops over Kashmir and Punjab and the low pressure centre is formed over the Indian Ocean and Arabian Sea. Thus the winds move from land to sea and these are NE monsoon (Ramaswamy 1972; Dhar and Rakhecha 1983; Singh and Sontakke 1999; Balachandran et al. 2006) in Northern Hemisphere. The WDs originate from high pressure zones near mid-latitudes (Mediterranean Sea) towards poles. But by the Coriolis effect, these winds become south WDs in Northern Hemisphere and encounter the NW India and Himalaya.

1.2.3 Jet Stream Theory

Jet stream is a group of fast moving air mass from west to east, usually found in the middle latitudes in the upper troposphere (height of about 12 km). The Low Level Jet streams (LLJ) are fast moving narrow belts within heights of 2–3 km from surface (Bunker 1965; Li et al. 2004). Findlater (1969) made a detailed study of LLJ near Equator. The LLJ originates from Madagaskar and crosses Kenya coast, Ethopia, Somalia and Arabian Sea. It transports moisture to the Indian subcontinent (Joseph and Raman 1966; Findlater 1969) during the ISM period. This LLJ is also known as East African Low level jet or Somali Jet. The Somali Jet is low level jet (Fig. 1.3a) stream runs along the coast of Somali and Oman (Joseph and Raman 1966) in the western Indian Ocean.

The Somali Jet monsoon wind that is deflected to the north as it crosses the Equator is further deflected to the east by the mountains of Africa. The Somali Jet affects the precipitation pattern of the ISM and NE monsoons. The increase of the ISM (Arabian Sea) towards Indian subcontinent is greatly aided by the onset of the Somali Jet. It

strengthens enduring high near Madagascar and also assists to drive the ISM towards India at a greater intensity. The strange feature of the Findlater Jet (Findlater 1969) is reversal in direction with the arrival of the summer monsoon. In winter, this current is from north to the south from the coast of Arabia to the east African coastline.

The Findlater Jet (Fig. 1.3b) is also a narrow low-level jet that develops after the duration of the ISM. At the center of this jet, the transport is maximum and decreases to the right and left with increasing distance (Findlater 1969). Towards the left of the jet center, there is less water movement towards the center than is leaving, creating a divergence in the upper layer and resulting in an upwelling event. The NE monsoon is active from December to February due to the effect of the Findlater Jet.

1.3 Important Teleconnections with ISM Variability

The ISM has capacity to interact with other modes of the climate variability. The most important teleconnections related to ISM variability are, the El Niño Southern Oscillations (ENSO), Indian Ocean Dipole (IOD), and the North Atlantic Oscillations (NAO) (Krishnan et al. 2009; Menzel et al. 2013; Prasad et al. 2014).

1.3.1 El Niño-Southern Oscillations (ENSO)

The ENSO cycle describes the fluctuations in temperature between the atmospheres in the east-central equatorial Pacific. This cycle has two opposite phases, El Niño and La Niña, El Niño as the warm phase (Rasmussen and Carpenter 1983) and La Niña as the cold phase. The El Niño is large-scale periodic warming in sea surface temperatures across the central (Fig. 1.4) and east-central equatorial Pacific. The La Niña represents the period of below-average sea surface temperatures across the east-central equatorial Pacific.

The El Niño, is one of the important parameters, noted to influence the ISM over India (Sikka 1980; Rasmussen and Carpenter 1983; Shukla and Paolino 1983; Webster and Yang 1992; Meehl and Arblaster 2002). The Indian subcontinent drought years are related with El Niño and La-Nina is related with floods. Researchers suggest that the effect of El Niño to the ISM has weakened during recent decades (Kumar et al. 1999; Sudipta et al. 2004). The ISM relationship with various parameters has guide to investigate new relationship with intensity and amount (Dugam and Kakkade 2004; Munot and Krishna 2007).

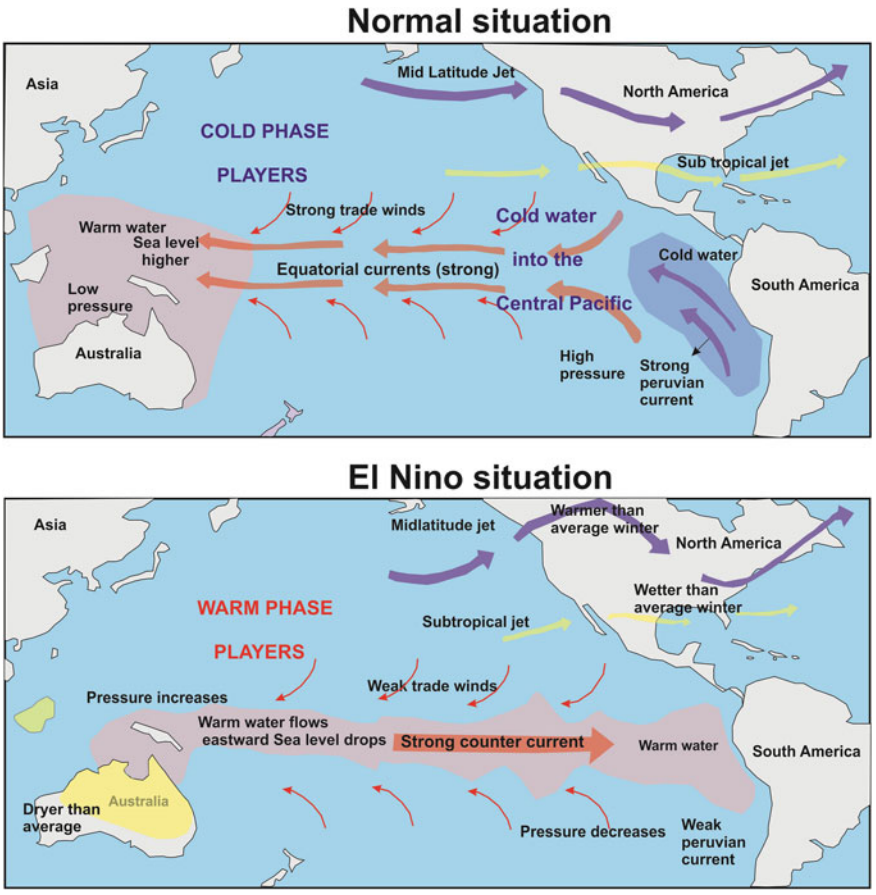

Fig. 1.4 Relationship between the ISM and El Niño

1.3.2 North Atlantic Oscillations (NAO)

The NAO is a large-scale pattern of natural climate variability that has important impacts on the weather and climate of the North Atlantic region. A number of studies have suggested that the NAO is related to the ISM variability (Dugam et al. 1997; Kakade and Kulkarni 2012). It is observed that April NAO index has negative correlation with the ISM of concurrent year (Kakade and Dugam 2000). The decadal scale analysis shows that the NAO during winter (December–January–February) and spring (March–May) has an inverse relationship with the ISM rainfall of Northwest India and Peninsular India. The highest correlation is observed with the winter NAO. The NAO and Northwest India rainfall relationship is stronger than that for the Peninsular India rainfall.

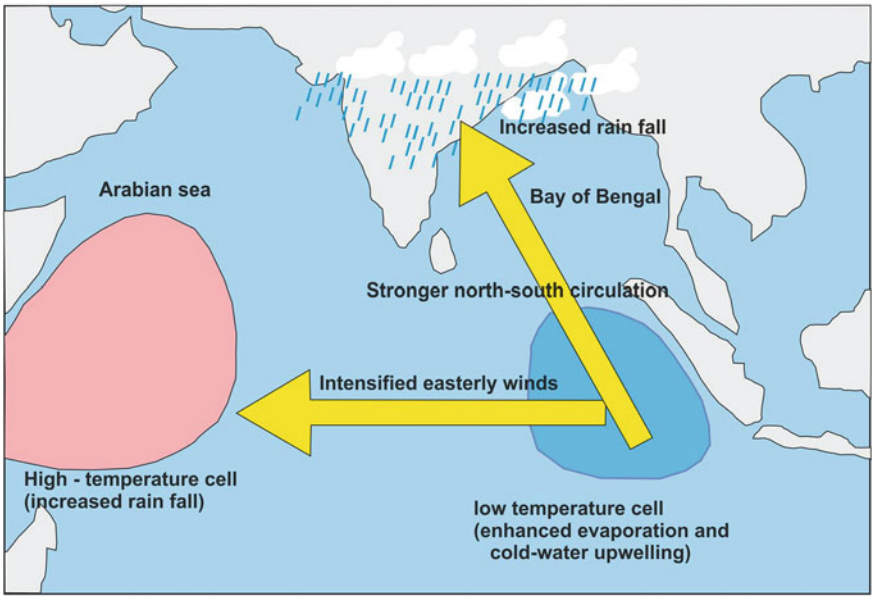

Fig. 1.5 Summer condition during a positive IOD and its relation with ISM

1.3.3 Indian Ocean Dipole (IOD)

The ISM is affected by the system of oscillating sea surface temperature known as IOD. In the IOD, western Indian Ocean becomes alternatively warmer than the colder eastern part of the ocean (Saji et al. 1999). A positive IOD (Fig. 1.5) leads to greater ISM rainfall while negative IOD leads to less rainfall or ISM breaks. The IOD is important factor that occurs inter-annually in the tropical Indian Ocean and which affects the ISM behaviour (Ashok et al. 2001). The correlation of the ISM rainfall with ENSO is low, but with the IOD is high (Yamagata et al. 2004). The IOD event not only affects the zonal (east-west) circulation in the troposphere, but also impacts on the meridional (North-South) circulation. During a typical El Niño period, the amount of precipitation accompanying the ISM is reduced, but a positive dipole mode event counteracts this effect when they occur together.

1.4 Himalayan Climate and Its Difference from Core Monsoon Zone

The uplift of Himalayan and Tibetan plateau is argued to have had profound effect on the global climate throughout late Cenozoic times due to mechanical, thermal and weathering effects (Ruddiman and Kutzbach 1989). The vast area of high ground exerts an important influence on regional and global climate in several ways

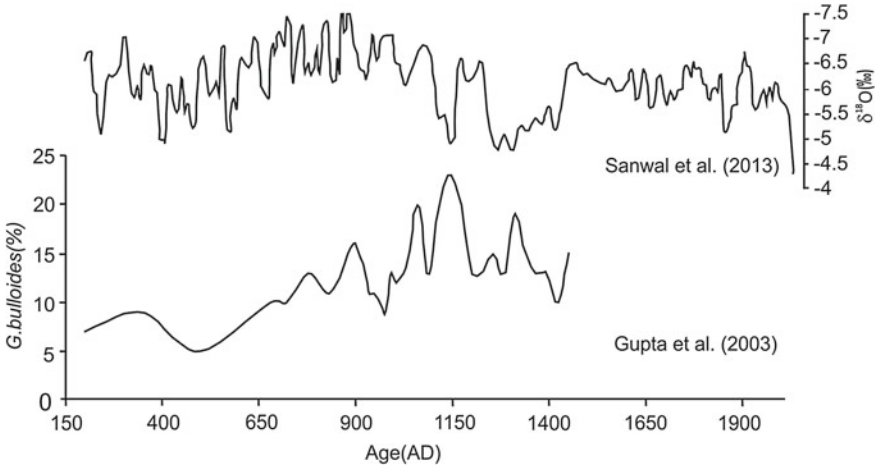

Fig. 1.6 Records from Arabian Sea $\delta^{18}O$ (Gupta et al. 2003) and stalagmite $\delta^{18}O$ records from Himalayan foothills (Sanwal et al. 2013) for the similar time bracket. The data show negative correlation

(Murakami 1987) and acts as barrier to atmospheric circulation for both ISM and the WDs. The Himalaya represents the sub tropical climate to Alpine climate from foot hills to higher mountain ranges. The ISM response over the Himalaya has not been completely linear (Overpeck et al. 2005). Therefore, this region demonstrates a great variability and is representative of precipitation over the entire Indian subcontinent.

Recent high resolution researches have shown that the Holocene climate of the Indian Himalaya displays anti-correlation with that of the Peninsular India. For, example, the Holocene ocean data from Arabian sea (Anderson et al. 2002; Gupta et al. 2003) show anti-correlation with Himalayan stalagmite record (Fig. 1.6). Various researchers have ascribed this difference as the significant role of WDs in the Himalaya. The $\delta^{18}O$ records of Valmiki Cave (influenced by the ISM; Lone et al. 2014) and Kalakot Cave (Northwest Himalaya; Kotlia et al. 2016) further show anti-correlation (Fig. 1.7) with each other. This means that the Holocene climate of the areas, influenced by single monsoon may show negative correlation with the sites influenced by two sources of moisture (e.g., Kotlia et al. 2015, 2016, 2017).

1.5 ISM and WDs in Himalaya

The Himalaya has a topographic, variability from south to north and east to west with a local scale weather pattern (Dimri and Niyogi 2012; Dimri et al. 2013). The Himalaya is situated at the northern boundary of ISM. The WDs are responsible for fog, rains, snow and avalanches. They are active in Himalaya mostly over Uttarakhand, Himachal Pradesh and Jammu and Kashmir and are important for

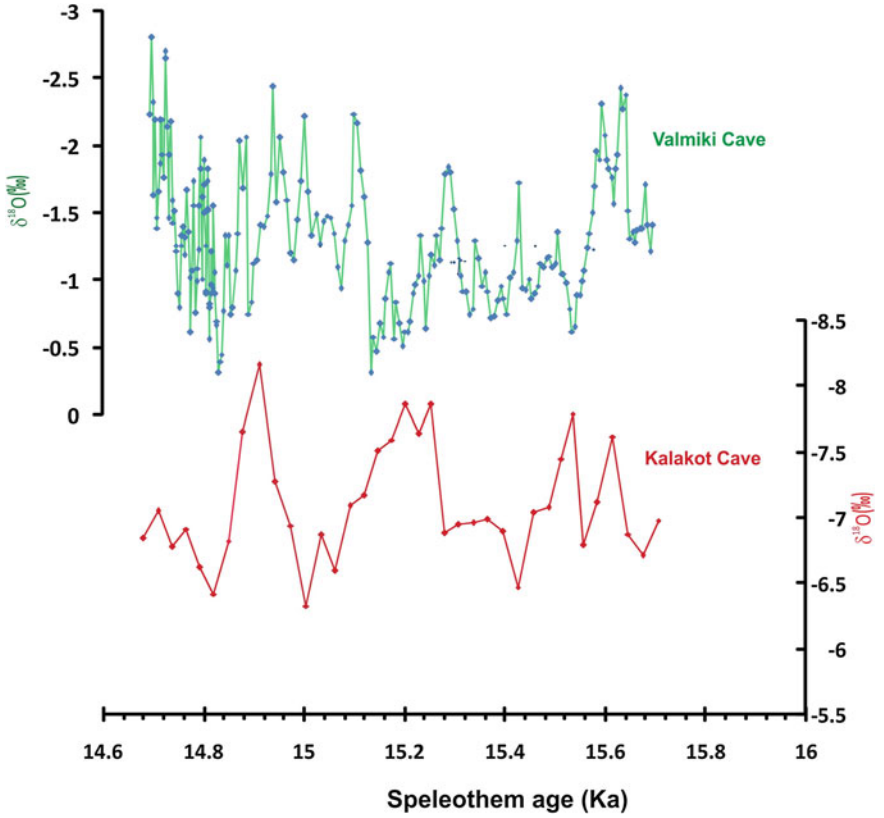

Fig. 1.7 Comparison of $\delta^{18}O$ records of Valmiki Cave (Peninsular India) (Lone et al. 2014) and Kalakot Cave (Himalaya record) (Kotlia et al. 2016) during similar time period. Note the anti-correlation

agriculture, glaciers and basins that feed the rivers. However, even within the Himalaya from east to northwest the climate is not linear (Fig. 1.8) largely because of more significant role of the WDs towards northwest (e.g., Kashmir).

1.6 Previous Palaeoclimatic Research in Brief in Indian Himalaya and Adjoining Areas

In the Indian Himalaya, a number of researchers have reconstructed palaeoclimatic changes by using archives such as lake sediments, peat deposits, pollen, tree rings and glaciers. From Kumaun Himalayan region, Quaternary lake record was first studied by Kotlia et al. (1997) by using multi-proxies techniques in Bhimtal-Naukuchiatal area. Subsequently, the Wadda and Riyasi lakes (Kotlia and Phartiyal 1999; Kotlia

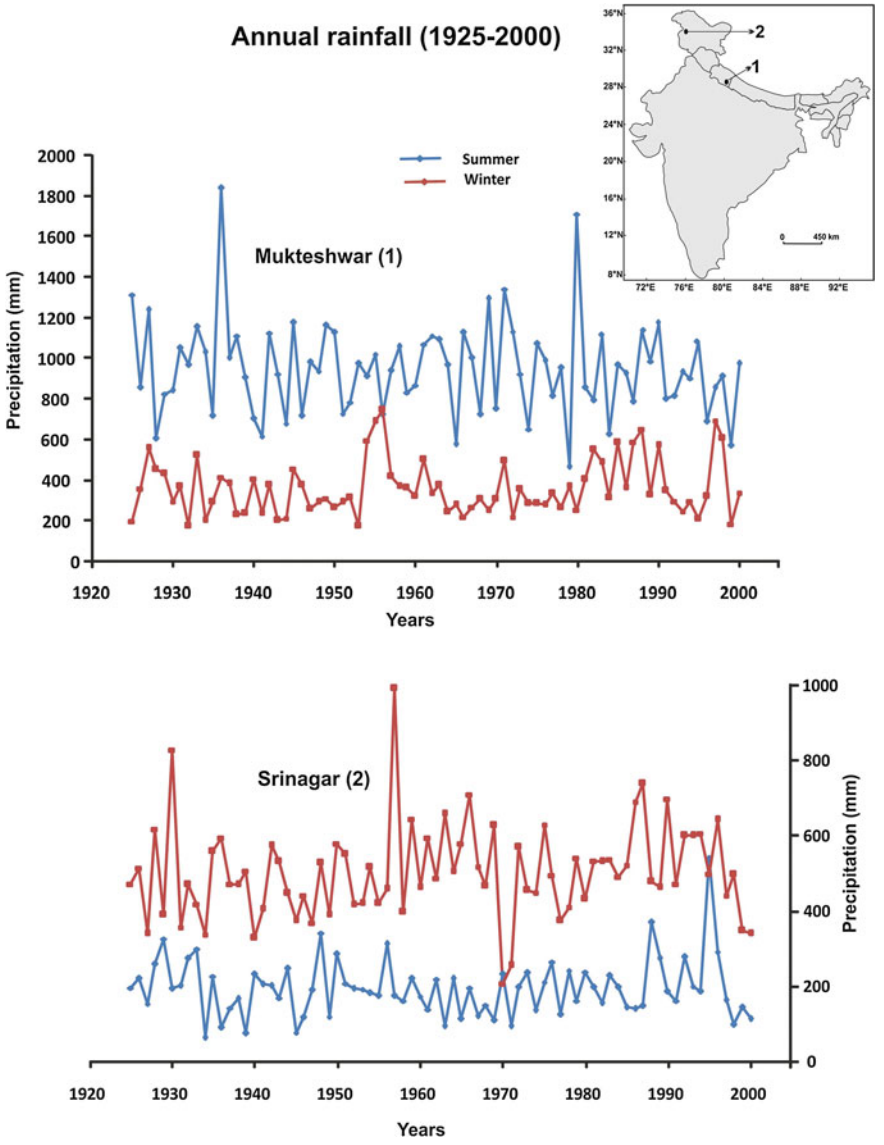

Fig. 1.8 Comparision of precipitation variability in the Himalaya from eastern part (Mukteshwar) to northwest (Srinagar). Data from Indian Meteorological Department

et al. 2000; Phartiyal et al. 2002, 2003) of Pithoragarh were studied from the view point of the climatic changes for Late Pleistocene-Holocene. The mineral magnetic study carried out by Kotlia and Sanwal (2004) in Dulam area indicate a number of arid and humid phases between 32 and 22 ka BP. Kotlia and Rawat (2004) reported

major climatic events of Holocene from Garbyang palaeolake. The magnetic susceptibility and sedimentological investigations of Garbyang paleolake provide climatic fluctuations between 20 and 10 ka BP with a prominent phase of Younger Dryas (YD) event between 12 and 11 ka BP with (Juyal et al. 2004). Kotlia et al. (2010) studied a lake profile from Champawat district covering the last 20 ka BP along with major climatic events such as Last Glacial Maximum (LGM), Older Dryas (OD), YD, 8.2 and 4.2 ka event.

Similarly, Garhwal Himalaya has been explored for Holocene climatic changes (Sharma and Gupta 1995, 1997; Chauhan et al. 1997). The climatic study on lacustrine sediments of Goting basin, Garhwal Himalaya revealed several pulses of cold and wet phases between 40 and 13 ka BP (Pant et al. 1998; Juyal et al. 2009). A study on a 1.8 m long core from subtropical belt of Garhwal Himalaya (Chauhan and Sharma 2000) indicated cool and dry climate from 2.5 to 2.3 ka BP. Another record from Garhwal Himalaya covers last 4 ka BP with wet (4–3.2 ka BP) and dry (3.2–1.7 ka BP) phases (Sharma et al. 2000). Pollen and magnetic susceptibility of Uttarkashi peat bog sediments indicate two phases of high precipitation at 7.8–5 ka BP and 6–4.5 ka BP (Phadtare 2000). The pollen records of the Pinder valley illustrate the precipitation weakening event at 3.5–2.3 ka BP (Rühland et al. 2006). Geochemical record of Rudraprayag palaeolake documents major climatic events, e.g., 4.2 ka event, Medieval warm period (MWP) and Little Ice Age (LIA) (Kotlia and Joshi 2013). Srivastava et al. (2013) investigated Malari palaeolake profile and revealed four phases of high monsoon intensity at ~11.5 ka BP, 11–10 ka BP, 10–9 ka BP and 8–7 ka BP. Recently, a detailed study of a modern lake core by Demske et al. (2016) suggested a combined effect of both ISM and WDs during the MWP (AD 500–1100) and LIA (AD 1400–1630). All these records represent millennial to centennial scale climatic changes but don't show decadal to multi-decadal scale changes.

In other parts of the Indian Himalaya, Bookhagen et al. (2005) explored Sutlej valley and suggested two ISM intensified phases at 29–24 and 10–4 ka BP. A more detailed study of late Holocene lake from Himachal Pradesh reveals a cold/dry phase (2.3–1.5 ka BP) and a warm/moist phase (1.5–0.9 ka BP) (Chauhan et al. 2000). Mazari et al. (1995) documented some cold dry phases between 2 and 1 ka BP in the spiti region. Chauhan (2006) investigated peat bogs in Lahaul-Spiti and found warm and moist phases between 1.3 and 0.5 ka BP. Anoop et al. (2013) studied a Holocene lake in Spiti and documented ISM break at 7.6–6.8 ka BP and strong phase of precipitation between 6.8 and 6.1 ka BP. A well dated post glacial lake profile of Lahaul-Spiti demonstrates the climatic fluctuations between 9.5 and 13 ka BP and their relationship with ISM intensity (Rawat et al. 2012, 2015). Recently, Bohra and Kotlia (2015) studied a 25 ka BP old lake profile in Lahaul-Spiti and documented the combined effect of ISM and WDs between 12 and 5 ka BP.

Further west and northwest, an important study on Tethyan Himalayan sediments of eastern Ladakh has revealed alternation of moist and wet phases for the last 30 ka BP (Bhattacharyya 1989). Demske et al. (2009) established palynology of Tso Kar lake for the last 15 ka BP and suggested that this area experienced several wet and dry phases with the combined effect of both monsoon regimes (ISM and WDs). Wünnemann et al. (2008, 2010) systematically explored Tso Kar Lake and obtained

results for the last 15 ka BP with high ISM intensity events (12.5, 11.5 and 8.6 ka BP) and dry phases (8–6 and 4.2 ka BP). Leipe et al. (2014) reported a well dated lake profile of Tso Moriri (12 ka BP) with wet (11.5–4.5 ka BP) and dry phases (4.5–1.9 ka BP). Tangtse valley deposits of Ladakh region reflects the wet (9.6–5.1 ka BP) and dry (30–21 ka BP) phases (Phartiyal et al. 2015). The isotopic investigations in the Tso Moriri lake show dramatic fluctuations during glacial and early Holocene including two wet phases (13.2–11.7 ka BP and 11.2–8.5 ka BP) (Mishra et al. 2015). From western Tibet area, Gasse et al. (1991) studied a lake record of the last 13 Ka BP with warm and humid pulses (12.5–10 ka BP). Gasse et al. (1996) also investigated a lake profile and documented a few high precipitation stages from 9.5–8.7 ka BP to 7.2–6.3 ka BP.

Tree ring width chronology of Himalayan conifers has helped document the short term past climatic changes. From Garhwal Himalaya, a relationship between tree ring width and glacial fluctuations has been established (Borgaonkar et al. 1994, 1999; Bhattacharyya et al. 2006). Singh and Yadav (2005) documented western Himalaya cedar record between AD 1897–1986 and climatic relationship with ISM records. Based on several conifer increment cores from western Himalaya, the climatic picture of the last about four hundred years is well studied (Singh et al. 2006). Subsequently, cedar records of Kinaur show that the 18th century was driest and 20th century was the wettest period (Singh et al. 2009). Some other tree ring records of Kinaur since AD 1353 show a relationship of precipitation with NAO and ENSO (Yadav et al. 2010; Yadav 2013). A detailed study of Juniper tree species from western Himalaya reflect 11–15th century as warm period and 18–19th century as cold period (Yadav 2011a, b). A western Himalaya tree ring records since 1171 AD reveals a number of climatic events such as LIA and MWP (Yadav and Park 2000; Yadav and Bhutiyani 2013). Lately the Kumaun Himalayan cedar record from Jageshwar (AD 1668–2012) and Gangolihat (AD 1536–2012) reveal a relationship of precipitation with crop productivity (Yadav et al. 2015). Yadava et al. (2016) have also documented a tree ring record of the last 2000 years from Himachal Pradesh that supports the role of WDs in the Himalaya and their effect on the MWP and LIA.

Few glaciers and glacier-snow covered regions in the Himalayas and Tibetan Plateau are studied (Kulkarni et al. 2005; Raina and Sangewar 2007; Upadhyay 2009), Gangotri Western Himalayas (Jain 2008), Himachal region (Berthier 2007), Chenab Glacier (Kulkarni et al. 2007), showing glacial retreat due to global warming. In the Himalaya, most ice cores were studied over the Tibetan plateau, Dasuopu Glacier the Central Himalaya (Thompson et al. 1989, 1990, 2000) and Southern Tibet East, Rongbuk glacier. These studies have provided a wide range of climatic and environmental records (Kang et al. 2002; Hou et al. 2003, 2013; Xu et al. 2007; Kaspari et al. 2008; Zhang et al. 2009; Lee et al. 2011).

References

Agnihotri R, Dutta K, Bhushan R, Somayajulu BLK (2002) Evidence for solar forcing on the Indian monsoon during the last millennium. Earth Planet Sci Lett 198:521–527

Ananthakrishnan R, Soman MK (1988) The onset of southwest monsoon over Kerala for the period 1870–1990. Int J Climatol 9:283–296

Ananthakrishnan R, Acharya UR, Ramakrishnan AR (1967) On the criteria for declaring the onset of the southwest monsoon over Kerala. Forecasting manual, FMU Report, India Meteorological Department, Pune, India, 4(18.1), p 52

Anderson DM, Prell WL (1993) A 300 kyr record of upwelling off Oman during the late Quaternary: evidence of the Asian southwest monsoon. Paleoceanography 8:193–208

Anderson DM, Overpeck JT, Gupta AK (2002) Increase in the Asian southwest monsoon during the past four centuries. Science 297:596–599

Anoop A, Prasad S, Krishnan R, Naumann R, Dulski P (2013) Intensified monsoon and spatiotemporal changes in precipitation patterns in the NW Himalaya during the early-mid Holocene. Quatern Int 313–314:74–84

Ashok K, Guan Z, Yamagata T (2001) Impact of the Indian Ocean Dipole on the relationship between the Indian Monsoon rainfall and ENSO. Geophys Res Lett 26:4499–4502

Balachandran S, Asokan A, Sridharan S (2006) Global surface temperature in relation to northeast monsoon rainfall over Tamil Nadu. J Earth Syst Sci 115:349–362

Benn DI, Owen LA (1998) The role of the Indian summer monsoon and the mid-latitude westerlies in Himalayan glaciation: review and speculative discussion. J Geol Soc 155(2):353–363

Berthier E (2007) Dynamique et bilan de masse des glaciers de montagne (Alpes, Islande, Himalaya). Contribution de l'imagerie satellitaire. La Houille Blanche 2:116–121

Bhattacharyya A (1989) Vegetation and climate during the last 30,000 years in Ladakh. Palaeogeogr Palaeoclimatol Palaeoecol 73:25–38

Bhattacharyya A, Shah SK, Chaudhary V (2006) Would tree ring data of *Betula utilis* be potential for the analysis of Himalayan glacial fluctuations? Curr Sci 91:754–761

Bohra A, Kotlia BS (2015) Tectono-climatic signatures during Late Quaternary in the Yunam basin, Baralacha Pass (upper Lahaul valley, India), derived from multi-proxy records. Quatern Int 371:111–121

Bookhagen B, Thiede RC, Strecker MR (2005) Late Quaternary intensified monsoon phases control landscape evolution in the northwest Himalaya. Geology 33:149–152

Borgaonkar HP, Pant GB, Rupa Kumar K (1994) Dendroclimatic reconstruction of summer precipitation at Srinagar, Kashmir, India since the late 18th century. Holocene 4(3):299–306

Borgaonkar HP, Pant GB, Rupa Kumar K (1999) Tree-ring chronologies from Western Himalaya and their dendroclimatic potential. Int Assoc Wood Anatomists 20(3):295–309

Bunker AF (1965) Interaction of the summer monsoon air with the Arabian Sea, (Preliminary analysis). In: Proceeding symposium meteorological department results international Indian Ocean expedition, Bombay, pp 22–26

Chakraborty A, Nanjundiah RS, Srinivasan J (2006) A theory for the onset of Indian summer monsoon from perturbed orography simulations in a GCM. Annales De Geophysique 24:2075–2089

Chang CP (2004) The East Asian Monsoon. World Scientific, Singapore, p 564

Chauhan MS (2006) Late Holocene vegetation and climate change in the alpine belt of Himachal Pradesh, India. Curr Sci 91(11):1572–1578

Chauhan MS, Sharma C (2000) Late Holocene vegetation and climate in Deorital area, inner lesser Garhwal Himalaya. Palaeobotanist 49:509–514

Chauhan MS, Sharma C, Rajagopalan G (1997) Vegetation and climate during Late-Holocene in Garhwal Himalaya. Palaeobotanist 46:211–216

Chauhan MS, Mazari RK, Rajagopalan G (2000) Vegetation and climate in upper Spiti region, Himachal Pradesh during late Holocene. Curr Sci 79(3):373–377

Chen M-T, Shiau L-J, Yu P-S, Chiu T-C, Chen Y-G, Wei K-Y (2003) 500,000-year records of carbonate, organic carbon, and foraminiferal sea-surface temperature from the southeastern South China Sea (near Palawan Island). Palaeogeogr Palaeoclimatol Palaeoecol 197:113–131

Clift PD, Plumb RA (2008) The Asian monsoon: causes, history and effects, vol 135, no 639. Cambridge University Press, Cambridge, p 547

Demske D, Tarasov PE, Wünnemann B, Riedel F (2009) Late glacial and Holocene vegetation, Indian monsoon and westerly circulation in the Trans-Himalaya recorded in the lacustrine pollen sequence from Tso Kar, Ladakh, NW India. Palaeogeogr Palaeoclimatol Palaeoecol 279:172–185

Demske D, Tarasov PE, Leipe C, Kotlia BS, Joshi LM, Long T (2016) Record of vegetation, climate change, human impact and retting of hemp in Garhwal Himalaya (India) during the past 4600 years. Holocene 26(10):1661–1675

Dhar ON, Rakhecha PR (1983) Forecasting northeast monsoon rainfall over Tamil Nadu, India. Mon Weather Rev 111:109–112

Dimri AP, Niyogi D (2012) Regional climate model application at subgrid scale on Indian winter monsoon over the western Himalayas. Int J Climatol 33(9):2185–2205

Dimri AP, Yasunari T, Wiltshire A, Kumar P, Mathison C, Ridley J, Jacob D (2013) Application of regional climate models to the Indian winter monsoon over the western Himalayas. Sci Total Environ 468–469:36–47

Ding Y, Chan JCL (2005) The East Asian summer monsoon: an overview. Meteorol Atmos Phys 89(1–4):117–142

Dugam SS, Kakkade SB (2004) Antartica sea ice and monsoon variability. Radiat Phys Chem 73:306–309

Dugam SS, Kakade SB, Verma RK (1997) Interannual and long-term variability in north Atlantic oscillation and Indian summer monsoon rainfall. Theoret Appl Climatol 58:21–29

Findlater J (1969) A major low level air current near the Indian Ocean during the northern summer. Q J Royal Meteorol Soc 95:362–380

Flohn H (1957) Large-scale aspects of the "summer monsoon" in South and East Asia. J Meteorol Soc Jpn 75:180–186

Gadgil S (2003) The Indian Monsoon and its variability. Annu Rev Earth Planet Sci 31:429–467

Gasse F, Arnold M, Fontes JC, Fort M, Gilbert E, Hue A, Li Bingyan, Yuangang L, Qing L, Melieres F, Van Campo E, Fubao W, Qingsong Z (1991) A 13,000-year climate record from western Tibet. Nature 353:742–745

Gasse F, Fontes JC, Van Campo E, Wei K (1996) Holocene environmental changes in Bangong Co basin (western Tibet). Part 4. Discussions and conclusions. Palaeogeogr Palaeoecol Palaeoclimatol 120:79–92

Goswami BN (2012) South Asian monsoon. In: Lau WKM, Waliser DE (eds) Intraseasonal variability in the atmosphere-ocean climate system, 2nd edn. Springer, Berlin, pp 21–72

Gupta AK, Anderson DM, Overpeck JT (2003) Abrupt changes in the Asian southwest monsoon during the Holocene and their links to the North Atlantic Ocean. Nature 421:354–357

Hastenrath S (1987) On the prediction of Indian summer rainfall anomalies. J Climate Appl Meteorol 26:847–857

Hou S, Qin D, Zhang D, Kang S, Mayewski PA, Wake CP (2003) A 154a highresolution ammonium record from the Rongbuk Glacier, north slope of Mt. Qomolangma (Everest), Tibet-Himalayas region. Atmos Environ 37:721–729

Hou S, Chappellaz J, Raynaud D, Masson-Delmotte V, Jouzel J, Bousquet P, Hauglustaine D (2013) A new Himalayan ice core CH_4 record: possible hints at the preindustrial latitudinal gradient. Clim Past 9:2549–2554

Indian Meteorological Department Report (2013). http://metnet.imd.gov.in/imdnews/ar2013.pdf

Jain SK (2008) Impact of retreat of Gangotri glacier on the flow of Ganga River. Curr Sci 95(8):1012–1014

Joseph PV, Raman PL (1966) Existence of low level westerly Jetstream over peninsular India during July. Indian J Meteorol Geophys 17:407–410

Juyal N, Pant RK, Basavaiah N, Yadava MG, Saini NK, Singhvi AK (2004) Climate and seismicity in the higher Central Himalaya during 20–10 ka: evidence from the Garbyang basin, Uttaranchal, India. Palaeogeogr Palaeoclimatol Palaeoecol 213:315–330

Juyal N, Pant RK, Basavaiah N, Bhushan R, Jain M, Saini NK, Yadava MG, Singhvi AK (2009) Reconstruction of Last Glacial to early Holocene monsoon variability from relict lake sediments of the Higher Central Himalaya, Uttarakhand, India. J Asian Earth Sci 34:437–449

Kakade SB, Dugam SS (2000) The simultaneous effect of NAO and SO on the monsoon activity over India. Geophys Res Lett 27:3501–3504

Kakade SB, Kulkarni A (2012) Relationship between ESI tendency and Indian monsoon rainfall: a possible mechanism. Atmos Res Lett 13:22–28

Kang S, Mayewski PA, Qin D, Yan Y, Zhang D, Hou S, Ren J (2002) Twentieth century increase of atmospheric ammonia recorded in Mt. Everest ice core. J Geophys Res 30, 107(D20):4595

Kaspari S, Hooke R, Mayewski PA, Kang S, Hou S, Qin D (2008) Snow accumulation rate on Qomolangma (Mount Everest) Himalaya: synchroneity with sites across the Tibetan Plateau on 50–100 year timescales. J Glaciol 54:343–352

Kotlia BS, Joshi LM (2013) Neotectonic and climatic impressions in the zone of Trans Himadri Fault (THF), Kumaun Tethys Himalaya, India: A case study from palaeolake deposits. Zeitschriftfür Geomorphologie 57(3):289–303

Kotlia BS, Phartiyal B (1999) Palaeomagnetic results from Late Quaternary lake profiles at Wadda and Riyasi (Pithoragarh) and Phulara (Champawat) Kumaun Himalaya. Mem Geol Soc India 44:249–260

Kotlia BS, Rawat KS (2004) Soft sediment deformation structures in the Garbyang palaeolake: evidence for the past shaking events in the Kumaun Tethys Himalaya. Curr Sci 87(3):377–379

Kotlia BS, Sanwal J (2004) Fauna and palaeoenvironmental of a late Quaternary fluvio-lacustrine basin in central Kumaun Himalaya. Curr Sci 87:610–612

Kotlia BS, Bhalla MS, Sharma C, Rajagopalan G, Ramesh R, Chauhan MS, Mathur PD, Bhandari S, Chacko T (1997) Palaeoclimatic conditions in the upper Pleistocene and Holocene Bhimtal-Naukuchiatal lake basin in south-central Kumaun, North India. Palaeogeogr Palaeoclimatol Palaeoecol 130(1–4):307–322

Kotlia BS, Sharma C, Bhalla MS, Rajagopalan G, Subrahmanyam K, Bhattacharyya A, Valdiya KS (2000) Palaeoclimatic conditions in the Late Pleistocene Wadda lake, eastern Kumaun Himalaya (India). Palaeogeogr Palaeoclimatol Palaeoecol 162:105–118

Kotlia BS, Sanwal J, Phartiyal B, Joshi LM, Trivedi A, Sharma C (2010) Late Quaternary climatic changes in the eastern Kumaun Himalaya, India, as deduced from multi-proxy studies. Quatern Int 213:44–55

Kotlia BS, Singh AK, Joshi LM, Dhaila BS (2015) Precipitation variability in the Indian Central Himalaya during last ca. 4,000 years inferred from a speleothem record: Impact of Indian Summer Monsoon (ISM) and Westerlies. Quatern Int 371:244–253

Kotlia BS, Singh AK, Sanwal J, Raza W, Ahmad SM, Joshi LM, Sirohi M, Sharma AK, Sagar N (2016) Stalagmite inferred high resolution climatic changes through Pleistocene-Holocene Transition in Northwest Indian Himalaya. J Earth Sci Clim Change 7:338

Kotlia BS, Singh AK, Zhao Jian-Xin, Duan W, Tan M, Sharma AK, Raza W (2017) Stalagmite based high resolution precipitation variability for past four centuries in the Indian Central Himalaya: Chulerasim cave re-visited and data re-interpretation. Quat Int 444(A):35–43

Krishna KK, Hoerling M, Rajagopalan B (2005) Advancing dynamical prediction of Indian monsoon rainfall. Geophys Res Lett 32:L08704

Krishnamurthy V, Kinter JL (2003) The Indian monsoon and its relation to global climate variability. In: Rodo X, Comin FA (eds) Global climate, Springer, Berlin, pp 186–236

Krishnamurthy V, Shukla J (2000) Intraseasonal and interannual variability of rainfall over India. J Clim 13:4366–4377

Krishnan R, Zhang C, Sugi M (2000) Dynamics of breaks in the Indian summer monsoon. J Atmos Sci 57(9):1354–1372

Krishnan R, Kumar V, Sugi M, Yoshimura J (2009) Internal feedbacks from monsoon midlatitude interactions during droughts in the Indian Summer Monsoon. J Atmos Sci 66(3):553–578

Kulkarni AV, Rathore BP Mahajan S, Mathur P (2005) Alarming retreat of Parbati Glacier, Beas basin, Himachal Pradesh. Curr Sci 88(11):1844–1850

Kulkarni AV, Bahuguna IM, Rathore BP, Singh SK, Randhawa SS, Sood RK, Sunil D (2007) Glacial retreat in Himalaya using Indian remote sensing satellite data. Curr Sci 92(1):69–74

Kumar KK, Rajagopalan B, Cane AM (1999) On the weakening relationship between the Indian monsoon and ENSO. Science 5423:2156–2159

Lee K, Hur SD, Hou S, Burn-Nunes LJ, Hong S, Barbante C, Boutron CF, Rosman KJR (2011) Isotopic signatures for natural versus anthropogenic Pb in high-altitude Mt. Everest ice cores during the past 800 years. Sci Total Environ 412–413:194–202

Leipe C, Demske D, Tarasov PE, HIMPAC Project Members (2014) A Holocene pollen record from the northwestern Himalayan lake Tso Moriri: implications for palaeoclimatic and archaeological research. Quat Int 348:93–112

Li CY, Wang JT, Lin SZ, Cho HR (2004) The relationship between Asian summer monsoon activity and northward jump of the upper westerly jet location. Chin J Atmos Sci 28(5):641–658

Lone MA, Ahmad SM, Dung NC, Shen CC, Raza W (2014) Speleothem based 1000-year high resolution record of Indian monsoon variability during the last deglaciation. Palaeogeogr Palaeoclimatol Palaeoecol 395:1–8

Mazari RK, Bagati TN, Chauhan MS, Rajagopalan G (1995) Palaeoclimatic records of last 2000 years in Trans-Himalaya Lahaul-Spiti region. In: Proceedings Nagoya IGBP-Pages/REP-II Symposium, pp 262–268

Meehl GA, Arblaster JM (2002) The tropospheric biennial oscillation and Asian Australian monsoon rainfall. J Clim 15:722–744

Menzel P, Gaye B, Wiesner MG, Prasad S, Stebich M, Das BK, Anoop A, Riedel N, Basavaiah N (2013) Influence of bottom water anoxia on nitrogen isotopic ratios and amino acid contributions of recent sediments from small eutrophic lonar lake, central India. Limnol Oceanogr 58(3):1061–1074

Mishra PK, Anoop A, Schettler G, Prasad S, Jehangi A, Menzel P, Naumann R, Yousuf AR, Basavaiah N, Deenadayalan K, Wiesner MG, Gaye B (2015) Reconstructed late Quaternary hydrological changes from Lake Tso Moriri, NW Himalaya. Quatern Int 371:76–86

Morrill C, Overpeck JT, Cole JE, Liu K, Shen C, Tang L (2006) Holocene variations in the Asian monsoon inferred from the geochemistry of lake sediments in central Tibet. Quatern Res 65:232–243

Munot AA, Krishna KK (2007) Long range prediction of Indian summer monsoon rainfall. J Earth Syst Sci 116:73–79

Murakami T (1976) Cloudiness fluctuations during the summer monsoon. J Meteorol Soc Jpn 54:175–181

Murakami T (1987) Effects of the Tibetean plateau. In: Chang CP, Krishnamurthi TN (eds) Monsoon meteorology, vol 8. Oxford University Press, Oxford, pp 235–270

Overpeck JT, Sturm M, Francis JA, Perovich DK, Serreze MC, Benner R, Carmack EC, Chapin FS III, Gerlach SC, Hamilton LC, Hinzman LD, Holland M, Huntington HP, Key JR, Lloyd AH, MacDonald GM, McFadden J, Noone D, Prowse TD, Schlosser P, Vörösmarty C (2005) Arctic system on trajectory to new, seasonally ice-free state. Eos Trans Am Geophys Union 86(34):309–316

Pang H, Hou S, Kaspari S, Mayewski PA (2014) Influence of regional precipitation patterns on stable isotopes in ice cores from the central Himalayas. Cryosphere 8:289–301

Pant GB, Rupa Kumar K (1997) Climates of South Asia. Wiley, Chichester, p 320

Pant RK, Juyal N, Rautela P, Yadava MG, Sangode SJ (1998) Climate instability during Last Glacial stage: evidence from varve deposits at Goting, district Chamoli, Garhwal Himalaya, India. Curr Sci 75:850–855

Phadtare NR (2000) Sharp decrease in summer monsoon strength 4000–3500 cal yr B.P. in the central higher Himalaya of India based on pollen evidence from alpine peat. Quatern Res 53:122–129

Phartiyal B, Kotlia BS, Sanwal J (2002) Feasibility of mineral/environmental magnetic studies in the Late Quaternary basins of Kumaun Lesser Himalaya-Pithoragarh palaeolake as a case study. In: Pant CC, Sharma AK (eds) Aspects of geology and environment of the Himalaya, Gyanodaya Prakashan, Nainital, pp 313–328

Phartiyal B, Appel E, Blaha U, Hoffmann V, Kotlia BS (2003) Palaeoclimatic significance of magnetic properties from Late Quaternary lacustrine sediments at Pithoragarh, Kumaun Lesser Himalaya India. Quatern Int 108:51–62

Phartiyal B, Singh R, Kothyari GC (2015) Late-Quaternary geomorphic scenario due to changing depositional regimes in the Tangtse Valley, Trans-Himalaya, NW India. Palaeogeogr Palaeoclimatol Palaeoecol 422:11–24

Prasad S, Enzel Y (2006) Holocene paleoclimates of India. Quatern Res 66:442–453

Prasad S, Anoop A, Riedel N, Sarkar S, Menzel P, Basavaiah N, Krishnan R, Fuller D, Plessen B, Gaye B, Rhl U, Wilkes H, Sachse D, Sawant R, Wiesner MG, Stebich M (2014) Prolonged monsoon droughts and links to Indo-Pacific warm pool: a Holocene record from Lonar Lake, central India. Earth Planet Sci Lett 391:171–182

Raina VK, Sangewar C (2007) Siachen glacier of Karakorum Mountains, Ladakh its secular retreat. J Geol Soc India 70:11–16

Ramamurthy K (1969) Monsoon of India: some aspects of the 'break' in the Indian southwest monsoon during July and August. Forecast. India Meteorological Department, Poona, India, (18, 3), pp 1–57

Ramaswamy C (1972) The severe drought over Tamil Nadu during the retreating monsoon period of 1968 and its associations with anomalies in the upper level flow patterns over the northern hemisphere. Indian J Meteorol Geophys 23:303–316

Rao YP (1976) Southwest monsoon. Meteorological monograph, vol 1. India Meteorological Department, New Delhi, p 366

Rao SA, Chaudhari HS, Pokhrel S, Goswami BN (2010) Unusual central Indian drought of summer monsoon 2008: role of southern tropical Indian ocean warming. J Clim 23:5163–5174

Rasmussen EM, Carpenter TH (1983) The relationship between eastern equatorial Pacific sea surface temperature and rainfall over India and Sri Lanka. Mon Weather Rev 110:354–384

Rawat S, Phadtare NR, Sangode SJ (2012) The Younger Dryas cold event in NW Himalaya based on pollen record from the Chandra Tal area in Himachal Pradesh, India. Curr Sci 102(8):1193–1198

Rawat S, Gupta AK, Srivastava P, Sangode SJ, Nainwal HC (2015) A 13,000 year record of environmental magnetic variations in the lake and peat deposits from the Chandra valley, Lahaul: Implications to Holocene monsoonal variability in the NW Himalaya. Palaeogeogr Palaeoclimatol Palaeoecol 440:116–127

Ruddiman WF, Kutzbach JE (1989) Forcing of late Cenozoic northern hemisphere climate by plateau uplift in southern Asia and the American West. J Geophys Res 94:18409–18427

Rühland K, Phadtare NR, Pant RK, Sangode SJ, Smol JP (2006) Accelerated melting of Himalayan snow and ice triggers pronounced changes in a valley peatland from northern India. Geophys Res Lett 33:L15709

Saji NH, Goswami BN, Vinayachandran PN, Yamagata T (1999) A dipole mode in the tropical Indian Ocean. Nature 401:360–363

Sanwal J, Kotlia BS, Rajendran C, Ahmad SM, Rajendran K, Sandiford M (2013) Climatic variability in central Indian Himalaya during the last 1800 years: evidence from a high resolution speleothem record. Quatern Int 304:183–192

Sharma C, Gupta A (1995) Vegetation history of Nachiketatal, Garhwal Himalaya. J Nepal Geol Soc 10:29–34

Sharma C, Gupta A (1997) Vegetation and climate in Garhwal Himalaya during early Holocene: Deoriatal. Palaeobotanist 46:111–116

Sharma C, Chauhan MS, Ragagopalan G (2000) Vegetation and climate in Garhwal Himalaya during last 4,000 years. Palaeobotanist 49:501–508

Shukla J, Paolino JA (1983) The Southern Oscillation and the long range forecasting of summer monsoon rainfall over India. Mon Weather Rev 111:1830–1853

Sikka DR (1980) Some aspects of the large scale fluctuations of summer monsoon rainfall over India in relation to fluctuations in the planetary and regional scale circulation parameters. Earth Planet Sci Lett 89(2):179–195
Sikka DR, Gadgil S (1980) On the maximum cloud zone and the ITCZ over India longitude during the Southwest monsoon. Mon Weather Rev 108:1840–1853
Singh N, Sontakke NA (1999) On the variability and prediction of post-monsoon rainfall over India. Int J Climatol 19:309–339
Singh J, Yadav RR (2005) Spring precipitation variations over the western Himalaya, India since AD 1731 as deduced from tree rings. J Geophys Res 110:D01110
Singh J, Park W-K, Yadav RR (2006) Tree-ring-based hydrological records for western Himalaya, India, since AD 1560. Clim Dyn 26:295–303
Singh J, Yadav RR, Wilmking M (2009) A 694-year tree-ring based rainfall reconstruction from Himachal Pradesh, India. Clim Dyn 33:1149–1158
Singh D, Tsiang M, Rajaratnam B, Diffenbaugh NS (2014) Observed changes in extreme wet and dry spells during the South Asian summer monsoon season. Nat Clim Change 4:456–461
Soman MK, Kumar KK (1993) Space time evolution of meteorological features associated with the onset of Indian summer monsoon. Mon Weather Rev 21:1177–1194
Srivastava P, Kumar A, Mishra A, Meena NK, Tripathi JK, Sundriyal YP, Agnihotri A, Gupta AK (2013) Early Holocene monsoonal fluctuations in the Garhwal higher Himalaya as inferred from multi-proxy data from the Malari paleolake. Quatern Res 80:447–458
Sudipta S, Ramesh PS, Menas K (2004) Further evidences for the weakening relationship of Indian rainfall and ENSO over India. Geophys Res Lett 31(L13209):1–4
Thompson LG, Mosley-Thompson E, Davis ME, Bolzan JF, Dai J, Yao T, Gundestrup N, Wu X, Klein L, Xie Z (1989) Holocene-Late Pleistocene climatic ice core records from Qinghai-Tibetan Plateau. Science 246:474–477
Thompson LG, Mosley-Thompson E, Davis ME, Bolzan JF, Dai J, Klein L, Gundestrup N, Yao T, Wu X, Xie Z (1990) Glacial stage ice core records from the subtropical Dunde ice cap. Int Glaciol Soc 14:288–297
Thompson LG, Yao T, Mosley-Thompson E, Davis ME, Henderson KA, Lin PN (2000) High-resolution millennial record of the South Asian monsoon from Himalayan ice cores. Science 289:1916–1919
Trenberth KE, Stepaniak DP, Caron JM (2000) The global monsoon as seen through the divergent atmospheric circulation. J Clim 13:3969–3993
Upadhyay R (2009) The melting of the Siachen glacier. Curr Sci 96(5):646–648
Wang B (2006) The Asian monsoon. Springer, Chichester, p 787
Webster PJ (1987) The elementary monsoon. In: Fein JS, Stephens PL (eds) Monsoons. Wiley, New York, pp 3–32
Webster PJ, Yang S (1992) Monsoon and ENSO: selectively interactive systems. Q J Royal Meteorol Soc 118:877–926
Webster PJ, Magana VO, Palmer TN, Shukla J, Tomas RA, Yanai M, Yasunari T (1998) Monsoons: processes, predictability and the prospectus for prediction. J Geophys Res 103:14451–14510
Wünnemann B, Reinhardt C, Kotlia BS, Riedel F (2008) Observations on the relationship between Lake formation, permafrost activity lithalsa development during the last 20,000 years in the Tso Kar Basin, Ladakh, India. Permafrost Periglac Process 19:341–358
Wünnemann B, Demske D, Tarasov P, Kotlia BS, Reinhardt C, Bloemendal J, Diekmann B, Hartmann K, Krois J, Riedel F, Arya N (2010) Hydrological evolution during the last 15 kyr in the Tso Kar lake basin (Ladakh, India), derived from geomorphological, sedimentological and palynological records. Quatern Sci Rev 29:1138–1155
Xu J, Hou S, Qin D, Kang S, Ren J, Ming J (2007) Dust storm activity over the Tibetan Plateau recorded by a shallow ice core from the north slope of Mt. Qomolangma (Everest), Tibet-Himalayas region. Geophys Res Lett 34:L17504
Yadav RR (2011a) Tree-ring evidence of 20th century precipitation surge in monsoon shadow zone of western Himalaya, India. J Geophys Res Atmos 116:D02112

Yadav RR (2011b) Long-term hydroclimatic variability in monsoon shadow zone of western Himalaya. India Clim Dynam 36:1453–1462
Yadav RR (2013) Tree ring-based seven-century drought records for the western Himalaya, India. J Geophys Res Atmos 118:4318–4325
Yadav RR, Bhutiyani MR (2013) Tree-ring-based snowfall record for cold arid western Himalaya, India since A.D. 1460. J Geophys Res Atmos 118:7516–7522
Yadav RR, Park WK (2000) Precipitation reconstruction using ring-width chronology of Himalayan cedar from western Himalaya: preliminary results. J Earth Syst Sci 109:339–345
Yadav RK, Yoo JH, Kucharski F, Abid MA (2010) Why is ENSO influencing northwest India winter precipitation in recent decades? J Clim 23:1979–1993
Yadav RR, Misra KG, Yadava AK, Kotlia BS, Misra S (2015) Tree-ring footprints of drought variability in last ~300 years over Kumaun Himalaya, India and its relationship with crop productivity. Quatern Sci Rev 117:113–123
Yadava AK, Braeuning A, Singh J, Yadav RR (2016) Boreal spring precipitation variability in the cold arid western Himalaya during the last millennium, regional linkages, and socio-economic implications. Quatern Sci Rev 144:28–43
Yamagata T, Behera SK, Luo JJ, Masson S, Jury MR, Rao SA (2004) The coupled ocean-atmosphere variability in the tropical Indian Ocean. Earth's climate: the ocean-atmosphere interaction. Geophys Monogr 147:189–211
Zhang Q, Kang S, Kaspari S, Li C, Qin D, Mayewski PA, Hou S (2009) Rare earth elements in an ice core from Mt. Everest: Seasonal variations and potential sources. Atmos Res 94:300–312

Chapter 2
Speleothems and Climate

The Karst topography describes the dissolution of underlying soluble rocks by surface water or ground water. This is commonly found in carbonate terrain (limestone and dolomite) in mountainous regions. The rain water infiltrates through the cracks of the rocks in the vertical manner until it reaches the water table and thereafter, it moves horizontally below the surface of water table. The conditions of this process are, (1) exposure of thick limestone cover the ground surface, and (2) limestone cover overlain by non soluble rocks. The discernible character of the karst topography is simply known as caves and sinkholes.

Caves are formed by karstification where by downward percolating meteoric water interacts with the soil zone enriched in CO_2 content, thereby dissolving relatively soluble rocks (Bar-Matthews et al. 1996). Caves are naturally formed as underground cavity and their size ranges from few meters to several kilometres. They are formed in fractured and soluble rocks as a result of mechanical and chemical processes that continue over thousand to million years (White 1988; Forti 2009). The main cave types are solution caves, glacier caves and sea caves.

2.1 Cave Structures

All types of depositional features in the caves are collectively called as speleothems. These are formed by mostly calcite but occasionally aragonite (Goede et al. 1998). They are precipitated slowly by degassing of meteoric water fed drips in caves. The speleothems include helictites, straws, flowstones, stalactites and stalagmites etc. (Fig. 2.1a). The Helictites are twisted cave formations (Self and Hill 2003) like helix shape (three dimensional smooth space curve) with pointed end. These are formed by the seeping of the ceiling water and reorientation of crystal structure of calcite. A soda straw (tubular stalactite) is a hollow cylindrical tube (mostly 1–10 cm) at the ceiling of the cave. These straws become stalactites if the hole of bottom is blocked or water begins flowing on the outside surface of hallow tube. Each successive drop of water deposits little more minerals near roof of the cave. After regular deposition,

A. K. Singh, *High Resolution Palaeoclimatic Changes in Selected Sectors of the Indian Himalaya by Using Speleothems*, Springer Theses,
https://doi.org/10.1007/978-3-319-73597-9_2

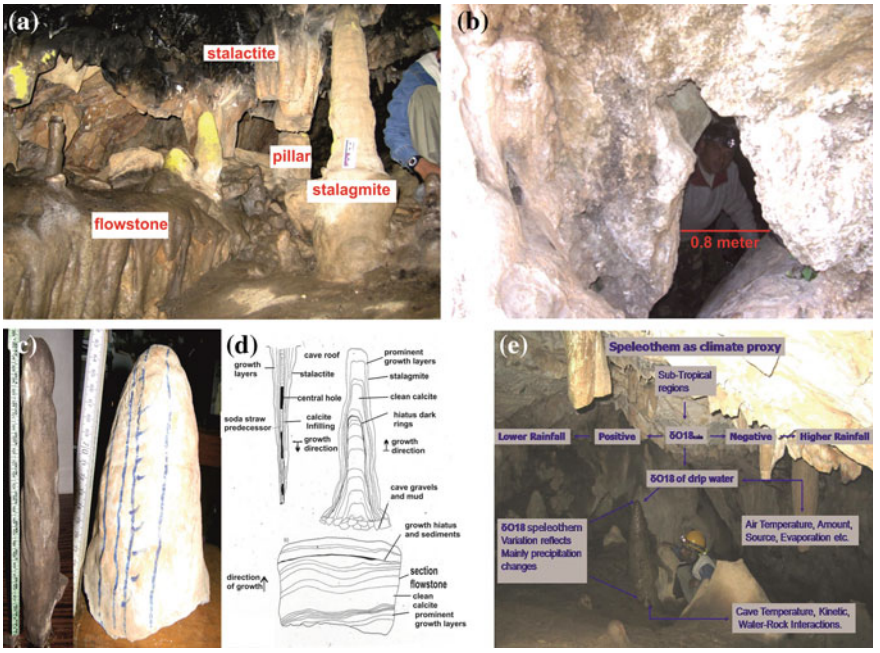

Fig. 2.1 Various cave structures: **a** Stalagmite, stalactite, pillar and flowstone, **b** Narrow entrance of the cave, **c** Conical stalagmite (candle shaped), **d** Sketch view of stalagmite and stalactite, **e** Processes in speleothem formation

these sharp and most fragile cave structures are formed. The stalactites are formations that hang from the ceiling of a cave (Fig. 2.1a). They have broad bases stuck to the cave ceiling (Hill and Forti 1997) and tapering ends hanging downward from the cave ceiling. The shape and size of stalactites are controlled by the cave ceiling and drip water (Sweeting 1972; Longman and Brownlee 1980; Jennings 1985). They are produced by precipitation of minerals from water dripping through the cave ceiling. If the cave ceiling is flat, stalactites are directly pointed towards the cave floor. But when the ceiling is inclined, elongated stalactites are formed.

Stalagmite is an upward-growing mineral deposit that has precipitated from water dripping onto the floor (Fig. 2.1a, c) of a cave (Railsback et al. 1994; Genty and Quinif 1996; Baker et al. 2008) and most stalagmites have rounded or flattened tips. They grow very slowly with isotopic equilibrium and save information in form of isotopes proxies (Dansgaard 1964; Rozanski et al. 1993; Moerrman et al. 2013). These are various processes involved in formation of cave structures (Fig. 2.1e). The stalagmites can develop under two conditions, (i) the development under equilibrium conditions, and (ii) under disequilibrium conditions. Pillar (Fig. 2.1a) is a calcite deposit, i.e., formed when stalactite and stalagmite meet together. Stalagmites are grouped into three categories (Franke 1965, 1975) on the basis of morphology. (a) uniform stalagmites are formed by constant drip rates (Curl 1973), calcite concentrations

Table 2.1 Comparison of various archives and their resolution

Archive	Temporal range	Potential resolution
Stalagmites	0 to ≥500 ka	5–10 years
Modern lakes	0 to ≥500 years	Seasonal to decadal
Palaeolakes	3 to 50 ka	Centennial
Peats	0 to ~11 ka	Decadal to centennial
Tree ring	0 to 2 ka	Seasonal

of the feed water and the cave atmosphere, (b) the conical form is generally common in low growth rate and or high drop fall height, (c) flow sheets are generally developed during the high precipitation (Gams 1981). Flowstones are deposits of minerals from water flowing over the floor and walls of a cave. Dripstones are calcareous deposits from dripping of water in dry limestone caves. Stalagmites long term records are used for documenting the significant changes in the frequency and magnitude of extreme climatic events (e.g., paleo-floods and droughts) and modelling of immediate future climate. They also have potential to record the palaeoclimatic changes with a range of past decade to thousand years (Hendy and Wilson 1968; Thompson et al. 1974).

The Quaternary archives such as lakes, marine cores, peat bogs and ice cores are studied by several researchers. But the strength of stalagmite is better than other on the basis of dating and resolution. Stalagmites can record continuous episodes of growth, preservation of information in the form of $\delta^{18}O$ and $\delta^{13}C$ isotopes. The excellent U/Th chronologies can be operated on stalagmites. This is far superior than other developed long records. These archives are physically and chemically robust and free from erosion and have very long potential resolution compared to other archives (Table 2.1).

2.2 Formation of Speleothems

When the rain water hits the ground, it percolates through the soil (or weak zones) and equilibrates with surrounding carbon dioxide (CO_2). Due to high amount of CO_2, the rain drop dissolves the limestone until solution is saturated. The deposition of calcite depends upon two mechanisms (Plummer et al. 1978; Buhmann and Dreybrodt 1985; Baker et al. 1998; Dreybrodt 1999), (i) surface reactions (ii) conversion of calcium carbonate ($CaCO_3$) into calcium bicarbonate $\{Ca(HCO_3)_2\}$ (Fig. 2.2). Each regular and continuous drop of water deposits more rings of calcite until soda straw formation occurs. The soda straw grows in length until it is filled with calcite and then water starts flowing down and outside the straw resulting in stalactite. The percolating water represents several reactions in its path. The chemical reaction of stalactite is

$$CaCO_3 + H_2O + CO_2 \rightleftharpoons Ca\,(HCO_3)_2$$

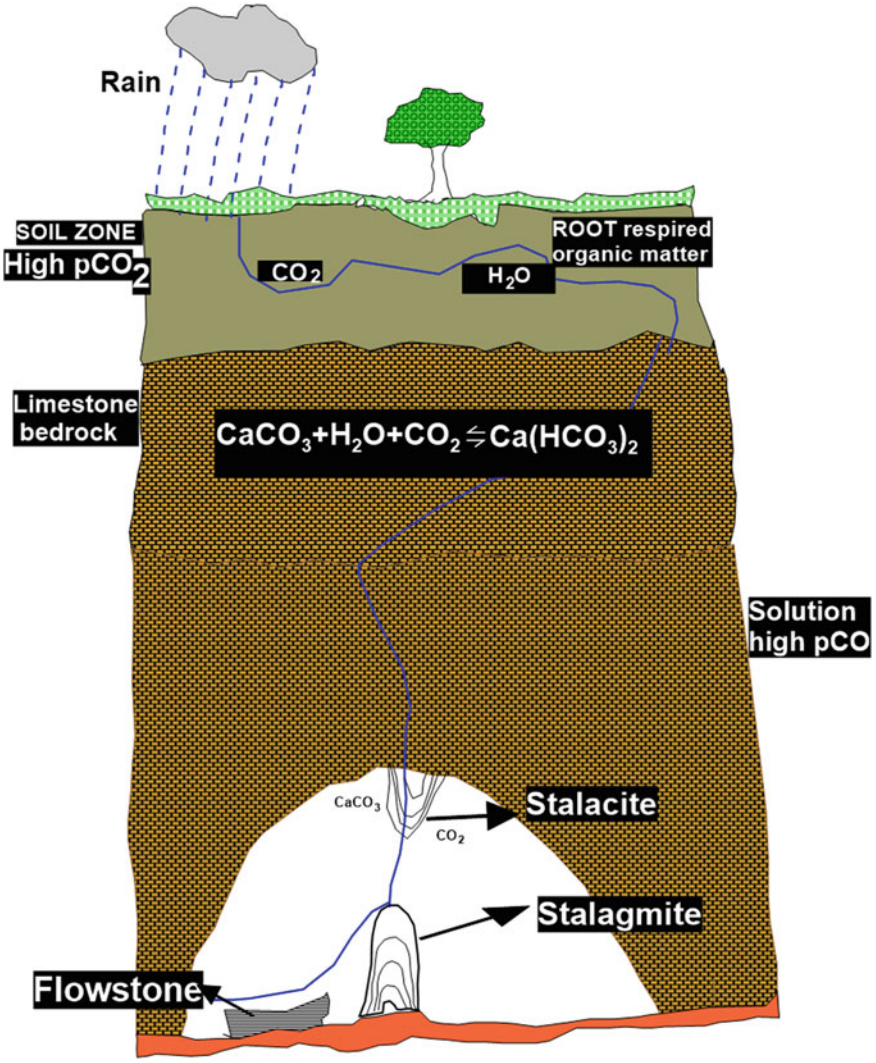

Fig. 2.2 Chemical processes of the formation of the speleothems

Formation of stalactite and stalagmite is in chemical equilibrium (A process where a forward and reverse reaction occurs at equal rates). As water droplet falls on the floor of the cave, it spreads out in wide pattern and flat rings are formed (Hendy 1969, 1971). The chemical reaction for the formula of stalagmite is reverse of the stalactite as

$$Ca\,(HCO_3)_2 \leftrightharpoons CaCO_3 + H_2O + CO_2$$

2.3 Ideal Stalagmites for Palaeoclimatic Study

The selection of ideal stalagmite is very important aspect for the palaeoclimatic research. The shape (morphology) of stalagmite depends upon the precipitation rate, nature of ceiling and shape the cave (Baker and Smart 1995; Baker et al. 1998; Proctor et al. 2000; Kaufmann 2003; Drysdale et al. 2005; Baldini et al. 2008). The candle or cylindrical shaped stalagmites (Fig. 2.1c) are best because of their consistent internal growth geometry (Genty and Quinif 1996; Frisia et al. 2000; Baldini 2001). They have several flat rings with a constant width from centre to margin. The ideal caves are horizontal with a small entrance (Fig. 2.1b). The small and narrow entrance supports that secondary calcite deposition typically occurs by degassing of CO_2 from carbonate saturated drip waters, because cave atmosphere usually have lower CO_2 levels (Schwarcz 1986; Ford and Williams 1989). If the cave is open then PCO_2 (partial, pressure of carbon dioxide) is same as external atmosphere. On the other hand, if the cave is closed with lack of ventilation, then PCO_2 level is high. This PCO_2 gradient between the drop and cave air causes conversion of bicarbonate (HCo_3^-) in Co_2 within the solution.

Cave temperature remains almost constant throughout the year in poorly ventilated caves (typically ± 1) (McDermott 2004), reflecting thermal inertia of host rocks (Gascoyne 1992; Lauritzen 1995; Repinski et al. 1999). For an ideal stalagmite, the cave air humidity is characterised by high relative humidity (95–100%) (Gams 1974; Vaupotič and Kobal 2004; Bezek et al. 2012) that minimizes the evaporation of the drip water.

2.4 Limitations in Speleothem Research

The composition and morphology of stalagmites depend upon the precipitation rate, capillary supply of ions, rate of CO_2 out gassing and the variability of these factors (González et al. 1992; Jones and Kahle 1993; Kendall 1993; Genty and Quinif 1996). Stalagmites can provide very useful information of palaeoclimatic changes, when they are formed in isotopic equilibrium (Hendy 1971). The evaporation effect and out gassing of CO_2 from droplet alters the isotopic equilibrium. This temperature and air effect of disequilibrium is known as kinetic fractionation. In equilibrium condition, candle or cylindrical shaped (Fig. 2.1c) stalagmites are formed.

The Hendy test is widely used for assessing whether isotopic equilibrium existed during the time of stalagmite formation (Fleitmann et al. 2004; Dykoski et al. 2005; Vacco et al. 2005; Johnson et al. 2006; Spötl et al. 2006; Mangini et al. 2007; Hu et al. 2008; Zhang et al. 2008; Zhou et al. 2008). According to Hendy test, $\delta^{18}O$ values remain constant along a single growth layer. The growth rate depends on the Ca concentration (cations and anions) (Kaufmann 2003). In stalagmites, most of the layers are thick at the central part (Fig. 2.1d) but thin and submerged at the outer part. In the Hendy test, the isotopic equilibrium criteria is that the $\delta^{13}C$ values do

not depend upon the $\delta^{18}O$ values (Hendy 1971) but this is not possible practically. This test is not ideal for isotopic equilibrium conditions because this takes place at the same time when kinetic fractionation occurs at the outer side of stalagmite (Talma and Vogel 1992; Spötl and Mangini 2002; Dreybrodt 2008). Thus, Hendy test could not explain the isotopic equilibrium conditions in all sections of a particular stalagmite. Moreover the sample resolution and error percentage are also important for the Hendy test.

2.5 High Precision Uranium-Series Dating

Stalagmites have strong chronological control for the last 500,000 years (Edwards et al. 1987). These are ideal material for dating by U series, specially using the 'daughter efficiency' $^{230}Th/U$ Method. The Uranium content in calcite speleothems are (typically 0.1–10 $\mu g/g$ ^{238}U) very less and are about an order of magnitude higher in aragonite rich speleothems (McDermott et al. 1999). Uranium is incorporated into $CaCO_3$ as the uranyl ion UO_2^+ derives from the dominant aqoues species $(UO_2 CO_3)_3^{4-}$. This is incorporated in speleothems only with non carbonate phases. Uranium dating in speleothems has played a significant role in Quaternary science in recent years. Thermal Ionization Mass Spectrometry (TIMS) technique for uranium series measurements (Edwards et al. 1987; Li et al. 1989) is well established for speleothems. TIMS and MC- IPMS methods are best because in these techniques, sample size (10–100 to 10–500 mg) and age error percentage (2–10 to 0.10–0.4%) are decreased (Goldstein and Stirling 2003). Recent technological developments support new high resolution magnetic sector Multi Collector Inductive Coupled Plasma Mass Spectrometers (MC-ICP-MS) with vastly improved ionisation efficiency for elements such as thorium and protactinium (Shen et al. 2002; Richards and Dorale 2003). The dead carbon (C^{14}) percentage in speleothems is in the range 10–25% (Genty and Massault 1999; Genty et al. 1999) and covers a time range of 10^2–10^3 years with large error percentage. Therefore, several researchers limit the use of ^{14}C as dating technique in speleothems.

2.5.1 Oxygen Isotopes in Speleothems

Stable isotopes of oxygen and carbon provide the main palaeo record of precipitation and vegetation. When movement of water and air in a cave is relatively slow, a thermal equilibrium is developed. The rainwater composition effect represents established empirical relationship between precipitation $\delta^{18}O$ values and certain climatic parameters such as rainfall intensity (Dansgaard 1964; Rozanski et al. 1993; Spötl and Mangini 2002; Fleitmann et al. 2004; Harmon et al. 2004; Vollweiler et al. 2006; Wang et al. 2008; Moerrman et al. 2013) and temperature (Dansgaard 1964). The $\delta^{18}O$ values decrease with increasing amount of rainfall

(see Fig. 2.1e) (Fleitmann et al. 2003). Thus, the $\delta^{18}O$ values show inverse proportion to the precipitation.

On the basis of seasonal time scales, variations of $\delta^{18}O$ in precipitation arise from variations in the source of rainfall. The high resolution $\delta^{18}O$ series of speleothems gives evidence of solar activity influence on the ISM (Neff et al. 2001; Shindell et al. 2001; Fleitmann et al. 2003; Niggemann et al. 2003). In semi arid to arid climate, heavier $\delta^{18}O$ values are observed due to high evaporation process than precipitation (Bar-Matthews et al. 1996). The $\delta^{18}O$ is used to express the value of the oxygen isotope ratio ($^{18}O/^{16}O$) in a sample relative to that in a standard. Thus $\delta^{18}O = \{(^{18}O/^{16}O)$ sample/$(^{18}O/^{16}O)$ standard)}–1) * 1000) where s is the unknown sample and std is a standard that has been calibrated relative to the Pee Dee Belemnite (PDB) [usually expressed as Vienna Pee Dee Belemnite (VPDB)] or Vienna Standard Mean Ocean Water (VSMOW). The principle relationship between $\delta^{18}O$ and temperature is approximately $-24\ °C^{-1}$ at $25\ °C^{-1}$ (O'Neil et al. 1969). But for mid-high latitudes, this relation is calculated as an average of $0.6‰\ °C^{-1}$ (Rozanski et al. 1993).

The $\delta^{18}O$ composition of atmospheric precipitation becomes increasingly negative with decrease in temperature. The basic fact is that the maximum amount of precipitation that air can hold drops with decreasing temperatures (Dansgaard 1964). When humid air cools at a point the water molecules will condensate to form precipitation. The relation between $\delta^{18}O$ and temperature is averaged ($+0.59 \pm 0.09‰\ °C$) (Dansgaard 1964; Rozanski et al. 1993) per degree celcius for mid to high latitude region (Gascoyne 1992; Dorale et al. 1992, 1998; McDermott et al. 1999, 2006; Paulsen et al. 2003).

2.5.2 *Carbon Isotopes in Speleothems*

Carbon isotope ratio reflects a balance between light biogenic carbon (^{12}C) and heavier carbon (^{13}C) dissolved from precipitated water. The $\delta^{13}C$ values are capable of preserving vegetation signatures, such as soil organic matter (Boutton 1996). Soil yields CO_2 by microbial decomposition of soil organic matter and root respiration of the plants whose intensity increases during wet periods resulting in high PCO_2 and depleted $\delta^{13}C$ (Hesterberg and Siegenthaler 1991). The stalagmites are capable of recording the proportion of C_3 and C_4 plant biomass (Cerling 1984; Deines 1986; Cerling and Quade 1993; Dorale et al. 1998; Hellstrom et al. 1998; Genty et al. 2006) through time and are indirectly linked to the precipitation (Richards and Dorale 2003). The formula for $\delta^{13}C$ is used to express the value of the carbon isotope ratio ($^{13}C/^{12}C$) in a sample relative to that in a standard. Thus $\delta^{13}C = (^{13}C/^{12}C)$ sample/$(^{13}C/^{12}C)$ standard)–1) * 1000) where s is the sample (unknown) and std a standard that has been calibrated relative to the Pee Dee Belemnite (PDB).

After deposition, the secondary carbonate deposits have a range of $\delta^{13}C$ between -14 to $-6‰$ for C_3 and -6 to $2‰$ for C_4 plants (Cerling 1984). Due to restricted stomata conductance, the $\delta^{13}C$ of respired soil CO_2 of C_3 plants is heavier under dry

conditions and lighter under humid conditions. Carbon sources in speleothems are soil CO_2 and bed rock carbon and depend upon three parameters such as photosynthetic pathway, biological activity and drip rate.

2.5.3 Trace Elements and Mineralogy

Speleothems are mainly composed of calcite and aragonite or both. Aragonite and calcite can precipitate regularly at the same time but they reflect separate episodes of growth rates in speleothems. The internal structure of stalagmite reflects the annual band thickness (Ayliffe et al. 1998; Fairchild et al. 2001; Spötl and Mangini 2002; Duan et al. 2013). Mg rich calcite is mainly deposited in wet season and aragonite mainly in arid climate. Trace element analysis is generally related with the colour of growth rings (James 1997; White 1997). The light colour growth rings are mainly formed in high precipitation duration. But in arid time period, Mg/Ca ratio decreases and dark colour bands are formed.

Mineralogy of stalagmites is explored by XRD (X-ray Diffraction) and SEM (Scanning Electron Microscope). Proxy records using mineralogy were first established by Fairchild et al. (2000). Recently, Duan et al. (2013) reported precipitation variation in the Indian speleothems based on mineralogy. The thickness of annual lamination thickness is directly related to amount of precipitation year, which has been proved by experimental studies (Baker and Smart 1995; Dreybrodt 1996, 1999; Baker et al. 1998) and theoretical studies (Buhmann and Dreybrodt 1985). The growth rate in stalagmites is controlled by many physical factors (Dreybrodt 1988, 1999; Baker et al. 1999; Kaufmann 2003). It depends upon the mean annual temperature at the site, drip water rate and calcium concentration of drip waters (Genty et al. 2001; Polyak and Asmeron 2001; Fleitmann et al. 2004). In some stalagmites, annual visible or luminescent bands can establish independent verification of radiometric chronologies (Wang et al. 2001; Frisia et al. 2002; Hou et al. 2003; Fleitmann et al. 2004). The drip interval is defined as the time between the two continuous drops. It depends upon the drop volume, composition and precipitation amount. Regular monitoring of caves can give information about the precipitation behaviour, growth rate and its relationship with isotopes.

2.6 Speleothem Research in India

The speleothem research in India is in its early stage. Speleothem isotope records were first studied by Yadava (2002) from south Indian caves. Subsequently, Yadava et al. (2004) carried out rainfall variations on a 331-year old speleothem from Peninsular India. The work was further extended to Orissa (Gupteswar Cave) for reconstructing the rainfall data for the last about 3.5 ka BP (Yadava and Ramesh 2005). Yadava and Ramesh (2006) studied stable oxygen and carbon isotopes in stalagmites

collected from four locations viz., Gupteswar (Orissa), Dandak (Chhattisgarh), Sota (Uttar Pradesh), and Akalagavi (Karnataka) and reported various wet/dry periods within the last ~3.4 ka BP. Similarly, A 900 year (600–1500 AD) record of Dandak cave, Peninsular India (Sinha et al. 2007) reflects the Medieval Warm Period (MWP) and the earliest portion of the Little Ice Age (LIA). Two stalagmites from Baratang Cave in Andaman Islands, covering last ~4 ka BP documented the transition of MWP to LIA (Laskar et al. 2013). Lately, Lone et al. (2014) investigated Valmiki Cave covering a time period from 15.7 to 14.7 ka BP with an average sampling resolution of ~5 years. In the Indian Himalaya, Sinha et al. (2005) studied Timta Cave from eastern part of the central Himalaya that revealed the decrease in ISM intensity during Bølling–Allerød (BA) interstadial between 15.2 to 11.7 ka BP. A detailed study of the past precipitation from Chulerasim Cave in central Himalaya was performed by Kotlia et al. (2012) who suggested two prominent climatic phases (LIA and post-LIA) and interestingly showed that the LIA in the Himalaya was wet, while the post-LIA was drier and warmer. Duan et al. (2013) also worked on Chulerasim mineralogy and laminae counting to reconstruct the precipitation conditions for last 400 years. Stable isotope records of Dharamjali Cave (Sanwal et al. 2013) displayed the ISM variability during MWP and LIA. A cave record of ~4 ka BP from Sainji Cave reflects precipitation behaviour of ISM and WD_S in the Himalaya and its relation with Harappan/Indus civilization (Kotlia et al. 2015). A 2 ka BP record of Sahiya Cave shows that ISM intensity highly decreased in last 50 to 60 years perhaps due to anthropogenic activities (Sinha et al. 2015). Similarly, Mawmluh Cave (Meghalaya) has been studied for middle Holocene climate and is well correlated with Indus and Nile river civilizations (Berkelhammer et al. 2012). Another stalagmite record from 33.8 to 55 ka BP (Dutt et al. 2015) from Mawmluh Cave reveals monsoon intensity during major climatic events (YD, BA and Heinrich Event). Kathayat et al. (2016) systematically studied Bitto Cave and obtained the results for the last 280 ka BP with a relation between ISM and EASM (East Asian Summer Monsoon). More Recently, Kotlia et al. (2016) studied a stalagmite from Jammu and Kashmir (NW Himalaya) covering the record of Last Pleistocene-Holocene transition and foot prints of Older Dryas (OD), Allerød period and YD.

2.6.1 Stalagmite Records from China and Nearby Areas

Several researchers have investigated cave records from China and nearby areas to establish a relationship among ISM, EASM and ITCZ. A study on two stalagmites from Jiuxian Cave (Central China) indicated that the EASM was not very much effective on ISM behaviour during Holocene (Cai et al. 2010). The isotopic analysis of six stalagmites of Sanbo Cave by Dong et al. (2010) indicates the climatic variation in the last 13 ka BP and supports that the ITCZ affects ISM and EASM regularly. The $\delta^{13}C$ analysis of Lianhua Cave (Cosford et al. 2008) reflected the vegetational record of mid to late Holocene and two intervals of warm humid and cold arid phase. Hu et al. (2008) investigated Heshang Cave and reported some major climatic events

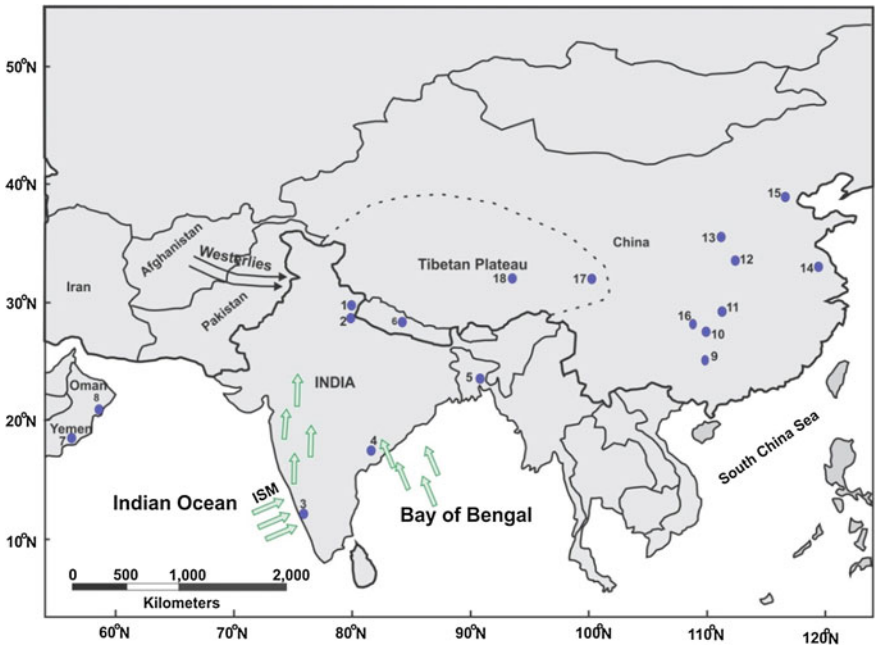

Fig. 2.3 Locations of the caves in different parts of Himalaya and nearby areas. 1. Panigarh Cave (Liang et al. 2015), 2. Timta Cave (Sinha et al. 2005), 3. Akalagavi Cave (Yadava et al. 2004), 4. Dandak and Jhumar Cave (Yadava and Ramesh 2005; Sinha et al. 2007, 2011), 5. Mawmluh Cave (Berkelhammer et al. 2012), 6. Sidha Baba Cave (Denniston et al. 2000), 7. Qunf Cave (Fleitmann et al. 2003), 8. Hoti Cave (Fleitmann et al. 2007), 9. Dongge Cave (Wang et al. 2005; Dykoski et al. 2005), 10. Shigao Cave (Jiang et al. 2012), 11. Heshang Cave (Hu et al. 2008), 12. Budha Cave (Paulsen et al. 2003), 13. Jiuxian Cave (Cai et al. 2010), 14. Hulu Cave (Wang et al. 2001), Kelly et al. 2006), 15. Shihua Cave (Ku and Li 1998), 16. Lianhua Cave (Cosford et al. 2008), 17. Sanbo Cave (Dong et al. 2010), 18. Tianmen Cave (Cai et al. 2012)

as, 8.2 ka event and LIA and showed high rainfall intensity in Holocene than today. Wang et al. (2001) reported five stalagmites from Hulu Cave and explained the importance climatic events such as YD and BA transition and their comparison with ice core records. A high resolution (1–3 year) stalagmite record of Budha cave (Paulsen et al. 2003), China covered a time span of 12.7 ka BP and reflected climatic events such as MWP and LIA (Fig. 2.3).

Similarly, a more detailed study of Shigao Cave (Jiang et al. 2012) record revealed a number of wet/dry phases and their link with solar forcing effect on the ISM and EASM. A 500 year old stalagmite from Shihua Cave reflects fourteen precipitation cycles of 30–40 years and many wet/dry phases (Ku and Li 1998). The Dongge Cave stalagmite has revealed the last 9 ka BP record with dry period (8.2 ka BP) and its relationship with Neolithic Chinese culture (Wang et al. 2005). Dykoski et al. (2005) also reported a continuous record for the last 16 ka BP from Dongge Cave and developed a relationship between Asian monsoon intensity and North

Atlantic climate during glacial period to early Holocene. An important stalagmite study (Tianmen Cave) from south Tibet demonstrates the control of solar activity on the ISM and EASM behaviour during last 8.7–4.3 ka BP (Cai et al. 2012).

Similarly, an aragonite stalagmite record (Siddha Baba Cave, Nepal) shows ISM variability and aridity at 2.3–1.5 ka BP and wet period after 1.5 ka BP (Denniston et al. 2000). The Four stalagmite records (Hotti Cave) of Oman and Yemen (Fleitmann et al. 2007; Yang et al. 2010) cover a time period from early to late Holocene and explain the relation between ITCZ migration and weakening of ISM period since 4.5 ka BP. The Qunf Cave (Fleitmann et al. 2003) covers a time period of 10.4–0.4 ka BP with a high peak aridity event (8.3 ka BP). The Moomi Cave stalagmite covers a time period of 27.4–11.1 ka BP with two peak aridity events and major global events such as YD and BA transition (Shakun et al. 2007).

2.7 Objectives of the Present Study

(a) Documentation of caves in selected parts of Jammu and Kashmir, Himachal Pradesh and Uttarakhand Himalaya. Detailed mapping of caves having ideal stalagmites and the selection of most ideal stalagmites for laboratory measurements.
(b) Stable isotopic ($\delta^{13}C$ and $\delta^{18}O$) determination at an interval of ca. 0.8 mm along the growth axis. Dating of selected samples (at least at an interval of ca. 10 cm) using Uranium series dating method through Thermal Ionisation Mass Spectrometry (TIMS).
(c) Mineralogy and trace element analysis to reconstruct the palaeoclimatic conditions in the surroundings, rainfall and other processes like intense evaporation rate etc.
(d) Reconstruction and interpretation of past precipitation on at least multi annual to decadal scale in the Indian Himalaya under various precipitation regimes.

References

Ayliffe LK, Marianelli PC, Moriarty KC, Wells RT, McCulloch MT, Mortimer GE, Hellstrom JC (1998) 500 ka precipitation record from southeastern Australia: evidence for interglacial relative aridity. Geology 26:147–150

Baker A, Smart PL (1995) Recent flowstone growth rates: field measurements in comparison to theoretical predictions. Chem Geol 122:121–128

Baker A, Genty D, Dreybrodt W, Barnes WL, Mockler NJ, Grapes J (1998) Testing theoretically predicted stalagmite growth rate with recent annually laminated samples: implications for past stalagmite deposition. Geochim Cosmochim Acta 62:393–404

Baker A, Mockler NJ, Barnes WL (1999) Fluorescence intensity variations of speleothem-forming groundwaters: implications for paleoclimate reconstruction. Water Resour Res 35(2):407–413

Baker A, Smith CL, Jex C, Fairchild IJ, Genty D, Fuller L (2008) Annually laminated speleothems: a review. Int J Speleol 37:193–206

Baldini JUL (2001) Morphologic and dimensional linkage between recently deposited speleothems and drip water from Browns Folly Mine, Wiltshire, England. J Cave Karst Stud 63:83–90
Baldini JUL, McDermott F, Hoffmann DL, Richard DA, Clipson N (2008) Very high-frequency and seasonal cave atmosphere PCO_2 variability: Implications for stalagmite growth and oxygen isotope-based paleoclimate records. Earth Planet Sci Lett 272:118–129
Bar-Matthews M, Ayalon A, Matthews A, Sass E, Halicz L (1996) Carbon and oxygen isotope study of the active water-carbonate system in a karstic Mediterranean cave: implications for palaeoclimate research in semiarid regions. Geochem et Cosmochim Acta 60:337–347
Berkelhammer M, Sinha A, Stott L, Cheng H, Pausata FSR, Yoshimura K (2012) An abrupt shift in the Indian monsoon 4000 years ago. In: Giosan L, Fuller DQ, Nicoll K, Flad RK, Clift PD (eds) Climates, landscapes, and civilizations, American Geophysical Union, vol 198, pp 75–87
Bezek M, Gregorič A, Kávási N, Vaupotič J (2012) Diurnal and seasonal variations of concentration and size distribution of nano aerosols (10–1100 nm) enclosing radon decay products in the Postojna Cave, Slovenia. Radiat Prot Dosim 152:174–178
Boutton TW (1996) Stable carbon isotope rations of soil organic matter and their use as indicators of vegetation and climate change. In: Yamasaki S, Boutton TW (eds) Mass spectrometry of soils. Marcel Dekker, New York, pp 47–81
Buhmann D, Dreybrodt W (1985) The kinetics of calcite dissolution and precipitation in geologically relevant situations of karst areas-open system. Chem Geol 48:189–211
Cai YJ, Tan LC, Cheng H, An ZS, Edwards RL, Kelly MJ, Kong XG, Wang XF (2010) The variation of summer monsoon precipitation in central China since the last deglaciation. Earth Planet Sci Lett 291:21–31
Cai YJ, Zhang HW, Cheng H, An ZS, Edwards RL, Wang XF, Tan LC, Liang FY, Wang J (2012) The Holocene Indian monsoon variability over the southern Tibetan Plateau and its teleconnections. Earth Planet Sci Lett 335:135–144
Cerling TE (1984) The stable isotope composition of modern soil carbonate and its relationship to climate. Earth Planet Sci Lett 71:229–240
Cerling TE, Quade J (1993) Stable carbone and oxygen isotopes in soil carbonates. In: Swart PK, Lohmann KC, McKenzie J, Savin S (eds) Climate change in continental isotopic records, American Geophysical Union, pp 217–231
Cosford J, Qing HR, Eglington B, Mattey D, Yuan DX, Zhang ML, Cheng H (2008) East Asian monsoon variability since the Mid-Holocene recorded in a high-resolution, absolute-dated aragonite speleothem from eastern China. Earth and Planet Sci Lett 275:296–307
Curl RL (1973) Minimum diameter stalagmites. Bull Natl Speleol Soc 35:1–9
Dansgaard W (1964) Stable isotopes in precipitation. Tellus 16:436–468
Deines P (1986) The isotopic composition of reduced organic carbon. In: Fritz P, Fontes JC (eds) Handbook of environmental geochemistry: the terrestrial environment, Amsterdam, pp 331–406
Denniston RF, Gonzalez LA, Asmerom Y, Sharma RH, Reagan MK (2000) Speleothem evidence for changes in Indian summer monsoon precipitation over the last ~2300 years. Quat Res 53(2):196–202
Dong JG, Wang YJ, Cheng H, Hardt B, Edwards RL, Kong XG, Wu JY, Chen ST, Liu DB, Jiang XY, Zhao K (2010) A high-resolution stalagmite record of the Holocene East Asian Monsoon from Mount Shennongjia, central China. Holocene 20:257–264
Dorale JA, González LA, Reagan MK, Pickett DA, Murrell MT (1992) A high resolution record of Holocene climate change in speleothem calcite from Cold Water Cave northeast Iowa. Science 258:1626–1630
Dorale JA, Edwards RL, Ito E, Gonzalez LA (1998) Climate and vegetation history of the mid-continent from 75 to 25 ka: a speleothem record from Crevice Cave. Missouri, USA Science 282:1871–1874
Dreybrodt W (1988) Processes in Karst Systems: physics, chemistry, and geology. Springer, Berlin, pp 1–288

Dreybrodt W (1996) Principles of early development of karst conduits under natural and man-made conditions revealed by mathematical analysis of numerical models. Water Resour Res 32:2923–2935

Dreybrodt W (1999) Chemical kinetics, speleothem growth and climate. Boreas 28:347–356

Dreybrodt W (2008) Evolution of the isotopic composition of carbon and oxygen in a calcite precipitating H_2O-CO_2-$CaCO_3$ solution and the related isotopic composition of calcite in stalagmites. Geochim Cosmochim Acta 72:4712–4724

Drysdale RN, Zanchetta G, Hellstrom JC, Fallick AE, Zhao JX (2005) Stalagmite evidence for the onset of the last interglacial in Southern Europe at 129 ± 1 ka. Geophys Res Lett 32:L24708

Duan W, Kotlia BS, Tan M (2013) Mineral composition and structure of the stalagmite laminae from Chulerasim cave, Indian Himalaya and the significance for palaeoclimatic reconstruction. Quat Int 298:93–97

Dutt S, Gupta AK, Clemens SC, Cheng H, Singh RK, Kathayat G, Edwards RL (2015) Abrupt changes in Indian summer monsoon strength during 33,800 to 5500 years B.P. Geophys Res Lett 42:5526–5532

Dykoski C, Edwards RL, Cheng H, Yuan DX, Cai YJ, Zhang ML, Lin YS, Qing JM, An ZS, Revenaugh J (2005) A high resolution absolute dated Holocene and deglacial Asian monsoon record from Dongge cave, China. Earth Planet Sci Lett 233:71–86

Edwards RL, Chen JH, Wasserburg GJ (1987) ^{238}U–^{234}U–^{230}Th–^{232}Th Systematics and the precise measurement of time over the past 5,00,000 years. Earth and Planet Sci Lett 81:175–192

Fairchild IJ, Borsato A, Tooth AF, Frisia S, Hawkesworth CJ, Huang Y, McDermott F, Spiro B (2000) Controls on trace element (Sr-Mg) compositions of carbonate cave waters: implications for speleothem climatic records. Chem Geol 166:255–269

Fairchild I, Baker A, Borsato A, Frisia S, Hinton R, McDermott F, Tooth A (2001) Annual to sub-annual resolution of multiple trace-element trends in speleothems. J Geol Soc 158:831–841

Fleitmann D, Burns SJ, Neff U, Mangini A, Matter A (2003) Changing moisture sources over the last 330,000 years in Northern Oman from fluid-inclusion evidence in speleothems. Quat Res 60:223–232

Fleitmann D, Burns SJ, Neff U, Mudelsee M, Mangini A, Matter A (2004) Palaeoclimatic interpretation of high resolution oxygen isotope profiles derived from annually laminated speleothems from Southern Oman. Quat Sci Rev 23:935–945

Fleitmann D, Burns SJ, Mangini A, Mudelsee M, Kramers J, Villa I, Neff U, Al Subbary AA, Buettner A, Hippler D, Matter A (2007) Holocene ITCZ and Indian monsoon dynamics recorded in stalagmites from Oman and Yemen (Socotra). Quat Sci Rev 26:170–188

Ford DC, Williams PW (1989) Karst geomorphology and hydrology. Academic Division of Unwin Hyman Ltd, London, p 601

Forti P (2009) State of the art in the speleological sciences. In: Proceeding XV International speleological congress. Kerrville Texas, vol 1, pp 26–31

Franke HW (1965) The theory behind stalagmite shapes. Stud Speleol 1:89–95

Franke HW (1975) Sub-minimum diameter stalagmites. Bull Natl Speleol Soc 37:17–18

Frisia S, Borsato A, Fairchild IJ, McDermott F (2000) Calcite fabrics, growth mechanisms, and environments of formation in speleothems from the Italian Alps and southwestern Ireland. J Sediment Res 70:1183–1196

Frisia S, Borsato A, Fairchild IJ, Mcdermott F, Selmo EM (2002) Aragonite-calcite relationships in speleothems (grotte de clamouse, France): environment, fabrics, and carbonate geochemistry. J Sediment Res 72:687–699

Gams I (1974) Concentration of CO_2 in the caves in relation to the air circulation (in the cave of the Postojna Cave). Acta Carsologica 6:183–192

Gams I (1981) Contribution to morphometrics of stalagmites. In: Proceedings of the 8th international congress of speleology, Bowling Green, Kentucky, pp 276–278

Gascoyne M (1992) Palaeoclimate determination from cave calcite deposits. Quat Sci Rev 11:609–632

Genty D, Massault M (1999) Carbon transfer dynamics from bomb-^{14}C and δ^{13}C time series of a laminated and stalagmite from SW France-modelling and comparison with other stalagmite records. Geochim Cosmochim Acta 63(10):1537–1548

Genty D, Quinif Y (1996) Annually laminated sequences in the internal structure of some Belgian stalagmites; importance for paleoclimatology. J Sediment Res 66(1):275–288

Genty D, Massault M, Baker A, Vokal B, Proctor CJ (1999) Reconstitution of bomb ^{14}C time history recorded in four modern stalagmites by AMS measurements: importance for carbon transfer dynamics. In: 8th international conference on AMS Vienna, p 93

Genty D, Baker A, Vokal B (2001) Intra and inter-annual growth rate of modern stalagmites. Chem Geol 176:191–212

Genty D, Blamart D, Ghaleb B, Plagnes V, Causse CH, Bakalowicz M, Zouari K, Chkir N, Hellstrom J, Wainer K, Bourge F (2006) Timing and dynamics of the last deglaciation from European and North African δ^{13}C stalagmite profiles comparison with Chinese and South Hemisphere stalagmites. Quat Sci Rev 25:2118–2142

Goede A, McCulloch M, McDermott F, Hawkesworth C (1998) Aeolian contribution to strontium and strontium isotope variations in a Tasmanian speleothem. Chem Geol 149:37–50

Goldstein SJ, Stirling CH (2003) Techniques for measuring Uranium-series nuclides: 1992-(2002). In: Bourdon B, Henderson GM, Lundstrom CC Turner SP (eds) Uranium-series geochemistry. Reviews in Mineralogy and Geochemistry, vol 52, pp 23–57

González LA, Carpenter SJ, Lohmann KC (1992) Inorganic calcite morphology-roles of fluid chemistry and fluid-flow. J Sediment Petrol 62:382–399

Harmon R, Schwarz H, Gascoyne M, Hess J, Ford D (2004) Studies of cave sediments. Physical and chemical records of palaeoclimate: Palaeoclimate information from Speleothems: The Present as a guide to the past, Kluwer, New York, pp 199–226

Hellstrom J, McCulloch MT, Stone J (1998) A detailed 31,000 year record of climate and vegetation change from the isotope geochemistry of two New Zealand speleothems. Quat Res 50:167–178

Hesterberg R, Siegenthaler U (1991) Production and stable isotopic composition of CO_2 in a soil near Bern, Switzerland, Tellus 43B:197–205

Hendy CH (1969) The use of C-14 in the study of cave processes. In: Proceedings of the Xllth nobel symposium, Uppsala, University of Uppsala, pp 419–443

Hendy CH (1971) The isotopic geochemistry of speleothems-I. The calculation of the effects of different modes of formation on the isotopic composition of speleothems and their applicability as paleoclimatic indicators. Geochim Cosmochim Acta 35:801–824

Hendy CH, Wilson AT (1968) Palaeodimatic data from speleothems. Nature 216:48–51

Hill C, Forti P (1997) Cave minerals of the world, 2nd edn. National Speleological Society, pp 1–463

Hou S, Qin D, Zhang D, Kang S, Mayewski PA, Wake CP (2003) A 154a highresolution ammonium record from the Rongbuk Glacier, north slope of Mt. Qomolangma (Everest) Tibet-Himalayas region. Atmos Environ 37:721–729

Hu CY, Henderson GM, Huang J, Xie SC, Sun Y, Johnson KR (2008) Quantification of Holocene Asian monsoon rainfall from spatially separated cave records. Earth Planet Sci Lett 266:221–232

James JM (1997) Minor, trace and ultra-trace constituents of speleothems. In: cave minerals of the world. In: Hill CA, Forti P (eds) National Speleological Society, pp 236–237

Jennings JN (1985) Karst Geomorphology. Basil Blackwell, Oxford p, p 293

Jiang XY, He YQ, Shen C-C, Kong XG, Li ZZ, Chang Y-W (2012) Stalagmite inferred Holocene precipitation in northern Guizhou Province, China, and asynchronous termination of the climatic optimum in the Asian monsoon territory. Chin Sci Bull 57:795–801

Johnson KR, Hu C, Belshaw NS, Henderson GM (2006) Seasonal trace-element and stable-isotope variations in a Chinese speleothem: The potential for high-resolution. Earth Planet Sci Lett 244:394–407

Jones B, Kahle CF (1993) Morphology relationships, and origin of fiber and dendrite calcite crystals. J Sediment Petrol 63:1018–1031

Kathayat G, Cheng H, Sinha A, Spotl C, Edwards RL, Lui W, Zhang H, Cai Y, Breitenbach SFM (2016) Indian monsoon variability on millennial-orbital timescales over the past 282,000 years. Sci Rep 10:20–20

Kaufmann G (2003) Stalagmite growth and palaeo-climate: the numerical perspective. Earth Planet Sci Lett 214:251–266

Kelly MJ, Edwards RL, Cheng H, Yuan DX, Cai Y, Zhang ML, Lin YS, An ZS (2006) High resolution characterization of the Asian Monsoon between 146,000 and 99,000 years B.P. from Dongge Cave, China. Palaeogeogr Palaeoclim Palaeoecol 236:20–38

Kendall AC (1993) Columnar calcite in speleothems-discussion. J Sediment Petrol 63(3):550–552

Kotlia BS, Ahmad SM, Zhao JX, Raza W, Collerson KD, Joshi LM, Sanwal J (2012) Climatic fluctuations during the LIA and post-LIA in the Kumaun Lesser Himalaya, India: evidence from a 400 yr old stalagmite record. Quat Int 263:129–138

Kotlia BS, Singh AK, Joshi LM, Dhaila BS (2015) Precipitation variability in the Indian Central Himalaya during last ca. 4000 years inferred from a speleothem record: impact of Indian Summer Monsoon (ISM) and Westerlies. Quat Int 371:244–253

Kotlia BS, Singh AK, Sanwal J, Raza W, Ahmad SM, Joshi LM, Sirohi M, Sharma AK, Sagar N (2016) Stalagmite inferred high resolution climatic changes through Pleistocene- Holocene transition in Northwest Indian Himalaya. J Earth Sci Clim Change 7:338

Ku TL, Li HC (1998) Speleothems as high-resolution paleoenvironment archives: records from northeastern China. J Earth Syst Sci 107(4):321–330

Laskar AH, Yadava MG, Ramesh R, Polyak VJ, Asmerom Y (2013) A 4 kyr stalagmite oxygen isotopic record of the past Indian Summer Monsoon in the Andaman Islands. Geochem Geophys Geosyst 14(9):3555–3566

Lauritzen SE (1995) High-resolution paleotemperature proxy record for the Last Interglaciation based on Norwegian speleothems. Quat Res 43:133–146

Li W-X, Lundberg J, Dickin AP, Ford DC, Schwarcz HP, McNutt R, Williams D (1989) High precision mass-spectrometric uranium-series dating of cave deposits and implication for palaeoclimate studies. Nature 339:334–336

Liang F, Brook GA, Kotlia BS, Railsback LB, Hardt B, Cheng H, Edwards RL, Kandasamy S (2015) Panigarh cave stalagmite evidence of climate change in the Indian Central Himalaya since AD 1256: monsoon breaks and winter southern jet depressions. Quat Sci Rev 124:145–161

Lone MA, Ahmad SM, Dung NC, Shen CC, Raza W (2014) Speleothem based 1000-year high resolution record of Indian monsoon variability during the last deglaciation. Palaeogeogr Palaeoclim Palaeoecol 395:1–8

Longman MW, Brownlee DN (1980) Characteristics of karst topography, Palawan, Philippines. Z für Geomorphol 24:299–317

Mangini A, Verdes P, Spötl C, Scholz D, Vollweiler N, Kromer B (2007) Persistent influence of the North Atlantic hydrography on Central European winter temperature during the last 9,000 years. Geophys Res Lett 34:L02704

McDermott F (2004) Palaeo-climate reconstruction from stable isotope variations in speleothems. Quat Sci Rev 23:901–918

McDermott F, Frisia S, Huang Y, Longinelli A, Spiro B, Heaton THE, Hawkesworth CJ, Borsato A, Keppens E, Fairchild IJ, VanderBorg K, Verheyden S, Selmo E (1999) Holocene climate variability in Europe: evidence from $\delta^{18}O$ and textural variations in speleothems. Quat Sci Rev 18:1021–1038

McDermott F, Schwarcz HP, Rowe PJ (2006) Isotopes in speleothems. In: Leng MJ (eds) Isot Palaeoenviron Res, Springer 10:185–226

Moerrman JW, Cobb KM, Adkins JF, Sodemann H, Clark B, Tuen AA (2013) Diurnal to interannual rainfall $\delta^{18}O$ variations in northern Borneo driven by regional hydrology. Earth and Planetary Science Letters 369–370:108–119

Neff U, Burns SJ, Mangini A, Mudelsee M, Fleitmann D, Matter A (2001) Strong coherence between solar variability and the monsoon in Oman between 9 and 6 kyr ago. Nature 411:290–293

Niggemann S, Mangini A, Richter DK, Wurth G (2003) A paleoclimate record of the last 17,600 years in stalagmites from the B7 cave, Sauerland, Germany. Quat Sci Rev 22:555–567

O'Neil JR, Clayton RN, Mayeda TK (1969) Oxygen isotope fractionation in divalent metal carbonates. J Chem Phys 51:5547–5558

Paulsen DE, Li HC, Ku TL (2003) Climate variability in central China over the last 1270 years revealed by high-resolution stalagmite records. Quat Sci Rev 22:691–701

Plummer LN, Wigley TML, Parkhurst DL (1978) The kinetics of calcite dissolution in CO_2-water systems at 5 to 60 °C and 0.0 to 1.0 atm CO_2. Am J Sci 278:179–216

Polyak VJ, Asmeron Y (2001) Late Holocene climate and cultural changes in the Southwestern United States. Science 294:148–151

Proctor CJ, Baker A, Barnes WL, Gilmour MA (2000) A thousand year speleothem proxy record of North Atlantic climate from Scotland. Clim Dyn 16:815–820

Railsback LB, Brook GA, Chen J, Kalin R, Fleisher CJ (1994) Environmental controls on the petrology of a late Holocene speleothem from Botswana with annual layers of aragonite and calcite. J Sediment Res 64(1a):147–155

Repinski P, Holmgren K, Lauritzen SE, Lee-Thorp JA (1999) A late–Holocene climate record from a stalagmite, Cold Air Cave, Northern Province, South Africa. Palaeogeogr Palaeoclim Palaeoecol 150:269–277

Richards DA, Dorale JA (2003) Uranium-series chronology and environmental applications of speleothems. Rev Mineral Geochem 52:407–460

Rozanski K, Araguás-Araguás L, Gonfiantini R (1993) Isotopic patterns in modern global precipitation. In: Swart PK et al. (eds) Climate change in continental isotopic record, American Geophysical Union Monograph, vol 78, pp 1–36

Sanwal J, Kotlia BS, Rajendran C, Ahmad SM, Rajendran K, Sandiford M (2013) Climatic variability in central Indian Himalaya during the last 1800 years: evidence from a high resolution speleothem record. Quat Int 304:183–192

Schwarcz HP (1986) Geochronology and isotopic geochemistry of speleothems. In: Fritz P, Fontes JC (eds) Handbook of environmental isotope geochemistry. Elsevier, Amsterdam, pp 271–303

Self CA, Hill CA (2003) How speleothems grow: an introduction to the ontogeny of cave minerals. J Cave and Karst Stud 65(2):130–151

Shakun JD, Burns SJ, Fleitmann D, Kramers J, Matter A (2007) A high resolution, absolute-dated deglacial speleothem record of Indian Ocean climate from Socotra Island. Earth Planet Sci Lett 259:442–456

Shen C-C, Edwards RL, Cheng H, Dorale JA, Thomas RB, Moran SB, Weinstein SE, Hirschmann M (2002) Uranium and thorium isotopic and concentration measurements by magnetic sector inductively coupled plasma mass spectrometry. Chem Geol 185:165–178

Shindell DT, Schmidt GA, Mann ME, Rind D, Waple A (2001) Solar forcing of regional climate change during the Maunder Minimum. Science 294:2149–2152

Sinha A, Cannariato KG, Stott LD, Li HC, You CF, Cheng H, Edwards RL, Singh IB (2005) Variability of Southwest Indian summer monsoon precipitation during the Bølling–Ållerød. Geology 33:813–816

Sinha A, Cannariato KG, Stott LD, Cheng H, Edwards RL, Yadava MG, Singh IB (2007) A 900-year (600–1500 A.D.) record of the Indian summer monsoon precipitation from the core monsoon zone of India. Geophys Res Lett 34(16):L16707

Sinha A, Berkelhammer M, Stott L, Mudelsee M, Cheng H, Biswas J (2011) The leading mode of Indian Summer Monsoon precipitation variability during the last millennium. Geophys Res Lett 38:L15703

Sinha A, Kathayat G, Cheng H, Breitenbach SFM, Berkelhammer M, Mudelsee M, Biswas J, Edwards RL (2015) Trends, oscillations and anomalies in the Indian Summer Monsoon rainfall over the last two millennia. Nature Communications 6(6309):1–8

Spötl C, Mangini A (2002) Stalagmite from the Austrian Alps reveals Dansgaard-Oeschger events during isotope stage 3: implications for the absolute chronologyof Greenland ice cores. Earth and Planet Sci Lett 203:507–518

Spötl C, Mangini A, Richards DA (2006) Chronology and paleoenvironment of Marine Isotope Stage 3 from two high-elevation speleothems, Austrian Alps. Quat Sci Rev 25(9–10):1127–1136
Sweeting MM (1972) Karst landforms. Macmillan, London, p 362
Talma AS, Vogel JC (1992) Late Quaternary paleotemperatures derived from a speleothem from Cango Caves, Cape Province, South Africa. Quat Res 37:203–213
Thompson P, Schwarcz H, Ford D (1974) Continental Pleistocene climatic variations from speleothem age and isotopic data. Science 184(4139):893–895
Vacco DA, Clark PU, Mix AC, Cheng H, Edwards RL (2005) A speleothem record of Younger Dryas cooling, Klamath Mountains, Oregon, USA. Quat Res 64:249–256
Vaupotič J, Kobal I (2004) Radon doses based on Alpha spectrometry. Acta Chim Slov 51:159–168
Vollweiler N, Scholz D, Mühlinghaus C, Mangini A, Spötl C (2006) A precisely dated climate record for the last 9 kyr from three high alpine stalagmites, Spannagel Cave Austria. Geophys Res Lett 33(L20703):1–5
Wang YJ, Cheng H, Edwards RL, An ZS, Wu JY, Shen C-C, Dorale JA (2001) A high-resolution absolute-dated late Pleistocene monsoon record from Hulu Cave. Science 294:2345–2348
Wang YJ, Cheng H, Edwards RL, He Y, Kong XG, An ZS, Wu JY, Kelly MJ, Dykoski CA, Li XD (2005) The Holocene Asian monsoon: links to solar changes and North Atlantic climate. Science 308:854–857
Wang Y, Cheng H, Edwards RL, Kong X, Shao X, Chen S, Wu J, Jiang X, Wang X, Zhisheng A (2008) Millenial and orbital scale changes in the East Asian monsoon over the past 224,000 years. Nature 451:1090–1093
White WB (1988) Geomorphology and Hydrology of Karst Terrains. Oxford University press, p 464
White WB (1997) Thermodynamic equilibrium, kinetics, activation barriers, and reaction mechanisms for chemical reactions in karst terrains. Environ Geol 30(1/2):46–58
Yadava MG (2002) Stable isotope systematics in cave calcites: Implications to past climatic changes in tropical India, Ph.D. thesis. Physical Research Laboratory, Navrangpura, India, pp 1–197
Yadava MG, Ramesh R (2005) Monsoon reconstruction from radiocarbon dated tropical Indian speleothems. The Holocene 15:48–59
Yadava MG, Ramesh R (2006) Stable oxygen and carbon isotope variations as monsoon proxies: a comparative study of speleothems from four different locations in India. J Geol Soc India 68:461–475
Yadava MG, Ramesh R, Pant GB (2004) Past monsoon rainfall variations in peninsular India recorded in a 331-year-old speleothem. Holocene 14:517–524
Yang Y, Yuan DX, Cheng H, Zhang ML, Qin JM, Lin YS, Zhu XY, Edwards RL (2010) Precise dating of abrupt shifts in the Asian Monsoon during the last deglaciation based on stalagmite data from Yamen Cave, Guizhou Province, Science China. Earth Sci 53:633–641
Zhang P, Cheng H, Edwards RL, Chen F, Wang Y, Yang X, Liu J, Tan M, Wang X, Ji Liu, An C, Dai Z, Zhou J, Zhang D, Jia J, Jin L, Johnson KR (2008) A test of climate, sun and culture relationships from an 1810-Year Chinese cave record. Science 322(5903):940–942
Zhou H, Zhao J, Feng Y, Gagan MK, Zhou G, Yan J (2008) Distinct climate change synchronous with Heinrich event one, recorded by stable oxygen and carbon isotopic compositions in stalagmites from China. Quat Res 69:306–315

Chapter 3
Studied Speleothems and Methodology

3.1 Description and Geology of Cave Sites

Considering the vast expansion of limestone host rock throughout the Himalaya, we studied six caves in the different sectors (Fig. 3.1) under varying precipitation regimes. These are, Kalakot Cave (33°13′19″ N: 74°25′33″ E; altitude, 826 m) from Jammu and Kashmir; Borar Cave (30°38′18″ N: 77°39′09″ E; altitude, 1622 m) and Tityana Cave (30°38′30.7″ N: 77° 39′07.4″ E; altitude, 1470 m) from Himachal Pradesh; Dharamjali Cave (29°31′27.8″ N: 80°12′40.3″ E; altitude, 2200 m), Sainji Cave (30°16′07″ N: 79°18′14″ E; altitude, 1478 m) and Chulerasim Cave (29°53′08″ N: 79°21′06″ E; altitude, 1254 m) from Uttarakhand.

Kalakot Cave is about 5 m long (entrance 1.8 m × 1.5 m, Fig. 3.2a) and is almost horizontal. The thickness of host rock (Sirban Limestone) above the cave is 50 m (Fig. 3.2b). The vegetation above the cave is dominated by broad leaved elements followed by pine trees. We observed 6 stalagmites of varying heights and a 19.6 cm long stalagmite (Fig. 3.2c–d) was collected. It was the longest inactive stalagmite and was collected at a distance of about 2.2 m from the main entrance. The composition of stalagmite is calcite with very well developed growth rings showing no discontinuity (Fig. 3.2e). The inside temperature and humidity at the time of collection of the sample was 10.6 °C and 79% respectively.

In the Kalakot region, the Sirban limestone (Fig. 3.3) is underlain by Jangli Formation (Subathu Group) and an unconformity lies between these (Mathur and Juyal 2000). In the study area, the Sirban limestone is exposed as occupying the crestal part of anticlinal features (Siddai and Shukla 2012). The presence of stromatolites suggests a Neoproterozoic age for the Sirban limestone (Raha and Sastry 1982).

Sainji Cave is located in the Almora District, Ranikhet Tehsil in the Kumaun Himalaya. This is a 32 m long cave with an entrance of 1.5 m^2 (Fig. 3.4a). The entrance of the cave is sub vertical (Fig. 3.4b), middle part almost vertical and then horizontal till the end. At the time of collection of specimen, the mean annual temperature around the cave site was ∼13.5 °C and the inside humidity was measured as 70%. The host rock above the cave is 50 m thick Deoban limestone. Several structures like stalactites, stalagmites and flow stones were observed inside the cave. The surrounded

A. K. Singh, *High Resolution Palaeoclimatic Changes in Selected Sectors of the Indian Himalaya by Using Speleothems*, Springer Theses,
https://doi.org/10.1007/978-3-319-73597-9_3

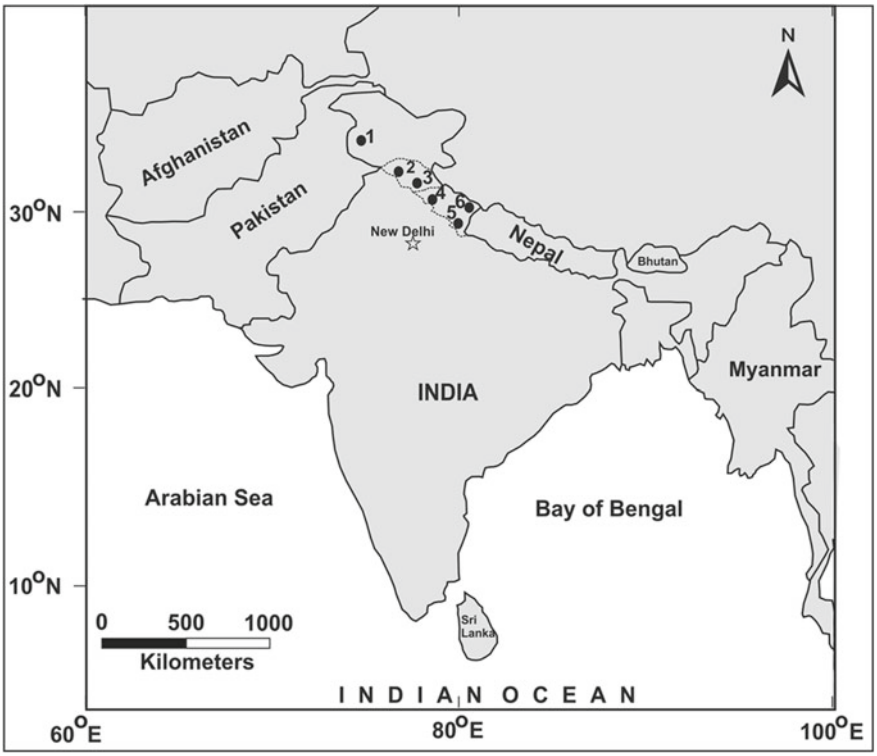

Fig. 3.1 Caves studied in the present work. 1—Kalakot (Jammu and Kashmir); 2—Borar and 3—Tityana (Himachal Pradesh); 4—Chulerasim, 5—Sainji and 6—Dharamjali (Uttarakhand)

area is dominated by the *Pinus roxburghii* with small shrubs, grasses and scattered *Quercus*. The cave is situated in subtropical climate with wetter and warmer summers and cooler and drier winters. The selected specimen, 26 cm in length (Fig. 3.4c–d) was collected from the last narrowest chamber (0.8 m × 0.7 m), about 31.5 m from the entrance.

Chulerasim Cave is situated near Chulerasim village, Chaukhtia (District Almora) in the Kumaun Lesser Himalaya. This is a 5 m long cave with main entrance as ~3 m × 3 m (Fig. 3.5a) and very narrow end. The 11.5 cm long active stalagmite (Fig. 3.5c–d) was collected at a distance of 4.9 m from the entrance. The vegetation around the cave area is dominated by *Quercus incana*, *Pinus roxburghii* and small shrubs. The yearly weather is sub-tropical wet/moist with warmer summers and cooler winters. The humidity outside the cave varies between 60 and 70% during the ISM period and 30–40% during the WDs months. The drip rate inside the cave was 1 drop/min, when specimen was collected.

The Sainji and Chulerasim Caves are situated in the Tejam group of rocks (Deoban and Mandhali formation) (Valdiya 1980). The caves are formed mainly in the rocks of the Deoban formation (Fig. 3.6). This formation is marked by stromatolite bear-

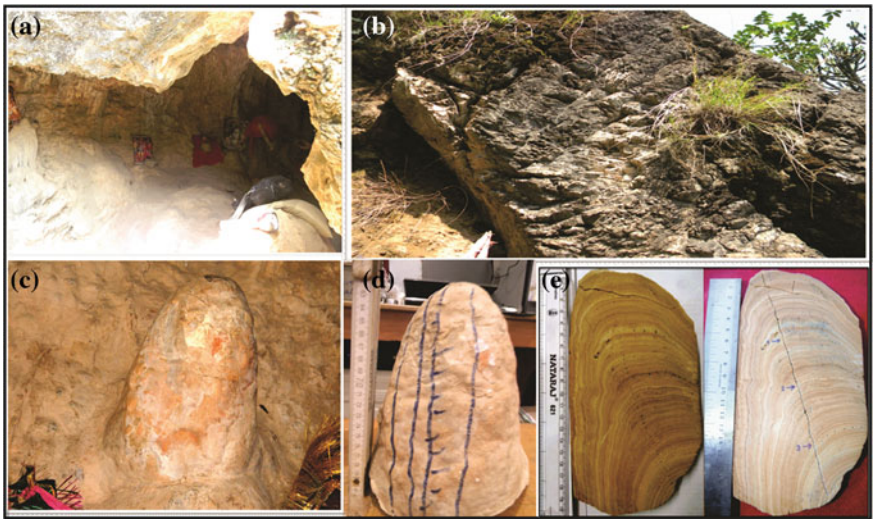

Fig. 3.2 **a** Entrance of the Kalakot Cave (1.8 m × 1.5 m); **b** Overlying limestone; **c** Ideal shape of stalagmite inside the cave; **d** Kalakot stalagmite after collection; **e** Sliced parts of the stalagmite with growth rings

ing cherty dolomite and dolomite limestone bands. The limestone and slate occur as intercalation and overlies with Rautgara Formation (Valdiya 1962, 1980) as a conformable contact. The age of Deoban limestone is Riphean (1400–800 Ma) (Srivastava and Kumar 1997).

Dharamjali Cave is located 7 km south-west of Pithoragarh. The sub-vertical cave is 35 m long with an entrance of 4.5 m × 2 m (Fig. 3.7a) from where the cave dips 60° NW at an angle of 40–45°. The cave is very narrow in the last chamber (ca 0.8 m × 0.9 m). It has structures like stalagmites, stalactites, pillars and flowstones (Fig. 3.7b). We collected five stalagmites of various heights. In the present study, we used a 41 cm long stalagmite (Fig. 3.7c–d) which was collected at a distance of about 34 m from the entrance. The thickness of the host rock above the cave is about 50 m with a 1–2 m thick brownish black soil. The vegetation is dominated by *Quercus* and *Rhododendron* with occasional occurrences of *Pinus roxburghii*, as well as small shrubs, grasses, ferns and herbs. The cave is wet throughout the year with highest dripping rate during the monsoon season and minimum water supply occurs during winter.

Dharamjali Cave is situated in the Mandhli (Sor and Thalkedar) Formation (e.g., Nautiyal 1990). This formation consists mainly of greyish green and black carbonaceous pyritic phylites-slates, interbedded limestone with paraconglomerate. The Mandhali Formation occurs in the core of Gangolihat Dolomite Formation. The sedimentary rocks have been designated as Sor slates and Thalkedar limestone (Fig. 3.8). The age of this Formation is Riphean to Vendian (1600−540 Ma) (Valdiya 1980, 1989).

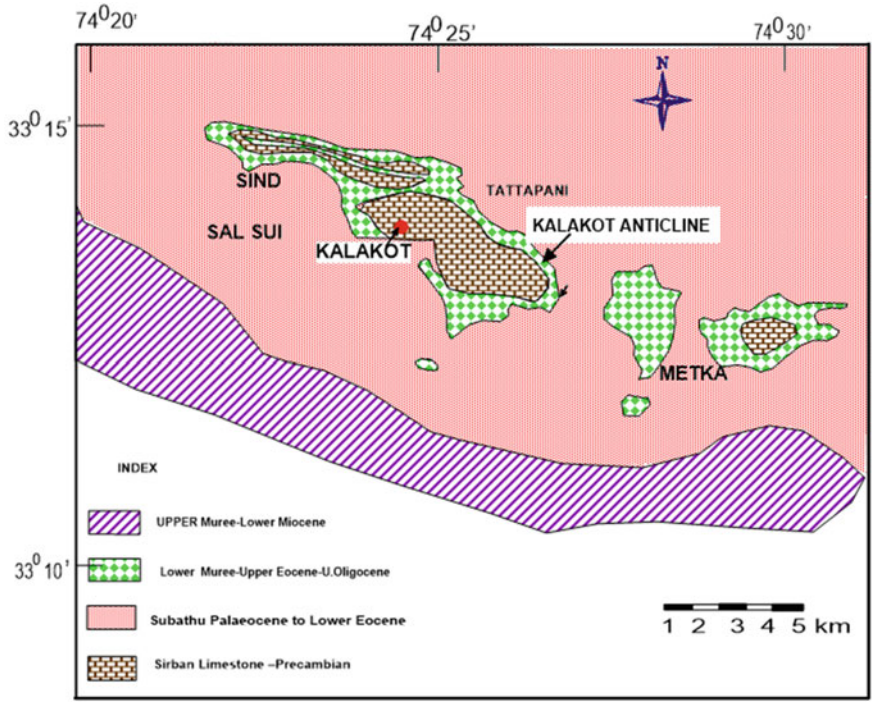

Fig. 3.3 Geological map of the area around Kalakot (modified after Khan 1973)

Fig. 3.4 **a** Entrance of the Sainji Cave; **b** Entrance becomes narrower in the middle part of the cave; **c** Collected specimen inside the cave; **d** Stalagmite in the laboratory after collection; **e** Sliced parts of the stalagmite

Tityana Cave is 13 m and long sub vertical with a small entrance (3 m × 1 m, Fig. 3.9a). The host rock thickness is 2 m. Two stalagmites were collected at distance of about 12.1 and 12.9 m respectively from the main entrance. The cave is dry and has flow stones, stalactites and unbroken stalagmites. In the present study, we selected

Fig. 3.5 **a** Entrance of the Chulerasim Cave; **b** Host rock above the cave; **c** Collected specimen (11.5 cm long) from the cave; **d** Sliced parts of the sample

a 13 cm long stalagmite (Fig. 3.9c–d). Structures like stalactites, stalagmites and flowstones are present inside the cave. The surrounding vegetation is dominated by *Pinus* trees along with shrubs. This cave has three chambers, two chambers have a slant of 60°–70° from main entrance and the last chamber is sub-horizontal.

Borar Cave is a 5.5 m long and is sub horizontal to sub vertical with a ceiling height of 2 m. The cave has very small entrance of 2 m × 1 m (Fig. 3.10a). The host rock thickness is about 20 m. While collecting the sample, the temperature and humidity inside the cave were 16.1 °C and 78% respectively. The surrounding vegetation is dominated by broad leaved sub-tropical forests and a lot of ferns. Stalagmites, stalactites and flowstones are present in the cave (Fig. 3.10b). Four stalagmites were collected at a distance of 2 m from the main entrance. We used a 23.6 cm long stalagmite in the present study (Fig. 3.10c–d). The sliced part of the sample shows dark rings (Fig. 3.10e). The drip rate inside the cave was 9 drops/min at the time of sample collection.

The Tityana and Borar Caves are located in the Deoban limestone (Fig. 3.11) of Precambrian age (Shali-Deoban Formation). This Deoban sequence begins with a red quartzite-limestone in the basal part, followed by a shale/slate series and grey

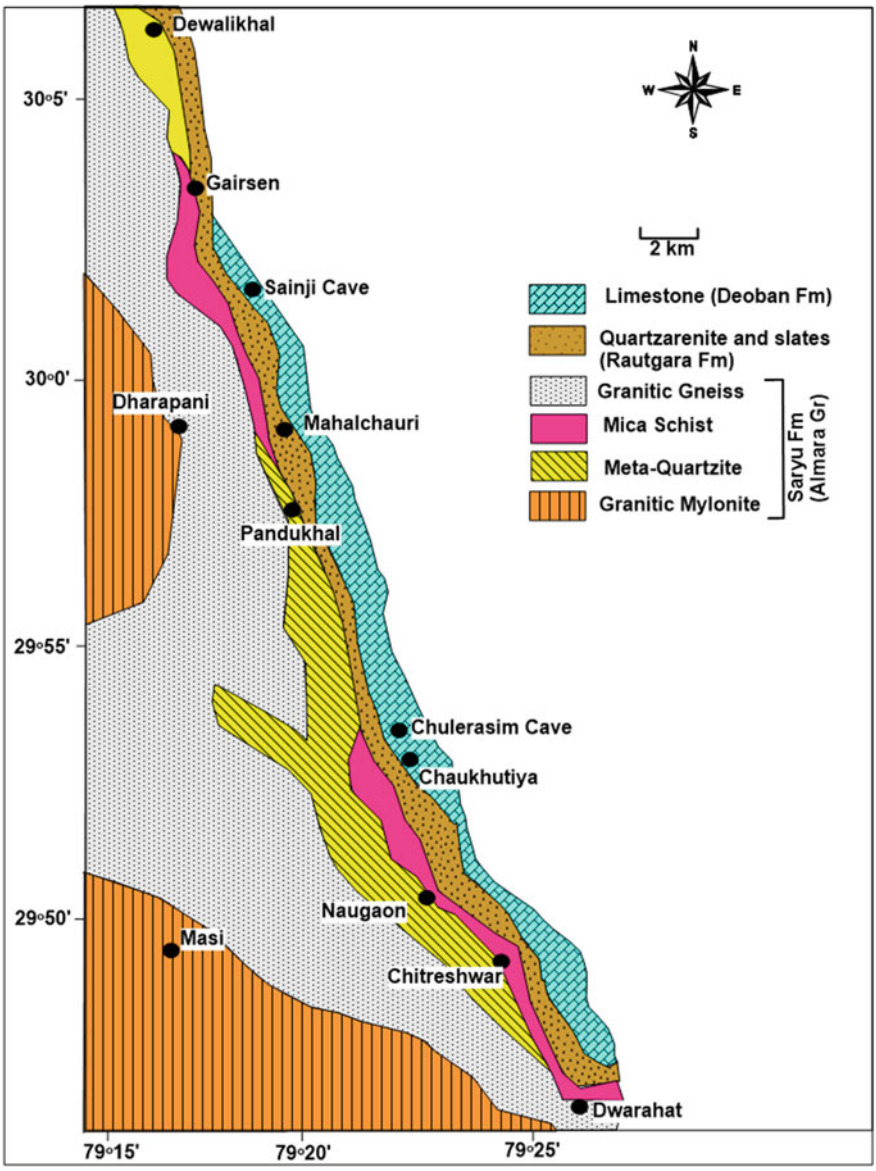

Fig. 3.6 Geological map around Sainji and Chulerasim Caves (after Valdiya 1980)

dolomite in middle and upper parts (Bhargava 1976). Based on the characteristic stromatolites, the Deoban Formation has been assigned a Mesoproterozoic age (Valdiya 1969; Thakur and Rawat 1992).

Fig. 3.7 **a** Entrance of the Dharamjali Cave; **b** Structures like stalactites, stalagmites, flow stones etc.; **c** Stalagmite inside the cave; **d** Sliced part of the stalagmite

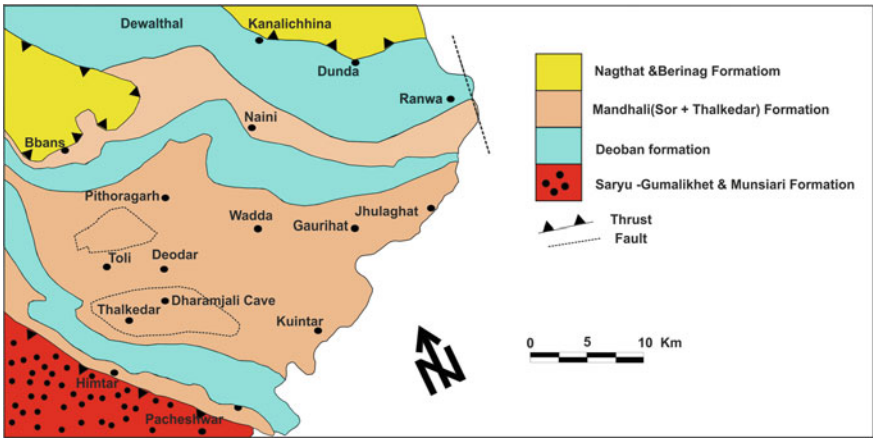

Fig. 3.8 Geology around Dharamjali Cave area (after Valdiya 1980)

3.2 Meteorological Data Around Cave Sites

We examined the precipitation data of six meteorological stations (1900–2000, http://www.indiawaterportal.org/met_data/), which are near by the studied caves. The data of all stations for ISM and WDs, display a variation in the minimum and maximum values of annual mean precipitation (Fig. 3.12). The maximum annual precipitation of all stations is about three times larger than minimum annual precipitation. The mean annual precipitation amount suggests that the ISM has a major role in different sectors of the Himalaya from Uttarakhand to Jammu and Kashmir. The meteorological data suggest that the ISM intensity decreases from east (Uttarakhand, ~2090 mm) to Northwest (Jammu and Kashmir, ~1352 mm) in the Himalayan region. However the WDs play a very significant role in total annual precipitation in Jammu and Kashmir (Table 3.1).

Fig. 3.9 **a** Entrance of the Tityana Cave; **b** Entrance becomes narrower inside the cave; **c** 13 cm long stalagmite inside the cave; **d** Sliced parts of the stalagmite

3.3 Methodology Adopted in the Present Study

3.3.1 U/Th Dating

Selected stalagmites were sliced into two halves, for dating, isotopic study and mineralogical analyses. For U/Th dating, the samples were drilled with sample size smaller than 5 mm. All samples were analysed by Thermal Ionisation Mass Spectrometry (TIMS) at Heidelberg Academy of Sciences, Germany and University of Queensland, Australia. Methods used for sample preparation and mass spectrometric analysis are explained in detail by Frank et al. (2000), Burns et al. (2002), Holzkämper et al. (2005), Kotlia et al. (2012). Samples were dissolved in 7 N HNO_3 and equilibrated with a mixed spike containing ^{229}Th, ^{233}U, and ^{236}U. The U and Th were separated using two stages of HNO_3–HCl cation exchange chemistry followed by reaction with HNO_3 and $HClO_4$ to remove any residual organic material. The Ages were calculated using Isoplot (Ludwig 2003) and the decay constants of Jaffey et al. (1971). The StalAge (age-depth) model was performed following Scholz and Hoffmann (2011). Age uncertainties are at 2-σ level and do not include half-life uncertainties.

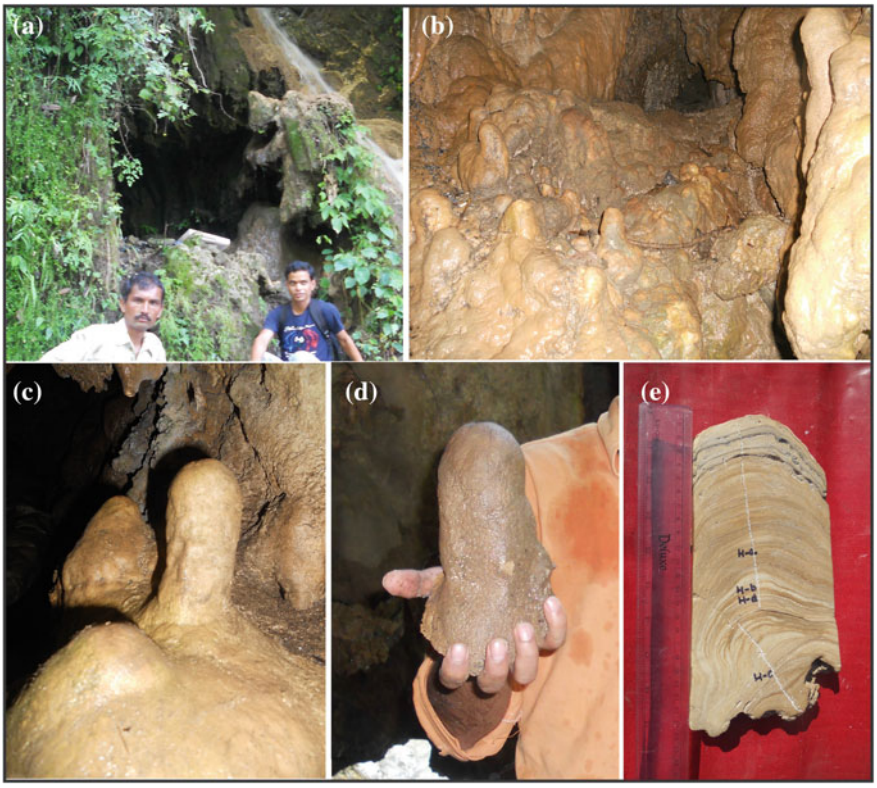

Fig. 3.10 **a** Entrance of the Borar Cave; **b** Different cave structures inside the cave; **c** 23.6 cm long stalagmite inside the cave; **d** Stalagmite sample outside the cave; **e** Sliced part of the sample

3.3.2 AMS Dating

In some stalagmites, the U/Th method was unsuccessful due to multiple source of non-authigenic ^{232}Th and low uranium concentration (<10 ppb). Thus, the AMS chronology was introduced for such stalagmites. Only one stalagmite from Tityana Cave was dated by AMS method. All samples were drilled at different depths using dental drill for ^{14}C AMS chronology and were analyzed at Poznań Radiocarbon Laboratory, Poland. The AMS measurements are dedicated to the ^{14}C because the Carbon-14 is a naturally occurring radioactive isotope of carbon. For AMS dating, the sample size is very less as 1–2 mg and in few cases as small as 50–100 micrograms. This technique determines the isotopic composition of a sample by first generating a negatively-charged ion beam, which is then subjected to a series of selective filtering procedures in order to get ^{14}C. This method is based on ^{14}C/^{12}C ratios in the range of 10^{-12}–10^{-15}. Thus, the AMS method has successfully been applied to build chronologies for young speleothems (Goslar et al. 2000; Mattey et al. 2008;

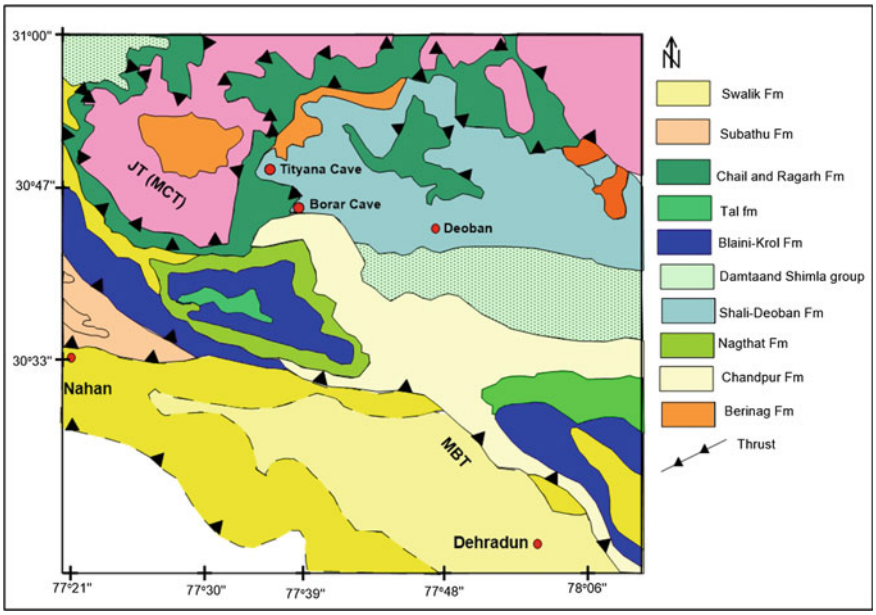

Fig. 3.11 Geological map around Tityana and Borar Caves (after Thakur and Rawat 1992)

Table 3.1 Precipitation data between 1900 and 2000 from the different meteorological stations (http://www.indiawaterportal.org/met_data)

S. No.	Meteorological station	Nearest Cave	Annual mean precipitation (mm)		ISM maximum (mm)	WDs maximum (mm)
			Minimum	Maximum		
1	Rajouri District (J&K)	Kalakot Cave	412	1352	1107	478
2	Almora (UK)	Sainji Cave	627	2199	1005	323
3	Pithoragarh (UK)	Dharamjali Cave	581	2037	1966	509
4	Nainital (UK)	Chulerasim Cave	580	2037	1917	280
5	Sirmour District (HP)	Borar Cave	433	1322	1228	263
6	Simla (HP)	Tityana Cave	548	1588	1359	341

Laskar et al. 2013; Zhao et al. 2015). All obtained AMS ages were calibrated using online Cal Pal program to convert the conventional radiocarbon dates into calendar ages. The Age/depth model was constructed by linear interpolation between the calibrated ages.

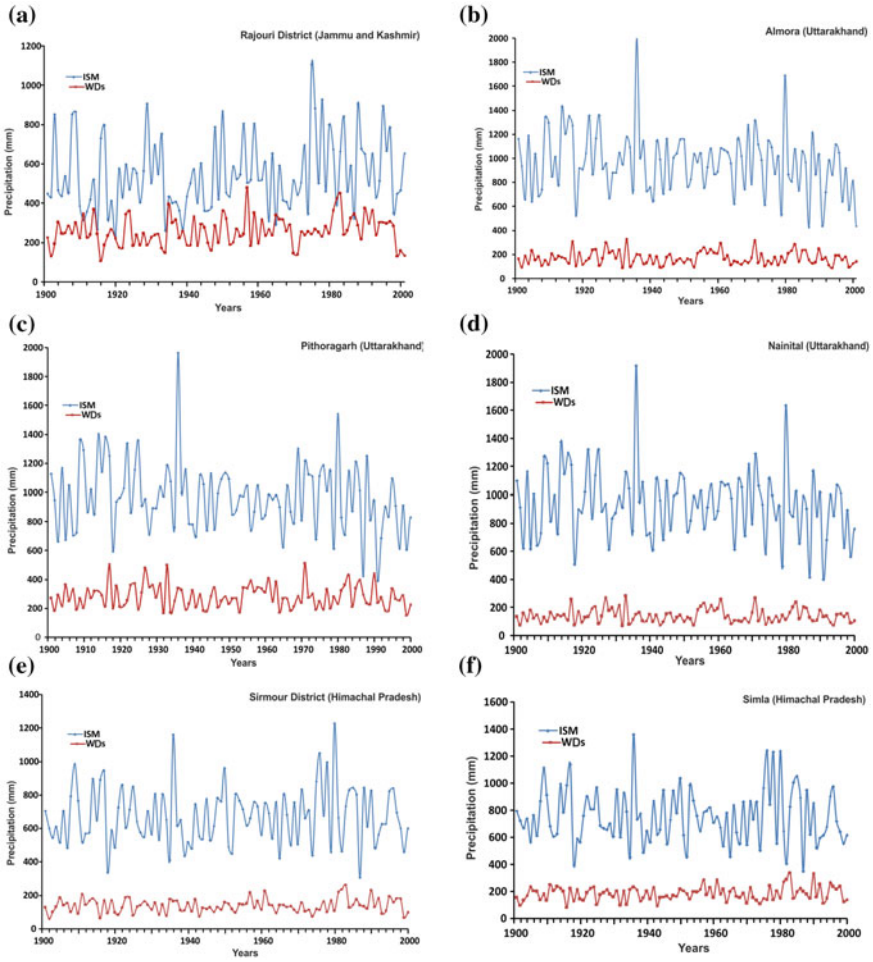

Fig. 3.12 Meteorological data from different districts around studied caves (data from http://www.indiawaterportal.org/metdata), **a** Rajouri District (J&K); **b** Almora (UK); **c** Pithoragarh (UK); **d** Nainital (UK); **e** Sirmour District (HP) and **f** Simla (HP)

3.3.3 $\delta^{18}O$ and $\delta^{13}C$ Isotopes

For isotopic analysis, the sub samples were drilled at every 0.8 mm along the growth axis (Fig. 3.13) by using a triaxial drill machine at National Geophysical Research Institute (NGRI) Hyderabad.

The Hendy test was performed on selected layers (from centre to right of the growth axis) at various depths to understand whether the deposition of the stalagmite carbonates was in isotopic equilibrium with precipitating waters (Hendy 1971). All the isotopic measurements were carried out using a Delta plus Isotope Ratio Mass Spectrometer (IRMS) coupled with Kiel-IV automatic carbonate device (Fig. 3.13).

Fig. 3.13 **a** Triaxial drilling machine for isotopic analysis; **b–c** Isotope Ratio Mass Spectrometer (IRMS) coupled with a Kiel-IV automatic carbonate device at NGRI Hyderabad

The obtained isotopic values are reported in δ notation as permil deviation from PDB standard (Spötl and Mattey 2006). The Analytical precision was better than 0.10‰ for $\delta^{18}O$ and 0.05‰ for $\delta^{13}C$. The calibration standard was achieved by repeated measurements of international reference standards NBS19 and NBS18 (Ahmad et al. 2008). The standard used is V-PDB supplied by IAEA (International Atomic Energy Agency, Vienna).

3.3.4 Petrography and SEM

For laminae analysis, the polished surfaces of stalagmites were scanned using a pre-calibrated high resolution scanner at RGB/3200 dpi. The X-Ray Diffraction (XRD) method was involved in identification of the mineralogical composition of the sample. The Scanning Electron Microscope (SEM) was used for determining the structure and composition of the stalagmite by coating the fresh broken surface of the sub-sample by carbon to provide electrical conductivity to the surface. Mineralogy, surface morphology and crystal composition of the stalagmites were determined by using petrographic microscope as well as Scanning Electron Microscope (SEM). The analysis was performed at Jawaharlal Nehru Centre for Advance scientific Research (JNCASR), Bangalore, India.

3.3.5 Abbreviations of Studied Cave Stalagmites

See Table 3.2.

Table 3.2 Abbreviations used for studied stalagmites

S. No.	Cave stalagmite	Abbreviation
1	Kalakot	KL-3
2	Sainji	SA-1
3	Chulerasim	CH-1
4	Dharamjali	DH-1
5	Tityana	TCS
6	Borar	BR-2

References

Ahmad SM, Babu A, Padmakumari GVM, Raza W (2008) Surface and deep water changes in the northeast Indian Ocean during the last 60 ka inferred from carbon and oxygen isotopes of planktonic and benthic foraminifera. Palaeogeogr Palaeoclimatol Palaeoecol 262:182–188

Bhargava ON (1976) Geology of the Krol Belt and associated formations: a reappraisal. Memoirs Geol Surv India 106(1):167–234

Burns SJ, Fleitmann D, Mudelsee M, Neff U, Matter A, Mangini A (2002) A 780-year annually resolved record of Indian Ocean monsoon precipitation from a speleothem from south Oman. J Geophys Res 107(D20):4434

Frank N, Braum M, Hambach U, Mangini A, Wagner G (2000) Warm period growth of travertine during the last interglaciation in southern Germany. Quat Res 54:38–48

Goslar T, Hercman H, Pazdur A (2000) Comparison of U-series and radiocarbon dates of speleothems. Radiocarbon 42(3):403–414

Hendy CH (1971) The isotopic geochemistry of speleothems-I. The calculation of the effects of different modes of formation on the isotopic composition of speleothems and their applicability as paleoclimatic indicators. Geochim Cosmochim Acta 35:801–824

Holzkämper S, Spotl C, Mangini A (2005) High-precision constraints on timing of Alpine warm periods during the middle to late Pleistocene using speleothem growth periods. Earth Planet Sci Lett 236:751–764

http://www.indiawaterportal.org/met_data/

Jaffey AH, Flynn KF, Glendenin LE, Bentley WC, Essling AM (1971) Precision measurement of half-lives and specific activities of ^{235}U and ^{238}U. Phys Rev Lett C 4(5):1889–1906

Khan A (1973) A new mammalian fossil from the Lower Murree of Kalakot, Jammu and Kashmir State, India. J Geol Soc India 14(3):296–301

Kotlia BS, Ahmad SM, Zhao JX, Raza W, Collerson KD, Joshi LM, Sanwal J (2012) Climatic fluctuations during the LIA and post-LIA in the Kumaun Lesser Himalaya, India: evidence from a 400 yr old stalagmite record. Quat Int 263:129–138

Laskar AH, Yadava MG, Ramesh R, Polyak VJ, Asmerom Y (2013) A 4 kyr stalagmite oxygen isotopic record of the past Indian Summer Monsoon in the Andaman Islands. Geochem Geophys Geosyst 14(9):3555–3566

Ludwig KR (2003) Mathematical-statistical treatment of data and errors for ^{230}Th/U geochronology. Rev Min Geochem 52:631–636

Mathur NS, Juyal KP (2000) Atlas of Early Palaeogene Invertebrate Fossils of the Himalayan Foothills Belt, Monogr. Wadia Institute of Himalayan Geology, Dehradun, p 257

Mattey D, Lowry D, Duffet J, Fisher R, Hodge E, Frisia S (2008) A 53 year seasonally resolved oxygen and carbon isotope record from a modern Gibraltar speleothem: reconstructed drip water and relationship to local precipitation. Earth Planet Sci Lett 269:80–95

Nautiyal AC (1990) Microfacies microfossils (organic-walled microfossils) in Middle Proterozoic, Tejam Group of Kumaon Lesser Himalaya and palaeoenvironmental significance. Palaeontol Soc India 35:177–187

Raha PK, Sastry MVA (1982) Stromatolites and Precambrian stratigraphy in India. Precambr Res 18:293–318

Scholz D, Hoffmann DL (2011) StalAge—an algorithm designed for construction of speleothem age models. Quat Geochronol 6:369–382

Siddai NS, Shukla MK (2012) Occurrence of rhyolite in Jangalgali Formation, Jammu and Kashmir, Northwest Himalaya, India. Curr Sci 103(7):817–821

Spötl C, Mattey D (2006) Stable isotope microsampling of speleothems for palaeoenvironmental studies: a comparison of microdrill, micromill and laser ablation techniques. Chem Geol 235:48–58

Srivastava P, Kumar S (1997) Significance of microfossil assemblage, Deoban Limestone, Garhwal Lesser Himalaya, Uttar Pradesh. Palaeobotanist 46(1, 2):7–12

Thakur VC, Rawat BS (1992) Geologic Map of Western Himalaya, 1:1,000,000. Wadia Institute of Himalayan Geology, Dehradun, India

Valdiya KS (1962) An outline of the stratigraphy and structure of the southern part of the Pithoragarh District, U.P. J Geol Soc India 3:27–48

Valdiya KS (1969) Stromatolites of the Lesser Himalayan carbonate formations and the Vindhyans. J Geol Soc India 10:1–25

Valdiya KS (1980) Geology of the Kumaun Lesser Himalaya. Wadia Institute of Himalayan Geology, Dehradun, pp 1–291

Valdiya KS (1989) Precambrian stromatolite biostratigraphy of India—a review. Himalayan Geol 13:181–214

Zhao M, Li HC, Liu ZH, Mii HS, Sun HL, Shen CC, Kang SC (2015) Changes in climate and vegetation of central Guizhou in southwest China since the last glacial reflected by stalagmite records from Yelang Cave. J Asian Earth Sci 114(3):549–561

Chapter 4
Results

4.1 Kalakot (KL-3) Stalagmite

4.1.1 Age/Depth Model

Four U/Th dates (Table 4.1) were obtained, i.e., 10, 10.4, 13.1 and 14.9 ka BP (Fig. 4.1a). The ^{230}Th dates from stalagmite and regression through origin indicate an age of 16.4 ka BP at the bottom and 9.5 ka BP near the top (Fig. 4.1b). The ages are similar by both methods. However, we used StalAge for further analysis interpretation. Based on the age model, the stalagmite covers a time span of 16.2–9.5 ka BP.

4.1.2 Hendy Test Results

We carried out the Hendy test on three layers (six samples from each layer) at depths of 6.5, 10.2 and 15.9 cm respectively (Fig. 4.2). The variations in δ^{18}O and δ^{13}C values for these layers are as follows: δ^{18}O (−6.44 to −8.07‰) and δ^{13}C (−6.44 to −8.07‰) for the first layer, δ^{18}O (−6.09 to −7.21‰) and δ^{13}C (−9.59 to −10.84‰) for the second layer and δ^{18}O (−6.54 to −7.59‰) and δ^{13}C (−8.21 to −8.59‰) for the third layer. The results show that (1) there is almost no enrichment of δ^{18}O towards the outer end, and (2) the correlation coefficient R^2 is low (>1) along these layers. It seems that the stalagmite was deposited under the isotopic equilibrium.

A. K. Singh, *High Resolution Palaeoclimatic Changes in Selected Sectors of the Indian Himalaya by Using Speleothems*, Springer Theses,
https://doi.org/10.1007/978-3-319-73597-9_4

Table 4.1 U/Th dates from Kalakot stalagmite (KL-3)

Sample code	Depth from top (cm)	δU (‰)	±2σ (abso.)	238U (ug/g)	±2σ (abso.)	^{232}Th (ng/g)	±2σ (abso.)	^{230}Th (pg/g)	±2σ (abso.)	Age_{uncorr} (ka BP)	Age_{corr} (ka BP)	Error in corr. ages (ka BP)
5190	1.6	129.1	16.0	0.05153	0.00010	4.92	0.054	0.103	0.010	12.5	10	1.8
5323	2.7	112.8	9.0	0.04284	0.00009	3.417	0.012	0.0842	0.0013	12.5	10.4	1.1
5324	9.5	120.0	5.9	0.05485	0.00011	7.503	0.059	0.1424	0.0048	16.7	13.1	1.9
5325	16.2	114.8	10.1	0.05622	0.00011	5.99	0.10	0.153	0.015	17.6	14.9	2.3

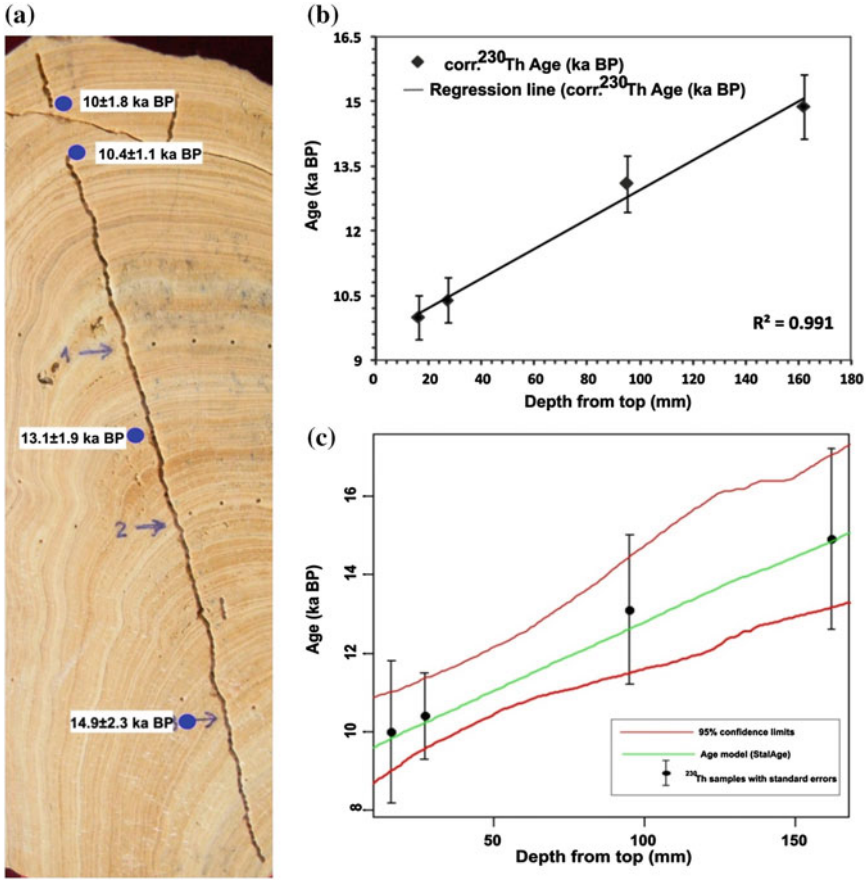

Fig. 4.1 **a** KL-3 with sampling points. Note the continuity in the deposition; **b** Corrected ^{230}Th dates and regression through the origin; **c** Age/depth relationship by StalAge (after Scholz and Hoffmann 2011). Black dots represent the individual age measurements

4.1.3 Mineralogy and Growth Rate

There is no hiatus, discontinuity and major lithological change on the polished surface (Fig. 4.1a). Sixteen SEM images were analyzed from different sections at an interval of 0.5 cm. The SEM images show that the stalagmite is mainly composed of calcite. Petrographic analysis under plane polarized light was performed on four thin sections at depths of 0–3.0, 3.5–6.5, 7.0–10.0 and 10.5–13.5 cm from the top.

Petrographic images at 3.5–6.5 cm depths show various calcite laminations (Fig. 4.3a–b) and the upper part shows high resolution image of flat-topped calcite layers (Fig. 4.3b). In general, the sample is mainly composed of finely laminated compact layers of calcite without much variation throughout excluding two thin porous layers at 6.2 and 10.3 cm. The flat-topped calcite layers possibly show sign

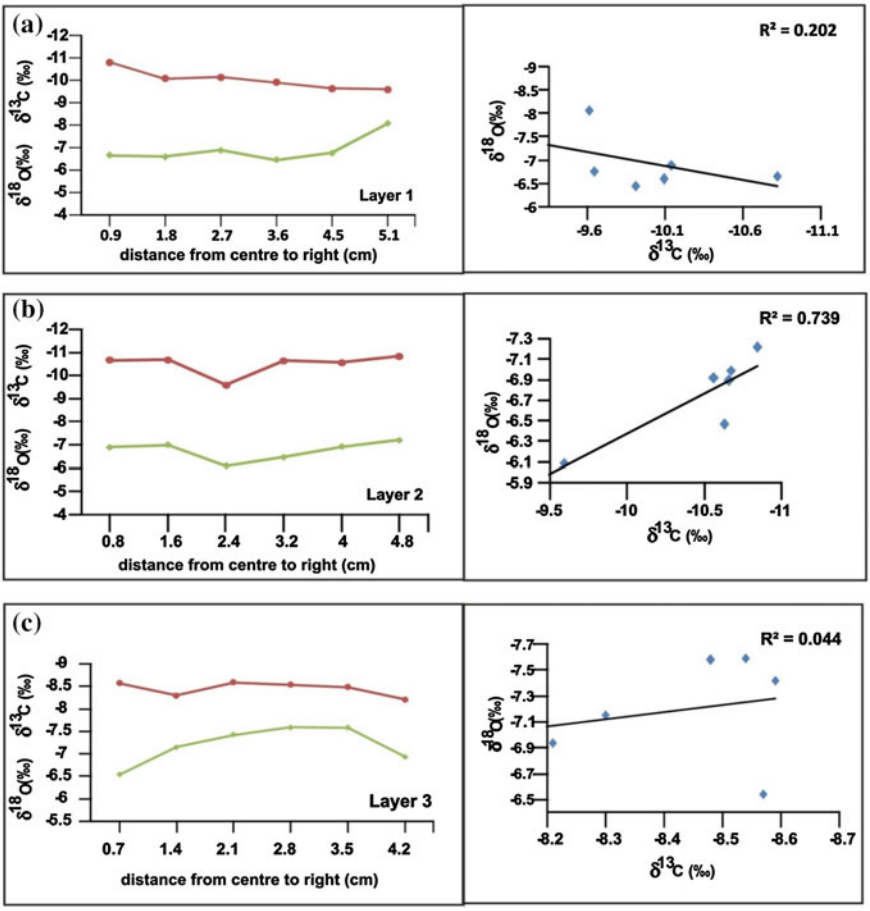

Fig. 4.2 Hendy test results: variations in $\delta^{18}O$ and $\delta^{13}C$ along three growth layers at 6.5, 10.2 and 15.9 cm from top of the stalagmite

of thin film of water on the surface of the growing KL-3. The SEM analysis at depth of 1.5 cm shows well-developed and long columnar calcite (CC), with clearly visible direction and termination of the crystals (Fig. 4.3c). The crystals of columnar calcite are parallel to each other and are wider than 10 microns. The boundary between columnar crystals shows equally-favored crystallographic orientation, more or less normal to former growth surface. At depths of 3.0 and 9.5 cm, the palisade calcite crystals (PC) are straight and parallel to each other (Fig. 4.3d). The parallel interwoven calcite crystals show approximate crystallographic orientations between the crystals (Fig. 4.3d–e). At the depth of 12.0 cm, the crystals of equant calcite (EC) are closely filled and oriented parallel to each other (Fig. 4.3f). Some porous layers observed at 6.2 cm are composed of darker microsparitic calcite (MSC) with a few voids (Fig. 4.3g).

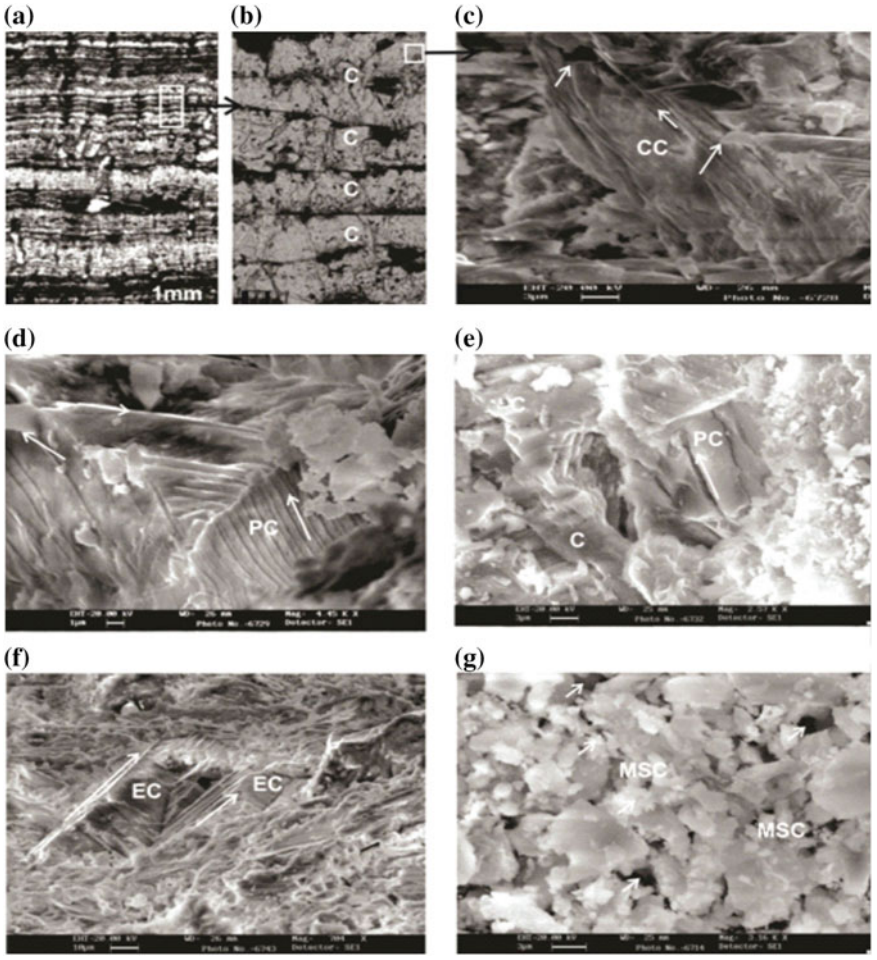

Fig. 4.3 Petrographic images **a**–**b** and SEM images **c**–**g** of KL-3 stalagmite; **a** Polished thin section from upper middle part with compact layers; **b** High resolution image of upper part with flat top layers with calcite; **c** SEM image at depth of 1.5 cm of long columnar calcite; **d** Palisade calcite (PC) at 3.0 cm depth, arrow indicating interwoven calcite; **e** Palisade calcite (PC) crystal boundaries and approximate crystallographic orientation between the crystals inter at 9.5 cm depth; **f** Interwoven trigonal crystals of equant calcite (EC) at 12.0 cm, arrows showing parallel orientation of crystals; **g** Porous layers at 6.2 cm showing presence of microsparitic calcite (MSC), arrows indicate arrangement of MSC crystals with a few voids

On the basis of stalAge results, the growth rate is estimated and it is assumed that the KL-3 grew with a rate of 23–47 μm/year with fluctuations (Fig. 4.4). The growth rate is slow during some multi centennial events (e.g., 14.5–14.0, 12.8–12.5, 10.6–10.4, 9.8–9.6 ka BP). The higher growth rate is observed between 15.4–15.0 and 12.5–11.8 ka BP and is maximum during 10.1–9.8 ka BP. The fluctuations in

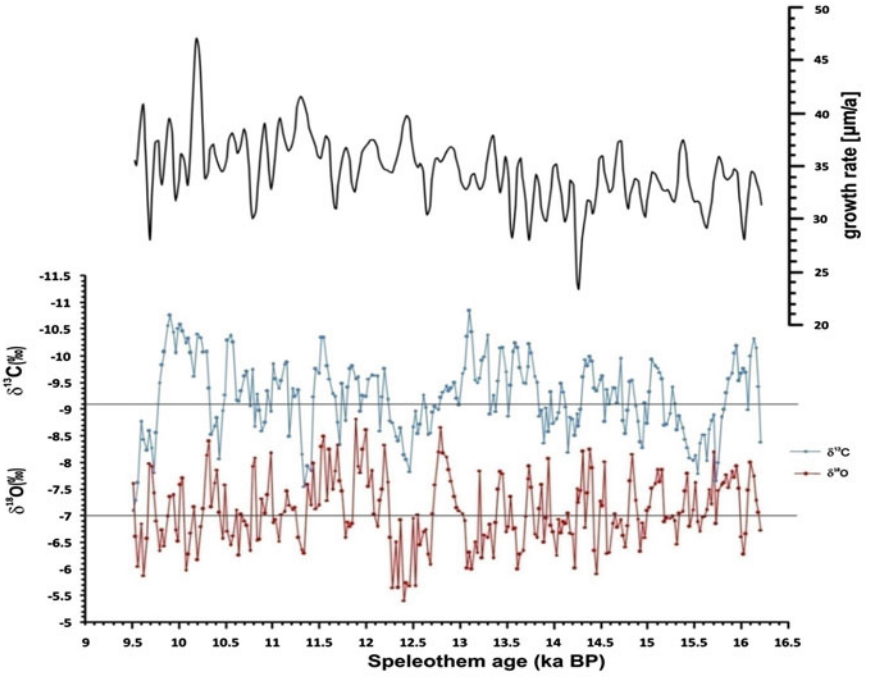

Fig. 4.4 Fluctuations in growth rate and $\delta^{18}O$ and $\delta^{13}C$ values in KL-3 stalagmite. Horizontal reference lines are based on the average values of $\delta^{18}O$ and $\delta^{13}C$

the growth rate suggest that the deposition of KL-3 is not uniform. In addition, the growth rate is not well linked with the isotopic results. The growth rate depends on many parameters as resolution of sub-samples, chronology and continuity of growth rings etc. Therefore, the accurate calibration is not possible on the basis of growth rate.

4.1.4 Isotopic Results

A total no of 245 samples were drilled along the central growth axis of KL-3. The $\delta^{18}O$ values range from −5.41 to −8.82‰ with a variation of 3.5‰ (Fig. 4.4). The $\delta^{13}C$ values range from −7.087 to −10.839‰. The isotopic values show large fluctuations, thus we used average values (−7‰ for $\delta^{18}O$ and −9.2‰ for $\delta^{13}C$) as reference values. The $\delta^{18}O$ value of mean annual precipitation at Kalakot (GNIP http://www.iaea.org/water) is −6.8‰, which is very close to average $\delta^{18}O$ values in the KL-3. Therefore, the $\delta^{18}O$ values higher than the reference line (Fig. 4.4) are considered as representation of cooler/drier climate. Similarly, the lower $\delta^{13}C$ values should broadly show warmer or wetter climate.

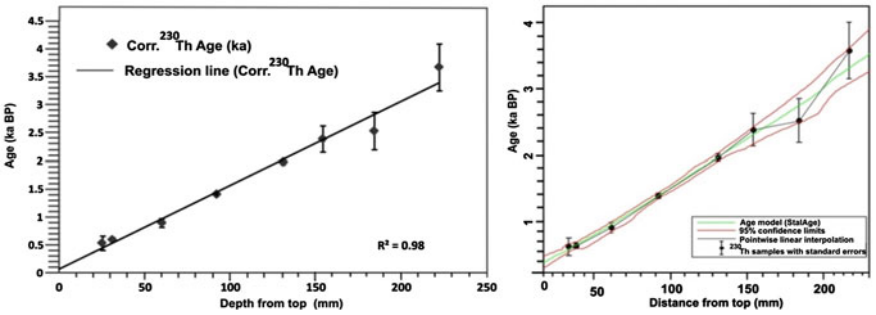

Fig. 4.5 Age/depth model by linear regression and StalAge. The black dots represent the individual age measurements at different depths with corresponding age uncertainties

On the basis of $\delta^{18}O$ isotopes and cluster pattern, five phases can be recognized as, (i) a period from 16.3 to 14.3 ka BP showing fluctuations in $\delta^{18}O$ values indicating a number of excursions of lighter and less heavier values, demonstrating shifts in the precipitation, (ii) the second stage during which, $\delta^{18}O$ and $\delta^{13}C$ values show a declining precipitation pattern from 14.3 to 13.9 ka BP and supporting cold and dry period, (iii) a sharp peak though not prominent between 13.9 and 12.7 ka BP indicating warm and moist conditions, (iv) Subsequently, from 12.7 to 12.5 ka BP, $\delta^{18}O$ values show sudden reduction in precipitation and this period is marked as lowest precipitation and consequently a cold and dry event, (v) a sudden shift of $\delta^{18}O$ and $\delta^{13}C$ values towards the higher precipitation and transition to the wetter conditions.

4.2 Sainji (SA-1) Stalagmite

4.2.1 Age/Depth Model

In SA-1, the Uranium concentration 0.6 μg/g seems ideal for ages with uncertainties smaller than 0.1 ka BP. Ten ages (Table 4.2) were obtained from this sample, but only 8 ages were taken into account as SA-19.6 and SA-25.0 gave large error bars as the high concentration of ^{232}Th seem responsible for an increase in the age uncertainties for SA1-19.6 and SA1-25.0. Based on the Age/depth model, SA-1 covers a time period of 4.0–0.2 ka BP (Fig. 4.5).

Table 4.2 U/Th dates from (SA-1). Ages of samples SA1-19.6 and SA1-25.0 were not used because of high ^{232}Th content

Sample code	Depth from top (cm)	^{234}U (‰)	^{238}U (μg/g)	^{230}Th (pg/g)	^{232}Th (ng/g)	^{230}Th/^{232}Th atomic ratio	^{230}Th/^{232}Th activity ratio	2-sigma	Age_{uncorr} (ka BP)	Age_{corr} (ka BP)
SA1-2.5	2.5	140.4 ± 8.0	0.6304 ± 0.0013	0.097 ± 0.020	7.677 ± 0.100	1.2745E−05	2.36	0.49	0.91	0.54 ± 0.13
SA1-3.1	3.1	149.8 ± 4.9	0.6261 ± 0.0013	0.104 ± 0.006	7.908 ± 0.042	1.3266E−05	2.46	0.14	0.97	0.6 ± 0.04
SA1-6.0	6.0	147.7 ± 5.7	0.5408 ± 0.0011	0.099 ± 0.005	2.545 ± 0.012	3.9238E−05	7.26	0.37	1.07	0.9 ± 0.08
SA1-9.2	9.2	149.4 ± 4.8	0.5948 ± 0.0012	0.163 ± 0.005	3.007 ± 0.011	5.4678E−05	10.12	0.31	1.60	1.41 ± 0.04
SA1-13.1	13.1	142.2 ± 4.4	0.6248 ± 0.0012	0.221 ± 0.005	1.238 ± 0.005	0.0002E−07	33.33	0.77	2.09	1.98 ± 0.05
SA1-15.4	15.4	134.4 ± 9.1	0.6233 ± 0.0012	0.283 ± 0.021	6.347 ± 0.088	4.4976E−05	8.32	0.63	2.71	2.39 ± 0.24
SA1-18.4	18.4	140.0 ± 3.5	0.6621 ± 0.0013	0.349 ± 0.019	14.028 ± 0.130	2.5095E−05	4.65	0.26	3.13	2.53 ± 0.33
SA1-19.6	19.6	151.6 ± 5.9	0.5456 ± 0.0011	0.483 ± 0.026	56.068 ± 0.471	8.6894E−06	1.61	0.09	5.26	2.6 ± 1.39
SA1-22.2	22.2	143.9 ± 3.4	0.7710 ± 0.0015	0.585 ± 0.011	24.099 ± 0.096	2.4486E−05	4.53	0.09	4.52	3.67 ± 0.42
SA1-25.0	25.0	152.5 ± 4.3	0.6841 ± 0.0014	1.090 ± 0.021	128.800 ± 0.618	8.5363E−06	1.58	0.03	9.70	4.84 ± 2.6

4.2.2 Drip Water

Based on the GNIP (Global Network of Isotopes in Precipitation) data (1961–2001), the mean $\delta^{18}O$ values during ISM and WDs at New Delhi (300 km away from Cave site) are −6.8 and −0.8‰ respectively. The recent studies (Garzione et al. 2000) suggested that the $\delta^{18}O$ water can be helpful to examine the source of moisture and establish the palaeoenvironmental conditions (Hren et al. 2009). Pande et al. (2000) measured $\delta^{18}O$ values from the water of Himalayan front and such data are also available from Tibetan Plateau (Quade et al. 2007) and China (Liu et al. 2008) to understand the source of moisture (Garzione et al. 2000). Hren et al. (2009) established a relationship between $\delta^{18}O$ values of water and altitude as ~ 0.3‰ per 100 m. This means that the $\delta^{18}O$ values will be lowered by 0.3‰ at every 100 m altitude. The elevation difference between Sainji (1478 m) and Delhi (215 m) is about 1200 m. Therefore, the $\delta^{18}O$ values of cave site are supposed to be about −3.6‰ lower than Delhi. This means that the −10.4 and −4.4‰ should be more representative $\delta^{18}O$ values of ISM and WDs respectively at the cave location. However the $\delta^{18}O$ values of three drip water samples are −7.4‰ (pre ISM) and −8.2‰ and −8.0‰ (post ISM) and with an average of −7.86‰. This average value is higher than the expected value of −10.4‰. This apparently means that the WDs prevailed significantly during the winter months in this region (Datte et al. 1991; Kotlia et al. 2012). We suggest that the autumn and spring seasons provided only a negligible amount of precipitation.

4.2.3 Mineralogy

In SEM study, the sample shows no evidence of re-crystallization and hiatus. It is mainly composed of aragonite except for upper 1 cm and the section below 20 cm which is calcite (Fig. 4.6). Only one small section at 21–22 cm is composed of gypsum. This result is confirmed by petrographic analysis, XRD and Mg/Ca ratio (Fig. 4.6). The aragonite shows low Mg/Ca concentration than calcite (Huang and Fairchild 2001; Dietzel et al. 2004). The calcite section is darker in colour and whereas aragonite is lighter. Most part of the sample is composed of acicular aragonite (Fig. 4.7a–b) which is composed of needle like thin, markedly elongated and pointed crystal of less than 10 microns. The calcite crystals are elongated and wider than 10 microns (Fig. 4.7c). The boundary between calcite and aragonite is identified by the shape and orientation of crystals (Fig. 4.7d).

4.2.4 Isotopic Results

The $\delta^{18}O$ values of SA-1 show a variation between −2.1 and −8.9‰ (Fig. 4.8). The $\delta^{13}C$ values range from −3.41 to 3.67‰. The $\delta^{18}O$ values show a variation of 6‰.

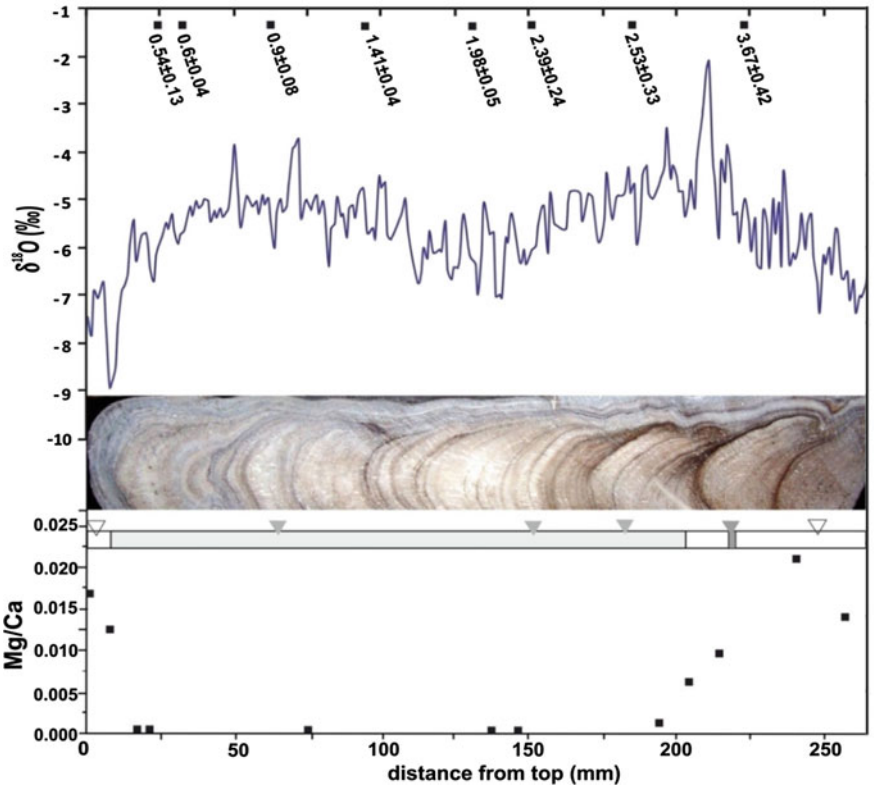

Fig. 4.6 $\delta^{18}O$ isotope composition of SA-1 stalagmite and Mg/Ca ratio. Position of U/Th samples (ages in ka) is shown on the top. The horizontal grey bars indicate aragonite deduced from low Mg/Ca ratio and confirmed by XRD (grey triangles). Intervening sections are calcite as shown by higher Mg/Ca ratio and verified by XRD (open triangles). One thin layer is composed of gypsum (dark grey rectangle)

Generally, the values of $\delta^{18}O$ and $\delta^{13}C$ do not co vary with each other, which reflect that the kinetic fractionation has not affected the deposition of sample.

The oxygen equilibrium isotope fractionation at mean annual temperature between water and $CaCO_3$ is 30.04‰ for calcite and 30.8‰ for aragonite (Kim and O'Neil 1997). Thus the sections of calcite and aragonite show a difference of 0.8‰ in the fraction values. Therefore, we corrected the calcite section values by adding 0.8‰. The results of $\delta^{18}O$ (Fig. 4.8) demonstrate mainly four sectors: (i) a period of 4–3 ka BP reflecting the reduction in precipitation and with 3.2 ka BP is marked as the lowest precipitation, (ii) period between 3 and 2 ka BP, marked as increase in precipitation with a 2.1 ka BP as higher precipitation, (iii) 2.0–0.8 ka BP period reflecting two dry periods at 1 and 0.8 ka BP, (iv) the last stage indicating increasing trend in precipitation with 0.25 ka BP (1700 AD) as the highest precipitation.

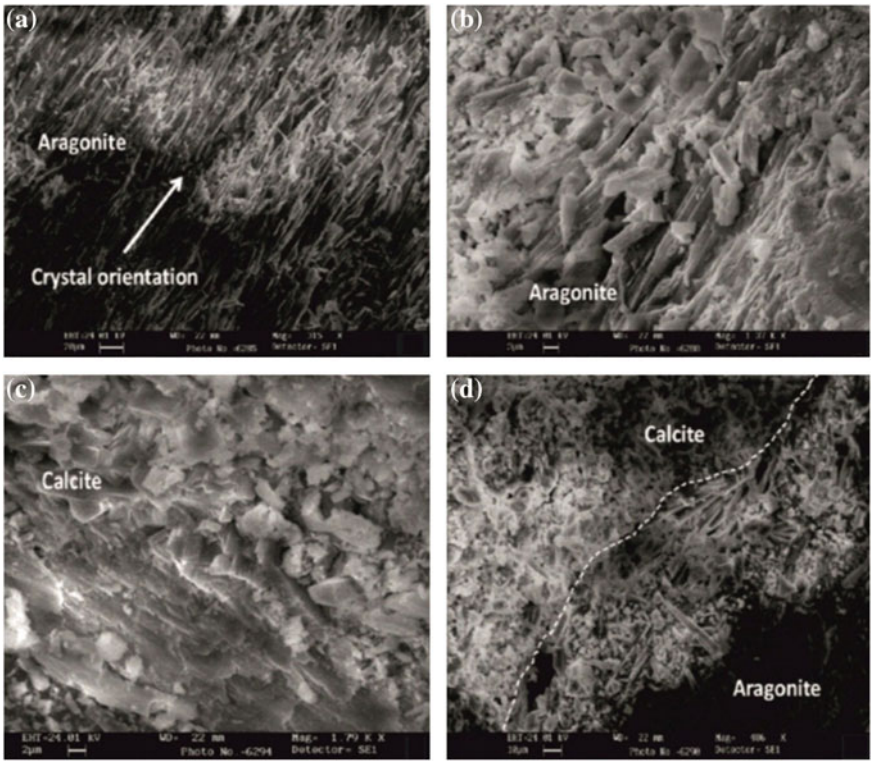

Fig. 4.7 SEM analysis of SA-1 stalagmite; **a** Middle part with elongated aragonite rays, arrow indicating direction of crystal growth; **b** Lower middle part of sample showing botryoids of aragonite; **c** Basal part of stalagmite showing growth of columnar calcite; **d** Boundary of aragonite and calcite regions

4.3 Chulerasim (CH-1) Stalagmite

4.3.1 Age/Depth Model

We obtained six dates from CH-1, almost at every second cm (Table 4.3). The error ranges between 0.015 and 0.06 ka BP. The upper portion of the stalagmite could not be dated because of high ^{232}Th content. Both the linear interpolation and StalAge model reflect the similar pattern, although the sample is young and the age model has limitations. Considering the age model, the duration of stalagmite deposition is determined as between 1622 and 1950 AD (Fig. 4.9).

Table 4.3 U/Th dates from Chulerasim sample (CH-1). TUL-10 was not datable because of high ^{232}Th content

Sample code	Depth from top (cm)	U (ppm)	±2 σ	^{232}Th (ppb)	±2 σ	(^{230}Th/^{232}Th)	±2σ	(^{230}Th/^{238}U)	±2 σ	(^{234}U/^{238}U)	±2 σ	Age_{uncor} (ka BP)	±2 σ	Age_{corr} (ka BP)	±2 σ	Corr. initial (^{234}U/^{238}U)	±2 σ
TUL-10	1.0	2.0884	0.0019	78.91	0.139	0.44	0.01	0.0055	0.0001	1.2139	0.0031	–	–	–	–	–	–
TUL-21	2.1	1.9517	0.0029	9.308	0.036	1.54	0.10	0.00243	0.00016	1.2214	0.0036	0.217	0.014	0.101	0.060	1.2217	0.0036
TUL-36	3.6	2.1838	0.0012	3.29	0.005	4.26	0.07	0.0021	0.0000	1.2215	0.0016	0.189	0.003	0.153	0.019	1.2217	0.0016
TUL-52	5.2	2.0660	0.0009	7.97	0.027	2.48	0.03	0.0032	0.0000	1.2190	0.0014	0.283	0.003	0.189	0.047	1.2193	0.0015
TUL-68	6.8	0.2803	0.0003	0.286	0.001	8.69	0.27	0.00293	0.00010	1.2097	0.0022	0.265	0.009	0.240	0.015	1.2099	0.0022
TUL-85	8.5	2.3190	0.0013	3.71	0.006	6.57	0.06	0.0035	0.0000	1.2204	0.0013	0.310	0.003	0.271	0.020	1.2206	0.0013
TUL-99	9.9	3.1119	0.0033	5.417	0.019	7.94	0.16	0.00455	0.00008	1.2239	0.0017	0.407	0.007	0.365	0.022	1.2242	0.0017

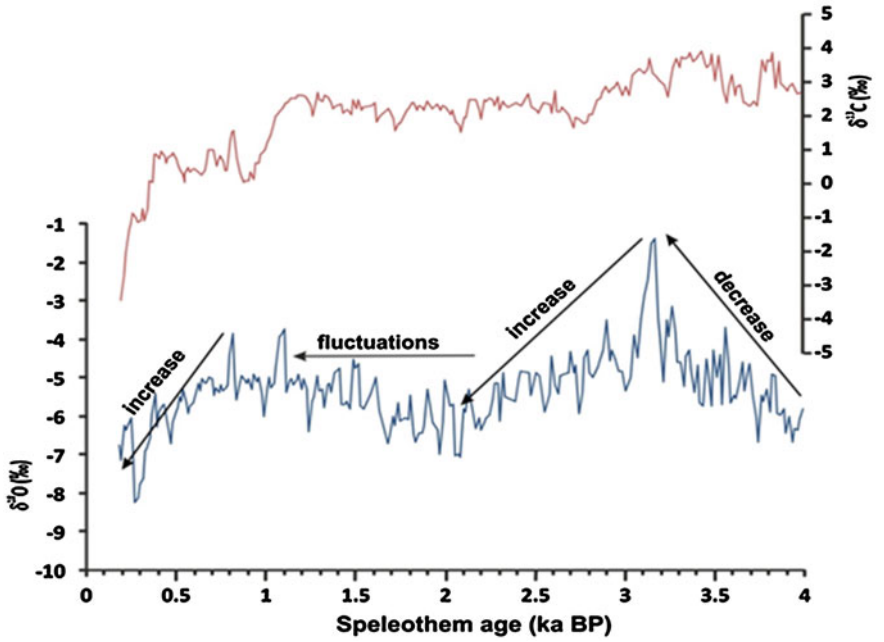

Fig. 4.8 $\delta^{18}O$ and $\delta^{13}C$ values along the growth axis

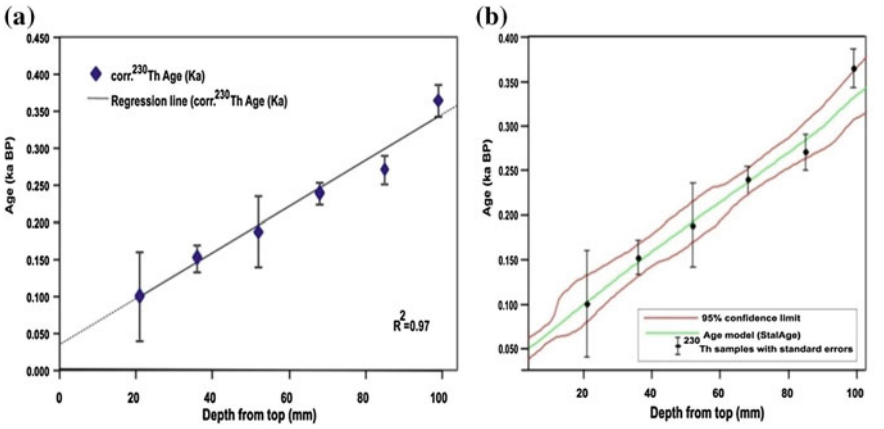

Fig. 4.9 **a** Regression line through the origin with error bars; **b** Age/depth relationships with StalAge

4.3.2 Hendy Test Results

The $\delta^{18}O$ and $\delta^{13}C$ variations along one growth layer are −4.9 to −5.6‰ and −4.5 to −7.4‰ respectively (Fig. 4.10). The results show that the sample was not deposited

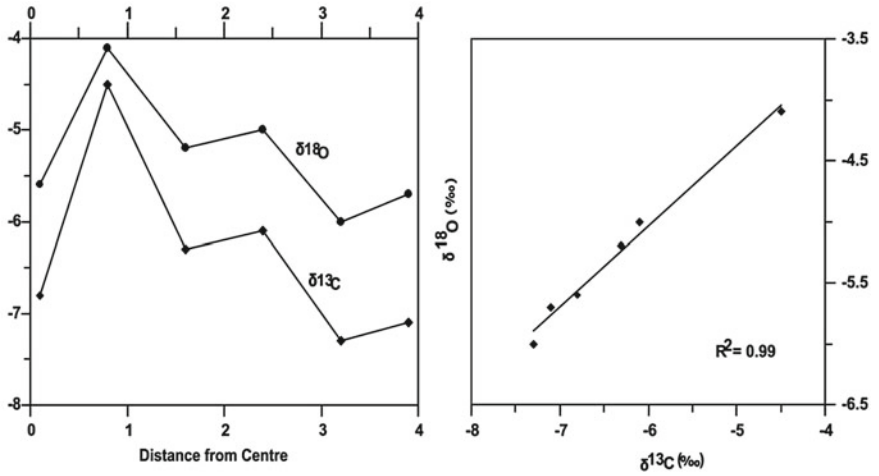

Fig. 4.10 Hendy test result on one layer (4.1 cm from top) of stalagmite

under isotopic equilibrium. However, the consistency of this test has been a centre of argument in the last decade (Fleitmann et al. 2004; Dorale and Liu 2009; Kotlia et al. 2012). The $\delta^{18}O$ and $\delta^{13}C$ values are signal of changes in both precipitation and soil productivity (Dorale and Liu 2009). Therefore, even if the Hendy test is not passed, $\delta^{18}O$ values may still be considered as reliable indicator of precipitation (Fleitmann et al. 2004; Zhou et al. 2011; Kotlia et al. 2012) particularly in sub-tropical locations.

4.3.3 Mineralogy and Growth Rate

The SEM analysis suggests that the stalagmite is composed of purely aragonite (Fig. 4.11). The polished surface sample reflects well developed prominent growth rings without any discontinuity or hiatus.

The sample has alternate bands of compact and porous layers. The large part of the sample is composed of elongated and columnar aragonite with a general longitudinal orientation, whereas the remaining part is made up of needle shaped and somewhat fibrous aragonite. The compact layers have elongated thick and long packages of aragonite needles while the porous layers have fewer amounts of aragonite crystals (Fig. 4.11a–d). The aragonite crystals are 0.5 mm long and are characterized by flat faces on the flank. There are no signs of recrystallization of aragonite to calcite. The needle shaped aragonite is the indicator of continuous and slow degassing which is rich in $\delta^{18}O$ and $\delta^{13}C$ values than the common aragonite crystals (Frisia et al. 2002). The growth rate varies from 300 to 382 μm/year. It is minimum between 1660 and 1710 AD and maximum from 1750 to 1820 AD.

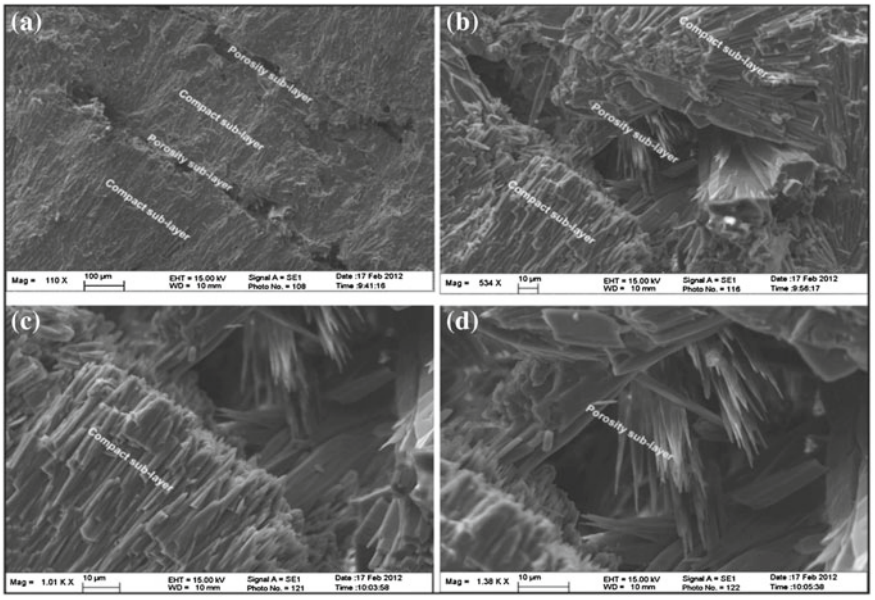

Fig. 4.11 **a–d** SEM images of CH-1. *Note* the compact and porous sub layers of aragonite

4.3.4 Laminae Counting

While counting the laminae by magnifying the specimen under U-V light for 400 times, the first and third sectors have less laminae than the number of years. But the fourth and fifth segments have more laminae than the dating intervals (Fig. 4.12). Counting of laminae and age difference is matched only for second sector where 30 laminaes are present in 31 years. The difference in layers and ages may be due to the age uncertainties.

4.3.5 Isotopic Results

The $\delta^{18}O$ and $\delta^{13}C$ values are range from $-2.71‰$ to $-5.92‰$ and $-5.72‰$ to $-8.83‰$ respectively. Based on the isotopic cluster pattern, the data set can be divided into four phases (Fig. 4.13). The first phase reflects the increase in precipitation from 1622 AD onwards with dry event at the origin (ca. 1622 AD) and ending with a wetter event at 1665 AD (variation from -2.5 to $-5.2‰$). During the next phase from 1665 to 1820 AD, the $\delta^{18}O$ values demonstrate higher precipitation with decadal scale dry event at 1740–1750 AD and two major wetter events at ca. 1795 and 1810 AD. Subsequently a sudden drier phase occurs between 1820 and 1870 AD with a prominent dry event at 1820–1825 AD which is followed by wetter event around

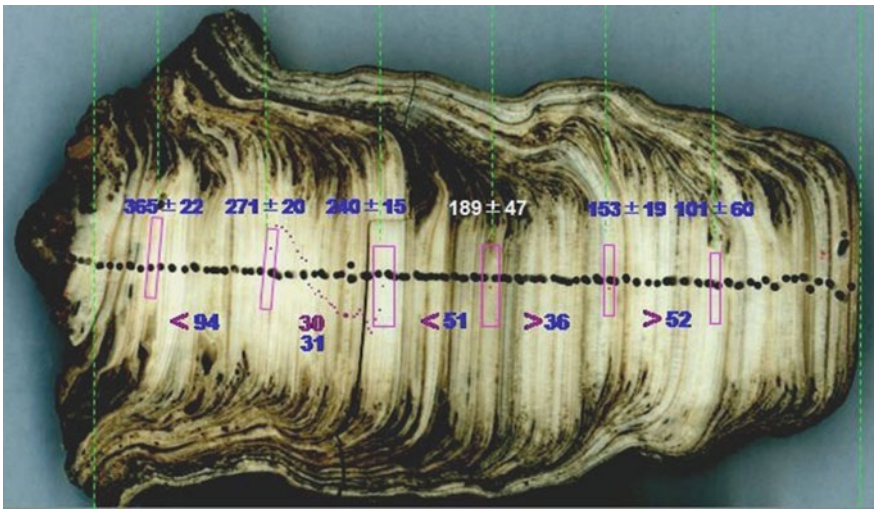

Fig. 4.12 Laminae counting in different sectors of CH-1

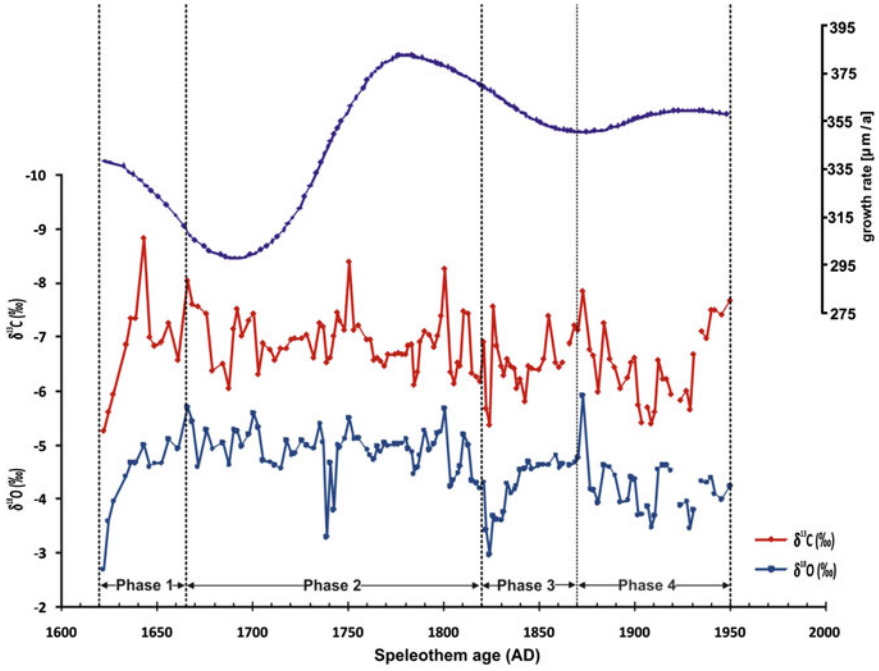

Fig. 4.13 $\delta^{18}O$ and $\delta^{13}C$ values and growth rate in CH-1 from 1622 to 1950 AD

1870 AD. During the last phase, the $\delta^{18}O$ values reflect reduction in precipitation until 1950 AD.

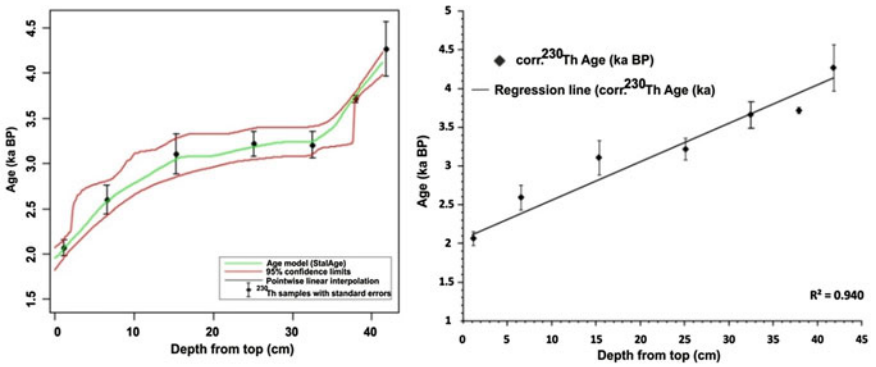

Fig. 4.14 Age/depth model and StalAge. Black dots represent the individual age measurements at different depths with corresponding age uncertainties

4.4 Dharamjali (DH-1) Stalagmite

4.4.1 Age/Depth Model

Seven dates from a 41 cm long stalagmite (DH-1) were obtained as 1.86, 2.60, 3.11, 3.22, 3.21, 3.72 and 4.27 ka BP (Fig. 4.14). The U concentration varies between 1.3 and 4.5 μg/g. Correction for detrital contamination assumes a $^{232}Th/^{238}U$ concentration ratio of 3.8 ± 1.9 and ^{230}Th, ^{234}U and ^{238}U in secular equilibrium. The individual age uncertainties are between 0.1 and 0.3 ka BP (Table 4.4).

However, it also shows significant ^{232}Th concentrations, leading to an increase of the final age uncertainties. The deposition of sample began at 4.05 ka BP and seized at 1.96 ka BP.

4.4.2 Mineralogy and Growth Rate

The DH-1 consists mainly of aragonite except at two sectors (0–7.3 cm and 8.5–13.5 cm) which are calcite (Fig. 4.15). Deposition of aragonite may be directly related to the higher $\delta^{18}O$ values under reduced precipitation, hence show drier conditions. Alternatively, the periods of calcite deposition are associated with lighter $\delta^{18}O$ values during more precipitation and indicate a more humid climate under reduced evaporation. On the basis of stalAge model, the growth rate in the sample was measured as 76–340 μm/year. The higher growth rate (above 250 μm/year) between ca. 3.3–3.1 ka BP may be ascribed to comparatively stronger intensity of the precipitation, as is also reflected in the isotopic measurements (Fig. 4.16).

At cave temperature, the difference in oxygen equilibrium isotope fractionation between water and $CaCO_3$ is 30.04‰ for calcite (Kim and O'Neil 1997) and 30.8‰ for aragonite (Kim et al. 2007). Hence, the calcite sections should show $\delta^{18}O$ values

Table 4.4 U/Th dates form Dharamjali stalagmite (DH-1)

Sample code	Depth from top (cm)	^{234}U (‰)	Error	^{238}U (μg/g)	Error	^{230}Th (pg/g)	Error	^{232}Th (ng/g)	Error (ka BP)	Age_{uncorr} (ka BP)	Age_{corr} (ka BP)
DH1-1.1	1.1	650.5	4.1	1.2987	0.0019	0.692	0.025	7.56	0.18	1.92	1.86
DH1-6.5	6.5	627.9	4.2	2.7705	0.0028	1.76	0.11	3.55	0.38	2.62	2.60
DH1-15.3	15.3	624.3	5.6	2.6100	0.0065	1.97	0.14	5.67	0.57	3.15	3.11
DH1-25.1	25.1	620.3	3.4	3.8718	0.0058	3.00	0.13	1.55	0.15	3.23	3.22
DH1-32.5	25.1	621.7	2.3	3.9099	0.0039	3.01	0.14	0.3540	0.0064	3.21	3.21
DH1-37.9	37.9	638.9	2.6	4.5512	0.0046	4.106	0.049	1.924	0.011	3.728	3.721
DH1-41.8	41.8	622.4	2.4	4.5339	0.0045	4.65	0.33	4.37	0.10	4.29	4.27

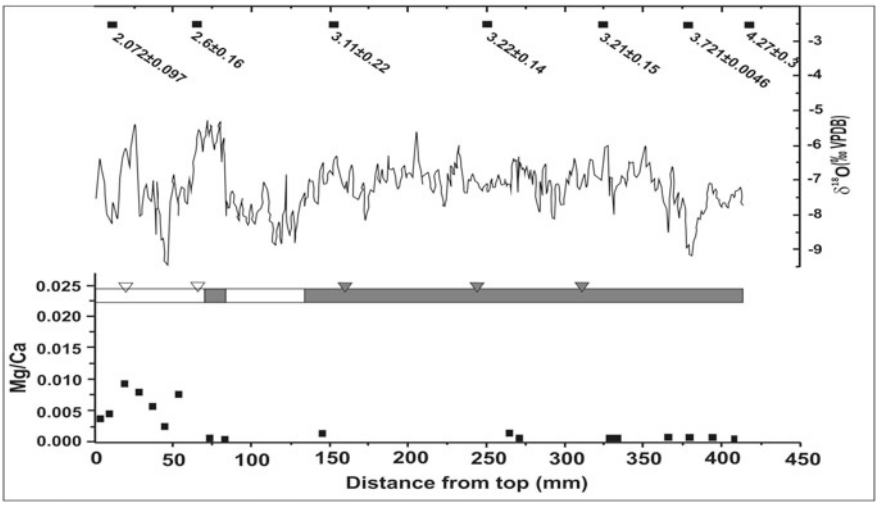

Fig. 4.15 Mineralogy, Mg/Ca ratio and $\delta^{18}O$ of DH-1. Squares near the top show the position of U/Th samples (ages in ka BP). Horizontal grey bars indicate aragonitic sections deduced from low Mg/Ca ratios and confirmed by spot analyses by XRD (gray triangles). Intervening sections are calcitic as shown also by higher Mg/Ca ratios (open triangles)

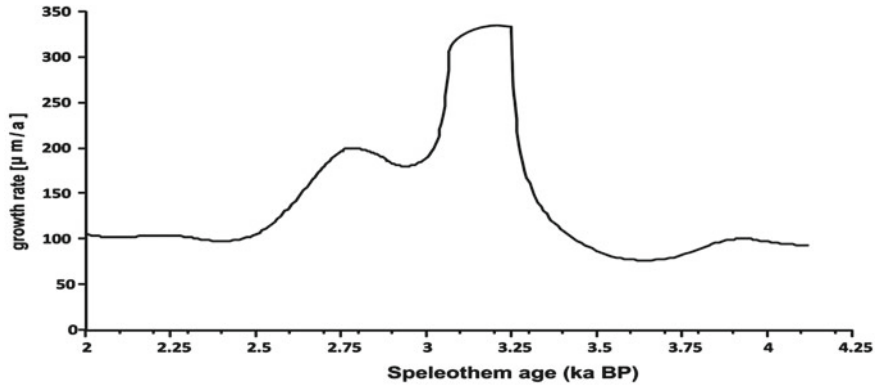

Fig. 4.16 The growth rate in DH-1 obtained by StalAge

that are by about 0.8‰ lower than the aragonite sections due to the differences in fractionation. We therefore corrected the $\delta^{18}O$ data of the calcite sections, accordingly.

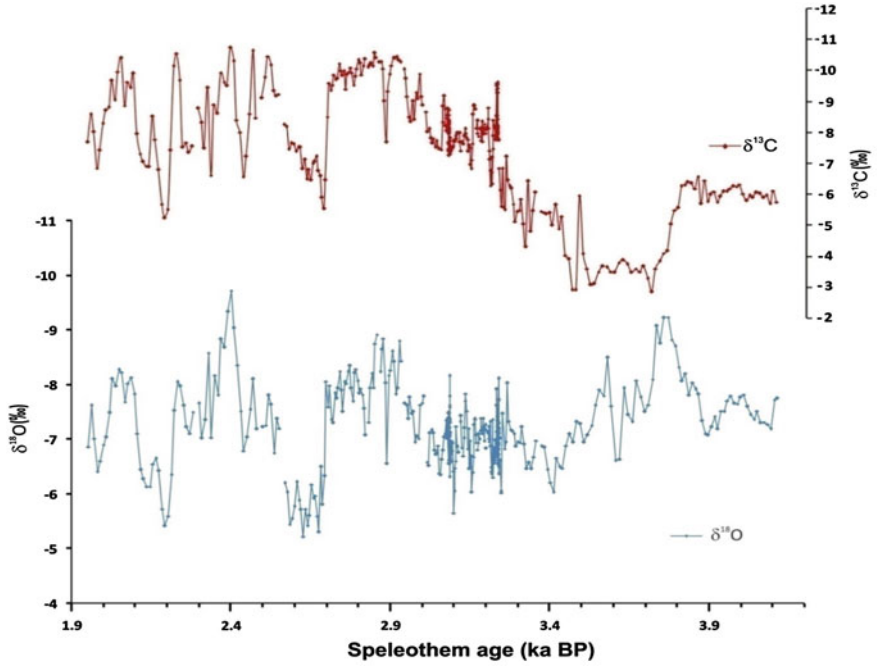

Fig. 4.17 $\delta^{18}O$ and $\delta^{13}C$ values along the central growth axis and their cluster pattern

4.4.3 Isotopic Results

The $\delta^{18}O$ values are between −5.3 and −10‰ and $\delta^{13}C$ values range from −3.0 to −10.5‰ (Fig. 4.17). From 4.05 to 3.75 ka BP, the $\delta^{18}O$ values (between −7 and −9‰), depict considerably higher precipitation that reached to the maximum of about −10‰ at 3.7 ka BP, thus making this decadal event the wettest one. The precipitation reduced steadily from 3.7 ka BP onwards and reached to the minimum most ($\delta^{18}O$ values about −6‰) at 3.5 ka BP one of the most arid events.

Between 3.5 and 2.5 ka BP, DH-1 grew continuously where conditions remained in a more humid mean state until around 2.7 ka BP although there appear some fluctuations. A sudden jump is observed towards heavier $\delta^{18}O$ values between 2.7 and 2.6 ka BP (around −5‰) indicates less precipitation (most arid event). However, from 2.6 ka onwards, an abrupt drop occurs in $\delta^{18}O$ and reaches to a peak at 2.4 ka BP, viewing the second highest precipitation event. Subsequently, $\delta^{18}O$ values show a dry event from 2.2 to 2.1 ka BP and a wet between 2.2 and 2 ka BP.

4.5 Tityana (TCS) Stalagmite

4.5.1 Age/Depth Model

The ^{230}Th/U method proved unsuccessful in TCS sample due to multiple sources of non-authigenic ^{232}Th and low uranium concentration (<10 ppb). In the speleothems, the uncertainty of ^{230}Th/^{232}Th activity affects the accuracy of the ^{230}Th/U age, especially when the activity of ^{232}Th is high for the sample. In TCS sample, the ^{230}Th/U dates have larger uncertainties (Table 4.5), this is not suitable for further calibration.

Therefore, we used AMS ^{14}C dating to construct the chronology of the stalagmite. Five samples were chosen for AMS radiocarbon dating (Table 4.6). All dates were calibrated using online Cal Pal program to change the conventional radiocarbon dates into calendar ages (Table 4.6). The Age/depth model was constructed by linear interpolation between the calibrated ages (Fig. 4.18b). The model reveals that the average growth rate is about 0.12 mm/year from 5.7 to 5.15 ka BP. It is comparatively less in middle Sect. (0.02 mm/year) until about 3.76 ka BP and is slightly higher from 3.76 to 3.17 ka BP (Fig. 4.18c). This model permits for non-uniform deposition rates. The model was set with critical values at 95% confidence level and we used median dates for further extrapolation.

4.5.2 Hendy Test Results

In TCS, a small fluctuation of δ^{18}O and δ^{13}C along layer 1 may be due to a little shift in layer while drilling and both values are constant along layer 2 (Fig. 4.19). Similarly, the low correlation coefficient (R^2) values of 0.042 for layer 1 and 0.698 for layer 2 suggest that the degassing of CO_2 was sufficiently slow to maintain the isotopic equilibrium during carbonate precipitation. The test is a check through the correlation between all the values of δ^{18}O and δ^{13}C (Fig. 4.19). The low R^2 value (0.19) further suggests that the kinetic fractionation was negligible and thus the δ^{18}O can be used for climate signals (Fig. 4.19).

4.5.3 Mineralogy

The SEM images indicate that the stalagmite is mainly composed of compact calcite layers (Fig. 4.20a). The crystallization structure is sometime between palisade calcite and columnar calcite. The primary columnar calcite (CC) is elongated with crystallographic axis parallel to the earlier growth surface (Fig. 4.20b–d) and may have been formed either by direct precipitation or as a recrystallization product of precursor aragonite (e.g., Perrin et al. 2014). The palisade calcite (PC) shows growth direction parallel to the crystals boundaries (Fig. 4.21e–f). The large and well

Table 4.5 U/Th ages for the Tityana cave stalagmite (TCS)

Sample code	Depth from top (cm)	^{238}U ppb		^{232}Th ppt	d^{234}U measured	[^{230}Th/^{238}U] activity	[^{230}Th/^{232}Th] ppm	Age uncorrected	Age corrected	d^{234}U$_{initial}$ corrected
TT 1	0.1	97.00	±0.10	9491 ± 795	39.5 ± 2.0	0.23 ± 0.022	3.89 ± 0.38	27,37 ± 302	−846 ± 16432	39.4 ± 2.6
TT 2	4.8	136.9	±0.42	1343 ± 1607	27.2 ± 9.5	0.22 ± 0.0174	3.72 ± 0.30	26,39 ± 237	−2,312 ± 16,671	27.0 ± 9.5
TT 3	5.1	84.54	±0.20	4590 ± 262	24.8 ± 3.2	0.26 ± 0.0100	7.91 ± 0.31	31,96 ± 142	16,987 ± 8142	26.0 ± 3.4
TT 4	12.7	171.0	±0.24	4651 ± 272	22.2 ± 1.8	0.14 ± 0.0041	8.67 ± 0.25	16,42 ± 507	9149 ± 3792	22.8 ± 1.8

All ages were not used because of high error percentage

Table 4.6 AMS dates of Tityana cave stalagmite (TCS)

Sample code	Depth from top (cm)	Lab. No.	Age 14C (ka BP)	Range	Modelled 95% range start (ka BP)	Modelled 95% range end (ka BP)	Modelled median (ka BP)
TCA_1	0.1	Poz-66853	2.985	±30 BP	1.691	1.531	1.584
TCA_2	3.1	Poz-66854	3.475	±35 BP	2.309	2.066	2.229
TCA_3	6.4	Poz-66855	4.470	±35 BP	3.450	3.270	3.387
TCA_4	9.4	Poz-66856	4.640	±35 BP	3.679	3.483	3.583
TCA_5	12.8	Poz-66857	4.940	± 40 BP	4.076	3.844	3.938

We used the median ages

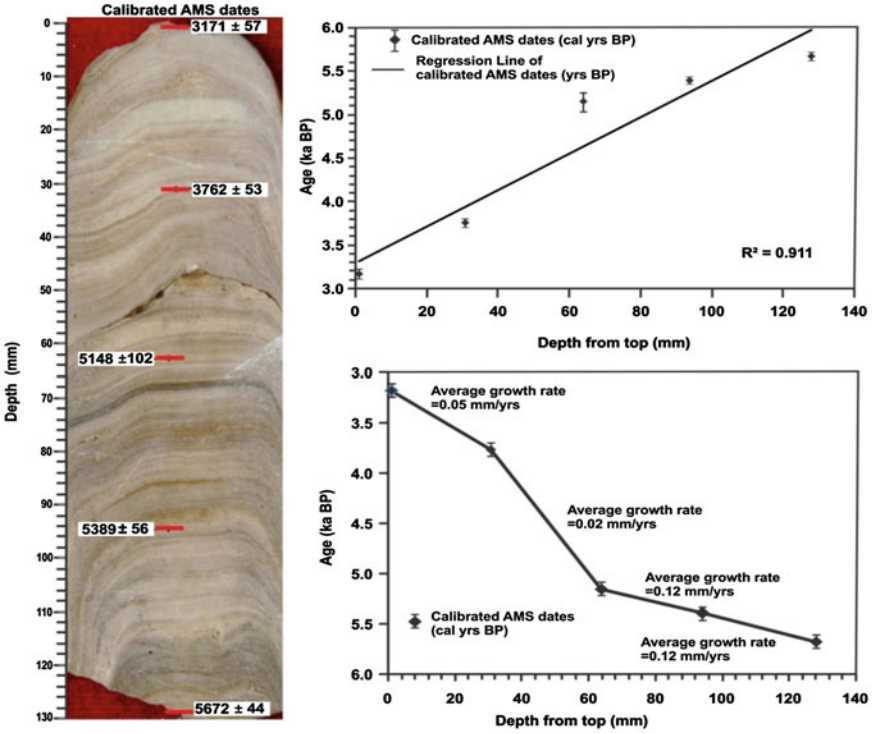

Fig. 4.18 Polished sample of TCS with AMS dating points **a** linear extrapolation of AMS dates; **b** Variation in growth rate through time

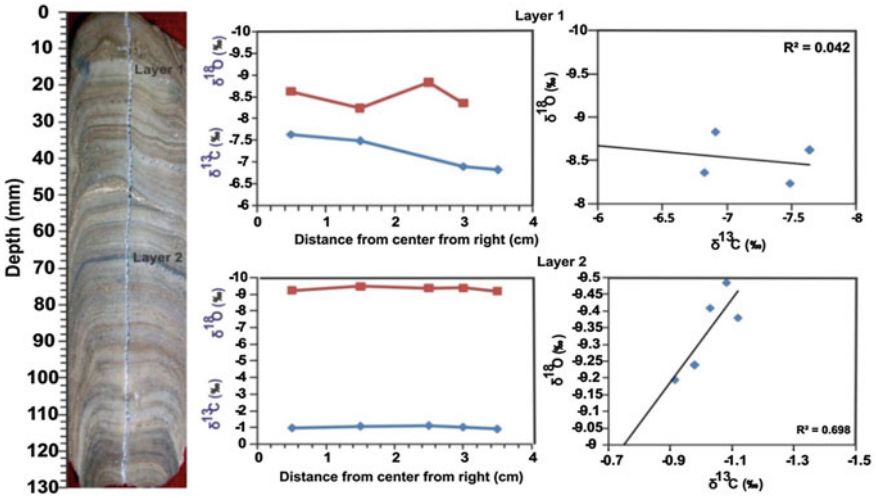

Fig. 4.19 Hendy test on two layers from TCS

developed crystals of equant calcite (EC) with multiple growth of small palisade are also observed (Fig. 4.20f) and they are closely packed with orientation parallel to each other (Fig. 4.21g).

Two thin porous EC layers are observed along the central growth axis (Fig. 4.20h) and the boundary between the CC and EC layers is clearly visible with small cavities (Fig. 4.20i). The powder XRD technique and EDS also reveal that the stalagmite is made up of calcite (Fig. 4.21a–b). Generally, pure calcite stalagmite shows more negative $\delta^{18}O$ (Frisia et al. 2002) indicating high monsoonal intensity.

4.5.4 Isotopic Results

The $\delta^{18}O$ values range from −8.04 to −10.49‰ showing variation of 2.45‰ (Fig. 4.22). The $\delta^{13}C$ values range from −0.3 to −10.77‰. On the basis of $\delta^{18}O$ values, three phases can be identified, (i) a period from 3.9 ka BP to 3.37 ka BP during which $\delta^{18}O$ values show declining pattern in precipitation and 3.4 ka BP is marked as the lowest precipitation period, (ii) An improved precipitation stage between 3.37 and 2 ka BP with two arid pulses, (iii) $\delta^{18}O$ values showing a enhanced precipitation around 2.2–2 ka BP. Subsequently, two prominent dry periods at 1.9–1.6 ka BP.

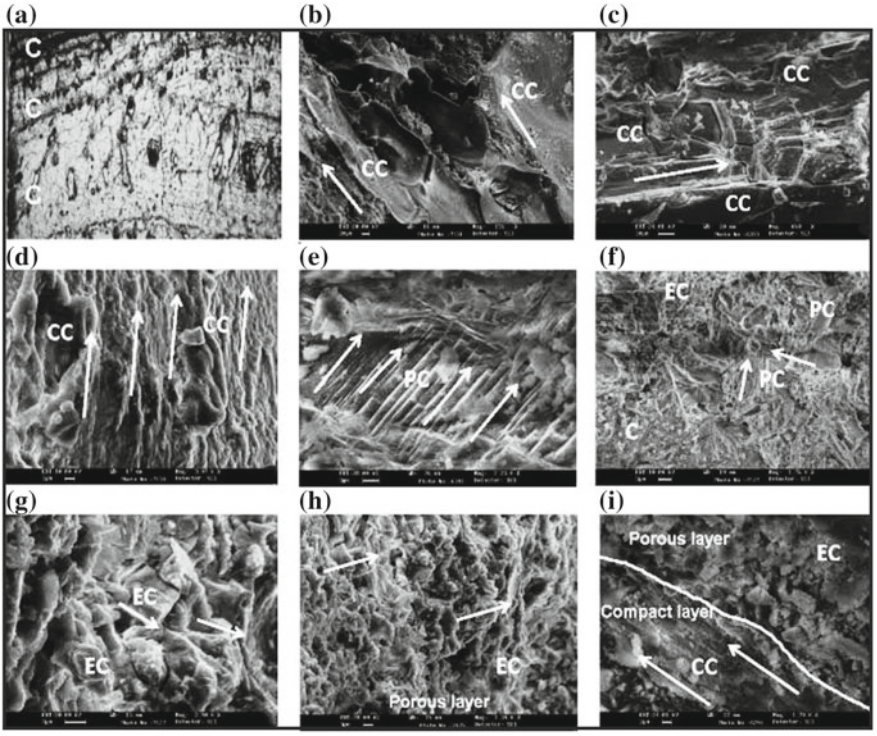

Fig. 4.20 SEM images showing **a** Large elongated compact calcite crystals; **b** Elongated columnar crystals of calcite with their orientation; **c** Orientation of large columnar calcite crystals; **d** Parallel columnar calcite (CC) crystals with growth direction; **e** Straight parallel crystals of palisade calcite (PC); **f** Multiple growth of small palisade and equant calcite crystals; **g** Closely packed and well developed large equant calcite crystals showing inside growth with small cavity on stalagmite surface; **h** Growth of small crystals of equant calcite in porous layers; **i** Columnar and equant calcite along with the boundary between compact and porous layers

4.6 Borar (BR-1) Stalagmite

4.6.1 Age/Depth Model

We obtained three U/Th dates, e.g., 1.18, 8.2 and 10.7 ka BP (Fig. 4.23). The sample covers a time span of 0.16–13.36 ka BP. However, the uranium concentration is as low as 0.01 ug/g (Table 4.7) and error percentage is around 50%. Thus, practically it is not possible to apply the chronology for isotopic interpretation.

Table 4.7 U/Th ages from the Borar cave stalagmite (BR-1)

Sample code	Depth from top (cm)	U (ppm)	±2 s	^{232}Th (ppb)	±2 s	(^{230}Th/^{232}Th)	±2 s	(^{230}Th/^{238}U)	±2 s	(^{234}U/^{238}U)	±2 s	Uncorr. Age (ka)	±2 s	Age$_{corr}$ (ka BP)	±2 s	Corr. initial (^{234}U/^{238}U)	±2 s
BR-vill-1_019	1.9	0.7051	0.0005	23.7	0.0	1.613	0.016	0.0178	0.0002	1.0507	0.0012	1.870	0.019	1.18	0.35	1.0512	0.0012
BR-vill-1_145	14.5	0.1116	0.0001	36.9	0.3	1.258	0.015	0.1372	0.0012	1.0509	0.0009	15.256	0.147	8.2	3.6	1.0557	0.0023
BR-vill-1_191	19.1	0.0752	0.0000	54.1	0.6	0.955	0.013	0.2265	0.0017	1.0427	0.0009	26.697	0.222	10.7	8.6	1.0513	0.0046

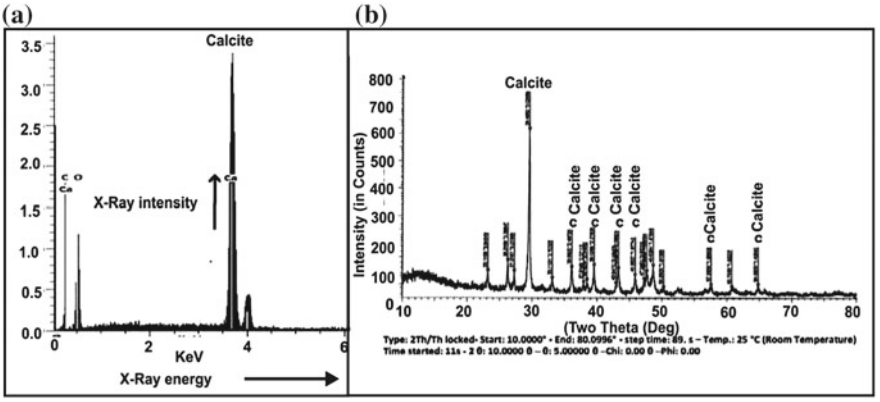

Fig. 4.21 **a** Representative graphs of Energy Dispersive X-ray Analysis (EDS) at different depths; **b** X-ray Diffraction Analysis (XRD) of stalagmite at various depths indicating calcite peaks

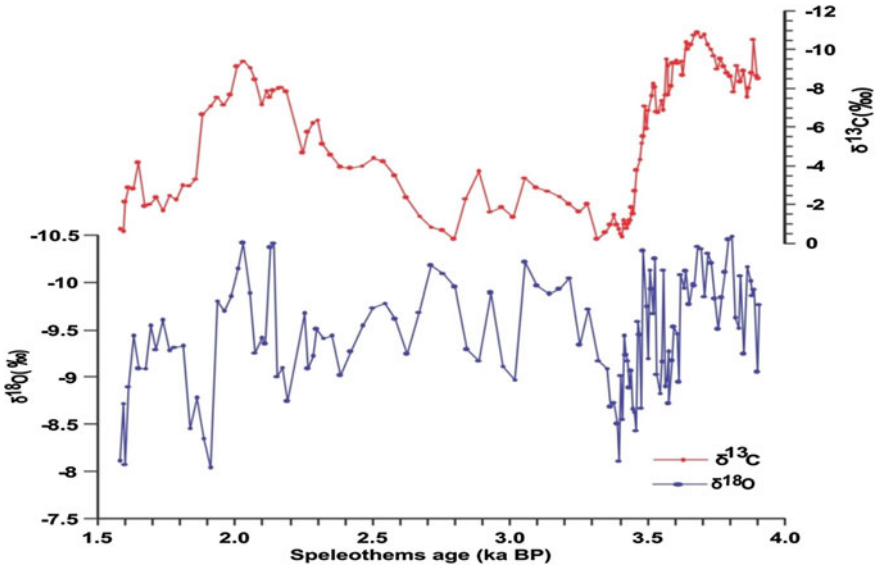

Fig. 4.22 Isotopic variations in TCS along the central growth axis

4.6.2 Hendy Test Results

The hendy test was performed on four layers at different depths, i.e., 10.1, 12.2, 12.5 and 19 cm from top. The $\delta^{18}O$ and $\delta^{13}C$ variations along these layers range from −9.1 to −11‰ and −11.5 to 7.5‰ (Fig. 4.24). The value of the correlation coefficient (R^2) is less than 1 and there is no enrichment of $\delta^{18}O$ towards the outer end for all

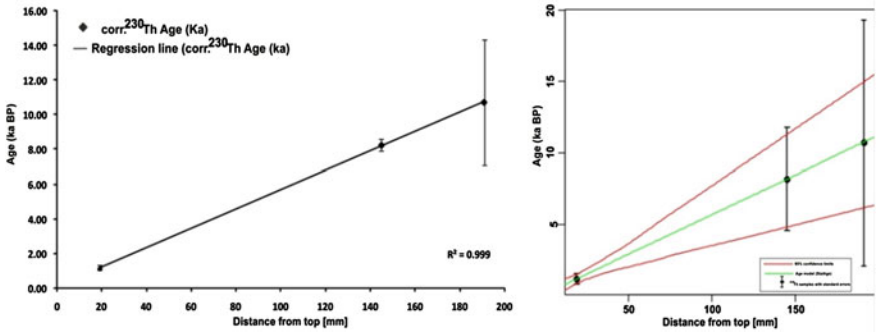

Fig. 4.23 **a** Corrected ^{230}Th dates from the BR-1 and regression through the origin; **b** Age-depth relationship by StalAge (note the large errors)

the layers. Thus, the sample may be considered as free from kinetic fractionation. The hendy test results show that the sample was deposited in isotopic equilibrium.

4.6.3 Isotopic Results

The δ^{18}O and δ^{13}C ranges from −7.4 to −11.17‰ and −1.04 to −12.18‰ respectively (Fig. 4.25). The δ^{18}O values show a zig-zag pattern without any zonation. The δ^{13}C values shoe even higher fluctuations. Thus it is difficult to divide this data into different climatic zones.

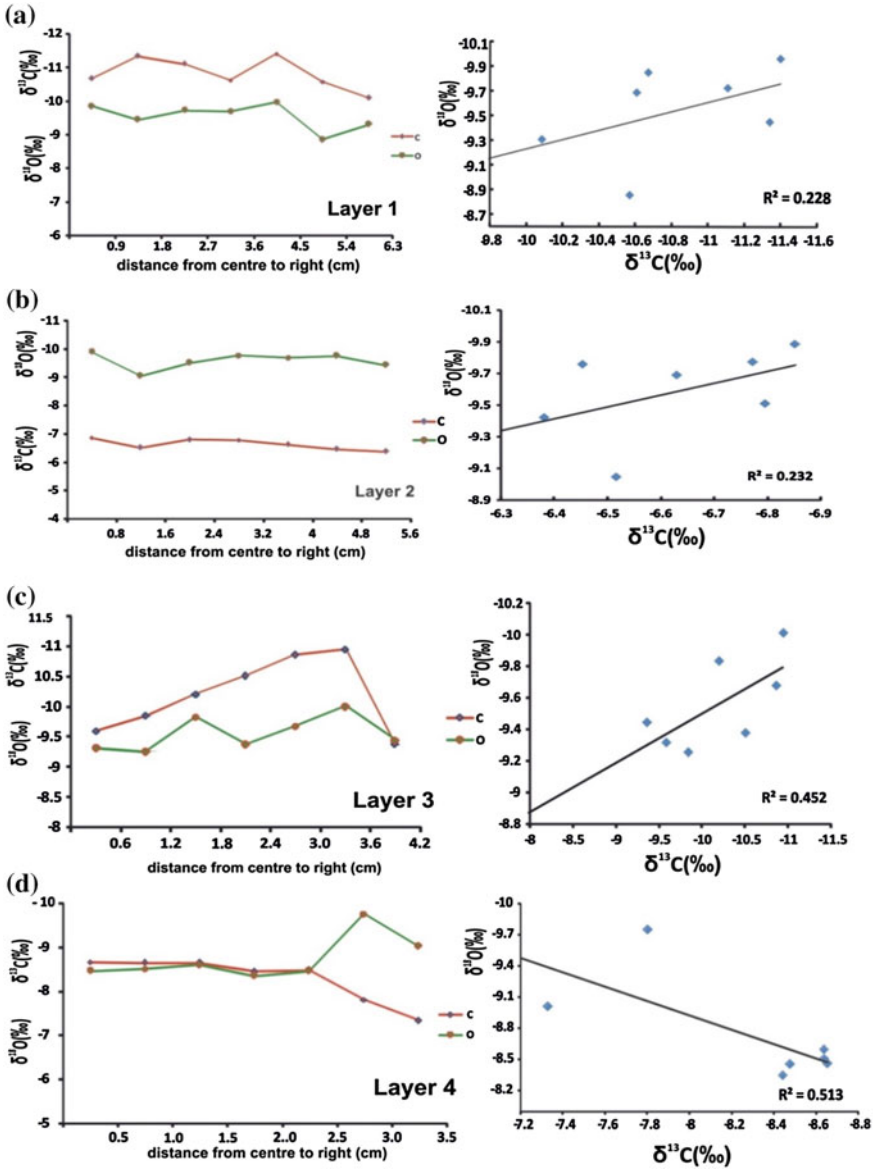

Fig. 4.24 Hendy test results: $\delta^{18}O$ and $\delta^{13}C$ values along three growth layers at 10.1, 12.2, 12.5 and 19 cm from the top of the sample

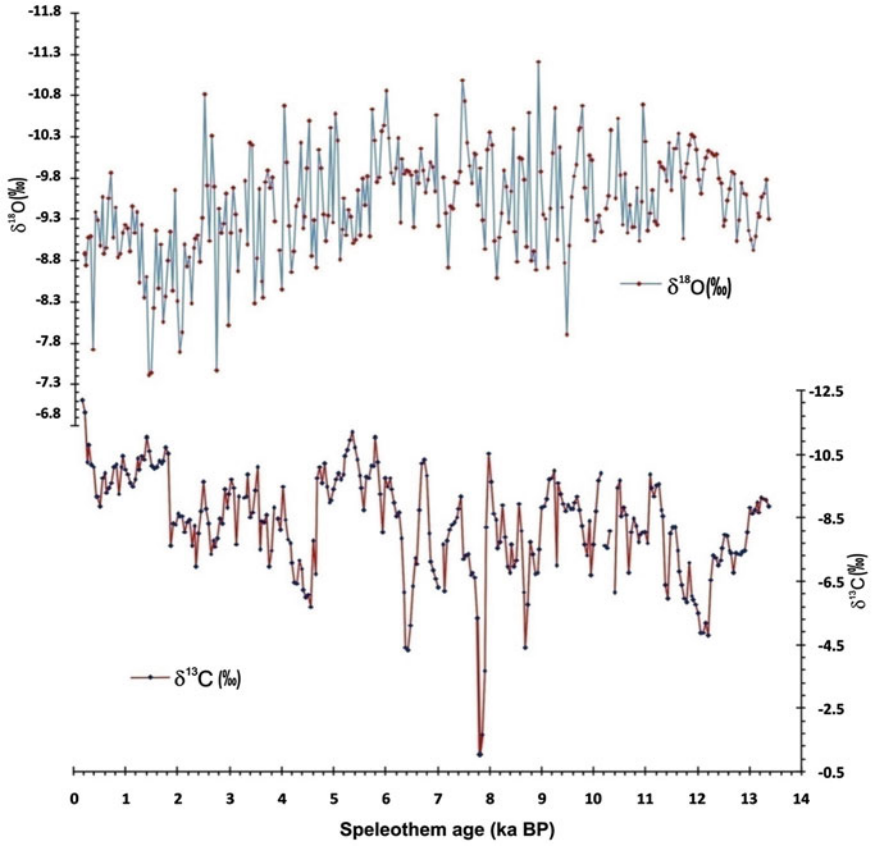

Fig. 4.25 $\delta^{18}O$ and $\delta^{13}C$ values in BR-1 stalagmite

References

Datte PS, Tyagi SK, Chandrasekharan H (1991) Factors controlling stable isotope composition of rainfall in New Delhi, India. J Hydrol 128:223–236

Dietzel M, Gussone N, Eisenhauer A (2004) Co-precipitation of Sr^{2+} and Ba^{2+} with aragonite by membrane diffusion of CO_2 between 10 and 50 degrees C. Chem Geol 203:139–151

Dorale JA, Liu Z (2009) Limitations of Hendy test criteria in judging the paleoclimatic suitability of speleothems and the need for replication. J Cave Karst Stud 71:73–80

Fleitmann D, Burns SJ, Neff U, Mudelsee M, Mangini A, Matter A (2004) Palaeoclimatic interpretation of high resolution oxygen isotope profiles derived from annually laminated speleothems from Southern Oman. Q Sci Rev 23:935–945

Frisia S, Borsato A, Fairchild IJ, Mcdermott F, Selmo EM (2002) Aragonite-calcite relationships in speleothems (Grotte de Clamouse, France): environment, fabrics, and carbonate geochemistry. J Sediment Res 72:687–699

Garzione CN, Quade J, DeCelles PG, English NB (2000) Predicting paleoelevation of Tibet and the Himalaya from $\delta^{18}O$ vs. altitude gradients in meteoric water across the Nepal Himalaya. Earth Planet Sci Lett 183:215–229

GNIP, http://www.iaea.org/water

Hren MT, Bookhagen B, Blisniuk PM, Booth AL, Chamberlain CP (2009) $\delta^{18}O$ and δD of stream waters across the Himalaya and Tibetan Plateau: implications for moisture sources and paleoelevation reconstructions. Earth Planet Sci Lett 288:20–32

Huang Y, Fairchild IJ (2001) Partitioning of Sr^{2+} and Mg^{2+} into calcite under karst analogue experimental conditions. Geochim Cosmochim Acta 65:47–62

Kim ST, O'Neil JR (1997) Equilibrium and nonequilibrium oxygen isotope effects in synthetic carbonates. Geochim Cosmochim Acta 61:3461–3475

Kim ST, O'Neil JR, Hillaire-Marcel C, Mucci A (2007) Oxygen isotope fractionation between synthetic aragonite and water: influence of temperature and Mg^{2+} concentration. Geochim Cosmochim Acta 71:4704–4715

Kotlia BS, Ahmad SM, Zhao JX, Raza W, Collerson KD, Joshi LM, Sanwal J (2012) Climatic fluctuations during the LIA and post-LIA in the Kumaun Lesser Himalaya, India: evidence from a 400 yr old stalagmite record. Quat Int 263:129–138

Liu Z, Tian L, Chai X, Yao T (2008) A model-based determination of spatial variation of precipitation $\delta^{18}O$ over China. Chem Geol 249:203–212

Pande K, Padia JT, Ramesh R, Sharma KK (2000) Stable isotope systematics of surface water bodies in the Himalayan and trans-Himalayan (Kashmir) region. Proc Indian Acad Sci 109:109–115

Perrin C, Prestimonaco L, Servelle G, Tilhac R, Maury M, Cabrol P (2014) Aragonite–calcite speleothems: identifying original and diagenetic features. J Sediment Res 84:245–269

Quade J, Garzione C, Eiler J (2007) Paleovegetation reconstruction using pedogenic carbonates. Rev Mineral Geochem 66:53–87

Scholz D, Hoffmann DL (2011) StalAge—an algorithm designed for construction of speleothem age models. Quat Geochronol 6:369–382

Zhou H, Zhao J, Qing W, Feng Y, Tang J (2011) Speleothem-derived Asian summer monsoon variations in Central China, 54-46 ka. J Quat Sci 26:781–790

Chapter 5
Summary and Conclusion

Since the response of precipitation over the Indian subcontinent has not been completely linear, the ISM and WDs have distinctly different origin and dynamics (Sarkar et al. 2000). We suggest that the impact of WDs in the Himalayan region makes the monsoonal system complex to understand its behavior. High resolution palaeoclimatic records are insufficient from the Himalaya, therefore, the present records may be helpful to develop the models for ISM variability and WDs through an improved understanding of the monsoon-climate interaction. The records are also helpful to reveal the complex nature of ISM and its relationship with different climatic phenomena, e.g., ENSO, NAO and tropical mid latitude interactions.

The short term events from the Indian Himalayan domain between upper Pleistocene to Late Holocene are scattered. Prior to instrumental records, one needs to understand the past monsoon variability using high resolution archives and proxies. The well dated archives help to understand major and minor climatic events and their variability in different sectors of the Himalaya. Therefore, we studied five well dated cave stalagmites of different age brackets, e.g., Kalakot Cave (16.2–9.5 ka BP), Sainji Cave (4 ka BP to present), Dharamjali Cave (4–1.9 ka BP), Tityana Cave (3.9–1.5 ka BP) and Chulerasim Cave (1622–1950 AD) in different sectors of the Himalaya. The past precipitation is based on the $\delta^{18}O$ and $\delta^{13}C$ values.

5.1 Pleistocene to Holocene Transition (16.2–9.5 Ka BP)

The $\delta^{18}O$ Kl-3 record between 16.2 and 9.5 ka BP, has preserved a number of major events. When compared this records from NW Himalaya with the Valmiki Cave (Peninsular India) (Lone et al. 2014) for similar time span, $\delta^{18}O$ and $\delta^{13}C$ values show anti-correlation (Fig. 5.2a), proving that the upper most Pliestocene-Early Holocene climate of the Indian Himalaya differs from that of the Peninsular India. This may be largely due to two moisture sources (ISM and WDs) in Himalayan region (e.g., Kotlia et al. 2012, 2015, 2016, 2017; Liang et al. 2015) compared to only ISM in the

A. K. Singh, *High Resolution Palaeoclimatic Changes in Selected Sectors of the Indian Himalaya by Using Speleothems*, Springer Theses,
https://doi.org/10.1007/978-3-319-73597-9_5

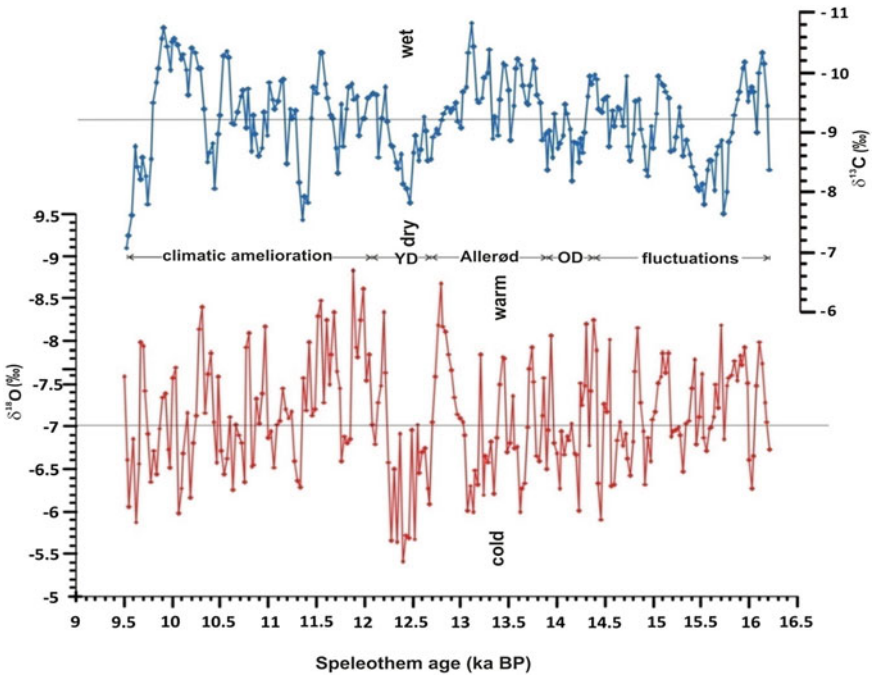

Fig. 5.1 $\delta^{18}O$ and $\delta^{13}C$ variations in KL-3 during Older Dryas (OD), Allerød period and Younger Dryas (YD)

Peninsular India. During this period, the isotopic pattern reveals three major events, e.g., Older Dryas (OD), Bølling–Allerød (BA) period and Younger Dryas (YD) at ca. 14.3–13.9, 13.9–12.7 and 12.7–12.2 ka BP respectively (Fig. 5.1). The OD and YD events are marked as weaker precipitation strength, whereas the Allerød interstadial event as wet period.

The OD is well known cold event between the Bølling and Allerød interstadial towards the end of the Pliestocene (Kotlia et al. 2016). In our records, enriched $\delta^{18}O$ and $\delta^{13}C$ values reveal that the OD stadial was a dry event. This event is also reported by Kotlia et al. (2010) at 14.3–13.8 ka BP using lake sediments from Central Indian Himalaya. The Bølling–Allerød is well marked as warm and wet phase from approximately 14.5–12.5 ka BP in Northern Hemisphere (Alley et al. 1993). In KL-3, the Allerød interstadial ranges between 13.9 and 12.7 ka BP as observed by the lowering of $\delta^{18}O$ values and this also includes a few multi decadal dry oscillations. The Timta Cave record shows a sharp decrease in $\delta^{18}O$ values between 14.5 and 12.7 ka BP (Sinha et al. 2005) which is interpreted as strengthening in precipitation. This period is also characterized by strong carbonate precipitation and presence of aquatic plants in the interiors (Tso Kar basin) of Northwest Himalaya (Wünnemann et al. 2010).

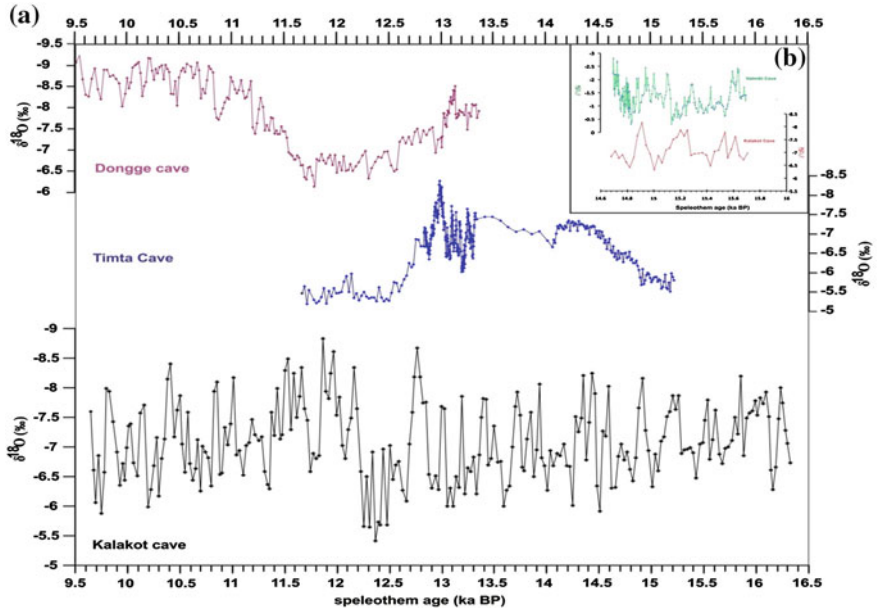

Fig. 5.2 **a** Comparison of $\delta^{18}O$ values in Dongge, Timta and KL-3 for similar time duration, **b** Inset shows Comparison of KL-3 $\delta^{18}O$ record with Valmiki Cave (under the influence of ISM) for same time duration. Note the near anti-correlation

The YD event in the Kl-3 stalagmite ranges between 12.7 and 12.2 ka BP. This is considered as a post glacial cooling event (Bond et al. 1993; Alley 2000) between 12.9 and 11.7 ka BP (Adams et al. 1999; Carlson 2013) and has been recognized throughout Europe, North Atlantic, North Pacific Ocean, Asia and North America tropics in both ocean and terrestrial sediments (Clark et al. 2002; Shakun and Carlson 2010). The Dongge Cave records also support the YD event between 13 and 11.5 Ka BP (Fig. 5.2) (Cheng et al. 2009) and so also the Mediteranian records (Dormoy et al. 2009), both show almost similar to the Kl-3 record.

In the Asian region, the YD event has not been identified particularly due to the poor chronology and low resolution. We compared of KL-3 record with Timta Cave (12.7–11.6 ka BP) of Central Himalaya (Sinha et al. 2005) and observed a similar trend in a general but a slight shift in the duration of the YD event (Fig. 5.2b). Therefore the initiation of the YD may very even within the Himalaya depending upon the behavior of WDs (Kotlia et al. 2016).

From Ladakh region, this event is recorded from the Tsokar lake at 12.5–11.6 ka BP (Wünnemann et al. 2010) as well as, western Tibet lakes (Van Campo and Gasse 1993; Van Campo et al. 1996). From Tibet and China, a maximum cooling of this event began at 12.8 ka BP in the Qinghai Lake, 12 ka BP in Guliya ice core and 12.5 ka BP in Erhai Lake (Jing et al. 2007). In the Himalayan region, the pollen analysis from Chandra Tal sediments show YD event between 12.9 and 11.6 ka BP

(Rawat et al. 2012) and has also been recorded from other lake sediments between 12–11 ka BP (Basavaiah et al. 2004) and 12.8–12.7 ka BP in the Higher Central Himalaya (Kotlia and Joshi 2013). This short term event has also been reported from the Eastern Kumaun Himalaya between 13.5 and 12 ka BP (Kotlia et al. 2010). All these data support that the YD event may be prominent in the Indian Himalaya, Tibet and China although the inception and duration may vary depending on altitude, location and response time.

5.2 Mid Holocene—Present (4 Ka BP—Present)

The $\delta^{18}O$ values in SA-1, DH-1 and TCS stalagmites show higher variation (above 3–4‰). However the stalagmites from the ISM core locations (Berkelhammer et al. 2010; Sinha et al. 2011) indicate variation of only about 2‰ (Fig. 5.3a). The $\delta^{18}O$ variability in a Qunf Cave stalagmite is reported as low as 1.5‰ (Fleitmann et al. 2007). The Dongge Cave $\delta^{18}O$ time series represents characteristics of the East Asian monsoon and shows only a variation of <2‰ (Dykoski et al. 2005; Wang et al. 2005). Therefore, we believe that the higher variations in $\delta^{18}O$ from the Himalayan speleothems reflect the additional contribution of WDs. Since the WDs provide precipitation with relatively high $\delta^{18}O$ values, this would result in an additional increase in the $\delta^{18}O$ signal of the stalagmites, which is by far larger than in the Peninsular Indian speleothems (Kotlia et al. 2015).

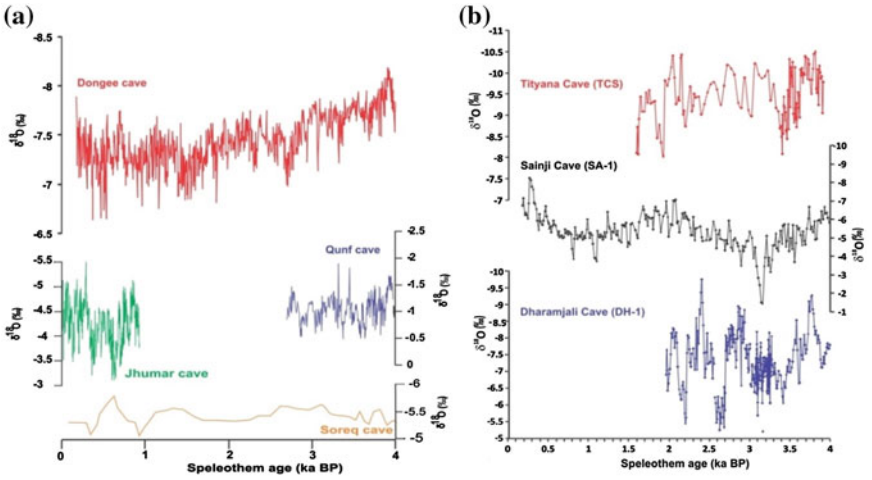

Fig. 5.3 $\delta^{18}O$ values in various stalagmites, influenced primarily by single monsoon. **a** Soreq Cave (Bar-Matthews et al. 2003), Jhumar Cave (Sinha et al. 2011), Qunf Cave (Fleitmann et al. 2007), Dongge Cave (Wang et al. 2005), **b** $\delta^{18}O$ values in the Himalayan stalagmites; Dharamjali Cave (DH-1), Sainji Cave (SA-1) and Tityana Cave (TCS) influenced by both ISM and WDs

Based on the Global Network of Isotopes in Precipitation data (GNIP, http://www.iaea.org/water) long-term (1961–2001) mean for $\delta^{18}O$ values of ISM and WDs at New Delhi (300 km away from Sainji Cave) are −6.8 and 0.8‰ respectively. However, New Delhi lies at an altitude of about 200 m and Sainji is at an elevation of 1478 m. This altitude difference (ca. 1200 m) is responsible for lower values at higher elevations with the gradient about ~0.3‰ per 100 m (Gonfiantini et al. 2001). This means that $\delta^{18}O$ values for Sainji cave location should range between the −10.4 and −4.4‰ for ISM and WDs respectively. However, we measured the $\delta^{18}O$ values of three drip water samples at Sainji Cave −7.4‰ (pre ISM) and −8.2 and −8.0‰ (post ISM) and with an average of −7.86‰, which is higher than the isotopic composition of precipitation during the ISM. This confirms that the drip water has a significant contribution from the WDs which prevail during the winter months in this region (Datte et al. 1991; Kotlia et al. 2012, 2015).

In general, the $\delta^{18}O$ results from SA-1, DH-1 and TCS can be correlated within the age uncertainties. The $\delta^{18}O$ results of these cave samples reveal a precipitation failure from 4 to 3.5 ka BP (Fig. 5.4) which can be linked with the decline of the Harrapan-Indus civilization from 4 ka BP onwards which was completely collapsed between 3.5 and 3 ka BP (Leipe et al. 2014), more precisely at 3.2 ka BP (Kotlia et al. 2015). Our records show peak aridity between 3.5 and 3.1 ka BP, a distinct arid event in South Asia (Madella and Fuller 2006; MacDonald 2011). This drought period can also be linked with disappearance of Ghaghar River and related civilization around 3.5 ka BP (Tripathi et al. 2004). The alpine peat record from Central Indian Himalaya indicates an arid event between 4 and 3.5 ka BP within the age uncertainties (Phadtare 2000) which may be close to our improved chronology.

Similarly, the reduced precipitation between 4.5 and 2.5 ka BP in Soreq Cave with heavier $\delta^{18}O$ values around 3.5 ka BP (Bar-Matthews et al. 2003) is considered as an arid event (Fig. 5.5). The reduced precipitation has also been observed in the Central Himalaya from ~4 to ~3 ka BP using $\delta^{18}O$ with the lowest precipitation around ~3.2–3.1 ka BP (Kotlia et al. 2015). The increased $\delta^{18}O$ values at Qunf Cave between 7.8 and 2.7 ka BP with higher amplitude aridity peak around 3.37 ka BP (Fleitmann et al. 2007) show declining precipitation (Fig. 5.5). The reduced precipitation occurred within this period in the Dongge area with an abrupt positive shift in $\delta^{18}O$ at 3.5 ka BP (Dykoski et al. 2005).

The progressive lowering of Tso Moriri lake level has been observed between 5.5 and 2.7 ka BP in NW Himalaya (Mishra et al. 2015). Further, other lake and peat records from NW Himalaya have also registered intensification of arid phase around 4–3.5 ka BP (Chauhan and Sharma 1996; Kotlia et al. 1997; Phadtare 2000). The western Tibet lake records from Sumxi Co basin (Gasse et al. 1991, 1996; Van Campo and Gasse 1993) and Bangong Co basin (Fontes et al. 1996; Van Campo et al. 1996) indicate the signatures of weak precipitation between 4.0 and 3.5 ka BP. Similarly, the decline of human civilization reported from the Middle East, North Africa and the Egyptian kingdom between 4.5 and 2.5 ka BP (Hassan and Stucki 1987; Weiss et al. 1993; Bar-Matthews et al. 2003), also supports reduction in precipitation from 4.0 ka BP onwards for about a millennium.

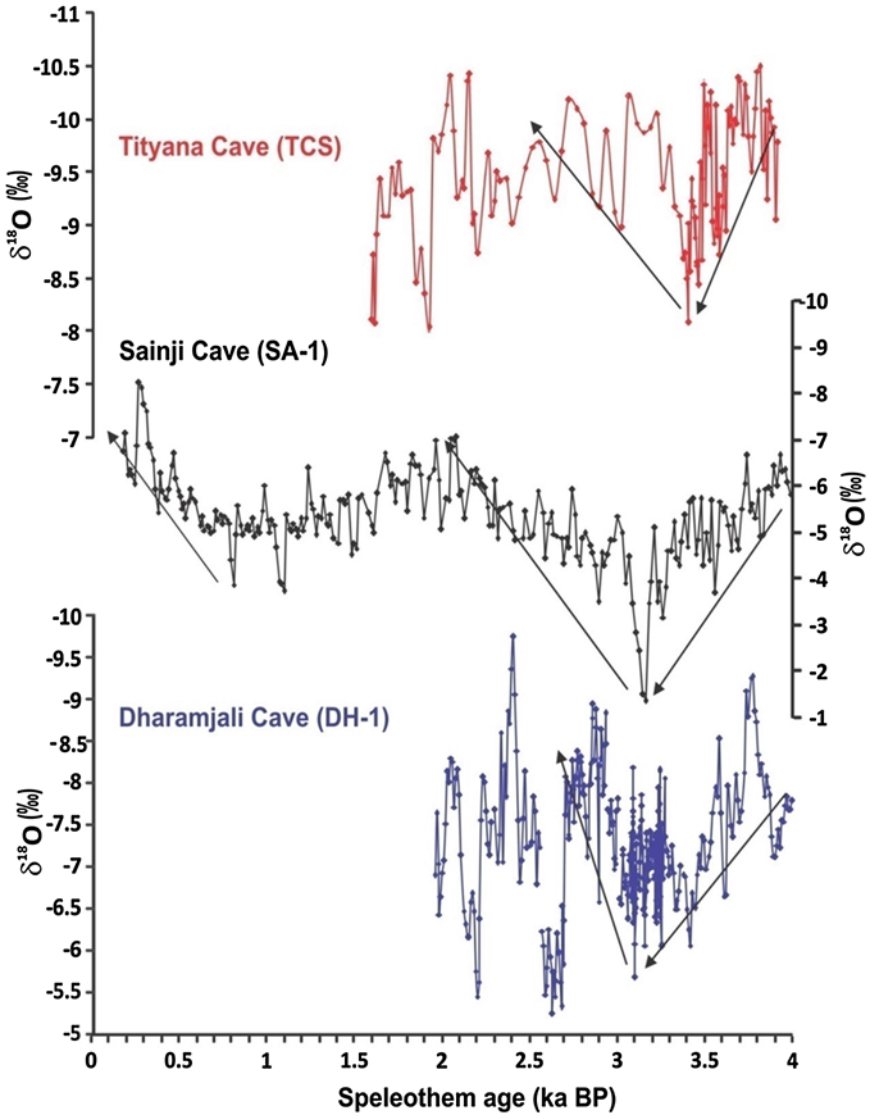

Fig. 5.4 $\delta^{18}O$ variation in DH-1, SA-1 and TCS

The lighter $\delta^{18}O$ values in SA-1 and TCS reflect wetter climatic conditions between 3 and 2 ka BP. This is coherent with the results obtained by Kotlia et al. (2015). However, the Dongge Cave record is not coherent with our record while, the Soreq cave record seems having similar fluctuations (Fig. 5.5). The high organic productivity and greater chemical weathering within the Garhwal Himalayan lakes show wetter climate between ca. 3.5 and 1.8 ka BP (Kotlia and Joshi 2013). Similarly,

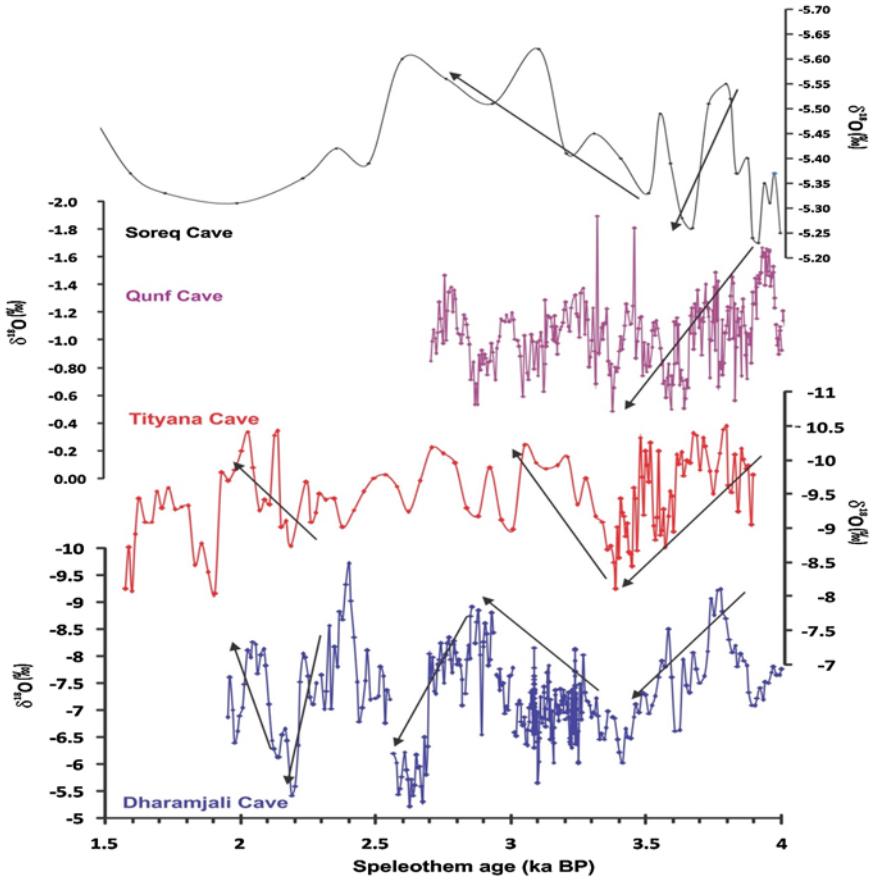

Fig. 5.5 Comparison of TCS and DH-1 $\delta^{18}O$ values with Qunf (Fleitmann et al. 2007) and Soreq Cave records (Bar-Matthews et al. 2003)

the $\delta^{18}O$ results demonstrating humid conditions from ~3.2 ka BP onwards can also be correlated with the nearby sites (29° 23′N 79° 31′E; altitude, 1980 m) at 3.2 ka BP (Gupta 2008).

The DH-1 results show a sudden increase in $\delta^{18}O$ values between 2.7 and 2.5 ka BP, marked as a prominent drought event (Fig. 5.5). Similarly, peak aridity in Garhwal Himalaya around 2.8 ka BP (Phadtare and Pant 2005) and abnormally dry interval at 2.7 ka BP in the Northwest Himalaya (Bookhagen et al. 2005) may be correlated with this drier spell of our record. The arid events of 2.7 and 2.1 ka BP are well connected with Tso Morari lake records (e.g., Leipe et al. 2014). The low solar activity is recorded at ca. 2.7 Ka BP indicating very weak ISM intensity during the Holocene (e.g., Fleitmann et al. 2003; Wang et al. 2005). After this drought event, the $\delta^{18}O$ values show wetter climatic conditions from 2.5 to 2.3 ka BP that are well

connected with another stalaglite record from Kumaun Himalaya (Kotlia et al. 2015). The favorable climatic conditions from ~3.3 to 2.0 ka BP (Rawat et al. 2015) are also suggested based on the pollen records from Lahaul, NW Himalaya and the high monsoonal runoff from the Indus River during ~3.5 to 2.2 ka BP (von Rad et al. 1999). The DH-1 and TCS results reflect that precipitation failure from 2.3 to 2.1 ka BP. Speleothem record from the Pokhara valley (Central Nepal) points to the deposition of aragonite between 2.3 and 1.5 ka BP under the reduced monsoonal precipitation and increased aridity (Denniston et al. 2000).

The $\delta^{18}O$ values of TCS and DH-1 prove the wetter climatic conditions between 2.1 and 2.0 ka BP. This wet event is also described from lake sediments of Deorital area at 2.3–2.0 ka BP (Chauhan et al. 2000) and from Pinder valley at ca. 2.3–1.6 ka BP (Rühland et al. 2006). A booming Painted Grey Ware culture in the Indus Valley existed around 2.3 ka BP and is consistent with improvement in climate (Pant 2003). Prolonged wet periods are recorded from Soreq Cave around ca. 2.0 ka BP and conversely relatively dry periods, marked by higher $\delta^{18}O$ values after 1.9 ka BP (Orland et al. 2009). Comparatively cooler and moist climate has also been observed around 2 ka BP in the Gangotri region, Garhwal Himalaya (Kar et al. 2002). Pollen data obtained from the Spiti region also signify cool/dry conditions between ~2.0 and 1.0 ka BP (Mazari et al. 1995). The increased moisture availability at about ~2 ka BP is associated with wetter climate as shown from a number of the Central Asian sites (Lister et al. 1991; Liu et al. 1998).

The Medieval Climatic Anomaly (MCA) (Crowley and Lowery 2000; Mann et al. 2009; Ledru et al. 2013) was a time of warm climate in North Atlantic region and its time span is ~950 to 1250 AD and its signatures have been observed worldwide from 950 to 1250 AD (Broecker 2001). In our SA-1 records, the MCA ranges from 750 to 1250 AD with uneven pattern of $\delta^{18}O$ values and do not support the major warming. There MCA is still debated for not being synchronous all over the globe (Bradley 1992; Bradley and Jones 1993). The Himalayan records (see Sanwal et al. 2013) show a little variation towards warm and the MCA is described as a regional scale event rather than global event (Yang et al. 2003). However, Liang et al. (2015) studied another stalagmite record from Himalayan foothills which revealed drier conditions during the MCA. Various proxy records from Tibetan Plateau show that the north-eastern sector of the Plateau had maximum warmth interval during the MCA; while in the case of the western sector, the warm events occur near the end of the Roman Warm Period, and in the southern sector, maximum warming is recorded during both warm periods (Yang et al. 2003). Zhang et al. (2009) argued that during the MCA, the climate was humid in the north of Xinjiang. Pollen analysis of Bosten Lake (Chen et al. 2006) also supports a warm MCA but was dry in the south of Xinjiang. This makes MCA asynchronous in the Himalaya, Tibet and China.

The little Ice Age (LIA) was a cold period that occurred after MCA and extended from 16th to 19th centuries (Lamb 1972; Mann et al. 1998). The signals of this event are present in both the hemispheres but not in a globally synchronous manner (Bradley and Jones 1993; Mann et al. 1998; Grove 2001, 2004) because of the uncertainty about the origin and extent of this event in different parts of the globe (Bradley 1992; Bradley and Jones 1993). Several archives and proxies also indicate that the

LIA was a global scale event, but it varies in precipitation pattern and magnitude of cooling in different regions (Grove 1988). The $\delta^{18}O$ values of SA-1 and CH-1 show the LIA event between 1450–1740 AD and 1622–1822 AD respectively. Study of these stalagmites show that the LIA was a wet event in the Himalayan region. Recent speleothem studies also indicate a signal of wet and warm LIA period in the Indian Himalaya (Kotlia et al. 2012, 2017; Sanwal et al. 2013; Liang et al. 2015).

The low $\delta^{18}O$ values from Sihua Cave, Beijing also designate the wet LIA from 1620 to 1900 AD, (Ku and Li 1998). Similarly, the Tibetan Plateau lake record also reflects wet LIA from 1650 to 1950 AD (Zhang et al. 2003). The $\delta^{18}O$ and $\delta^{13}C$ values of carbonate deposits from NE China have also marked the wet LIA between 1620 to 1900 AD (Ma et al. 2011). Further, $\delta^{13}C$ values of a Central Chinese stalagmite from 1475 to 1650 AD points to a wet climate (Paulsen et al. 2003). Numerous high resolution records from Central China (Chen et al. 2010) can be positively correlated with our results as wet LIA between 1500 and 1850 AD. The pollen records of the Qaidam basin of NE Tibet Plateau (Zhao et al. 2010) too support a wet LIA from 1500 to 1880 AD. The decadal scale chironomid record from Sugan Lake (Qaidam basin) also signifies a relatively humid climate during the LIA (Chen et al. 2009). The high organic matter content and low $\delta^{13}C$ values of Aibi Lake in China indicate a wet period from 1460 to 1860 AD (Wu et al. 2004). A well dated Aral sea sediment core points to an increase in the intensity of WDs during the LIA (Sorrel et al. 2007). Further, the $\delta^{18}O$ and $\delta^{13}C$ values of bulk carbonate of the Ebinur Lake of the northwest China also point towards a wet LIA (Ma et al. 2011). A trend between 1620 and 1900 AD (Hongchun et al. 1998) near Beijing and Tianjin has at least fourteen cycles of precipitation changes, with wet periods centered around 1600 AD, 1730 AD, and 1840 AD.

Previous results from Peninsular India suggest a weaker ISM during the LIA (von Rad et al. 1999; Agnihotri et al. 2002; Anderson et al. 2002; Gupta et al. 2003) but there is strong evidence of wetter condition in the Indian Himalaya (Rühland et al. 2006; Kotlia et al. 2012, 2017; Sanwal et al. 2013; Liang et al. 2015), Nepal (Denniston et al. 2000) and sites falling within the similar latitudes (e.g., Chu et al. 2002; Chen et al. 2005). The CH-1 results clearly reveal a wetter climate rather than a drier climate during the LIA. The recent studies suggest that ISM is closely associated with active, weak and break spells in the Indian core monsoon zone (Prasad and Hayashi 2007). During ISM break conditions, the moisture winds moved directly from the plains to the Himalayan foothills and the WDs extended to the southern edge of the Tibet Plateau (Raghavan 1973). Therefore, during this period, the Himalayan southern slopes received high precipitation than the core monsoon zone (Gadgil 2003). Thus, it may be possible that the ISM break conditions were responsible for the wet LIA in the Himalayan foot hills.

In our data, the post-LIA (from 1852 AD onwards) shows comparatively drier conditions (Fig. 5.6). The data analysis of different regions of western Himalaya reflect an increase in minimum and maximum temperatures of 1.0 and 3.4 °C during the period 1988–2008 which was accompanied by reduced precipitation (Shekhar et al. 2010). The western Himalayan tree ring have also preserved dry period from 1945 to 1974 AD (Yadav and Singh 2002). The grain size analysis of Dongdao Island

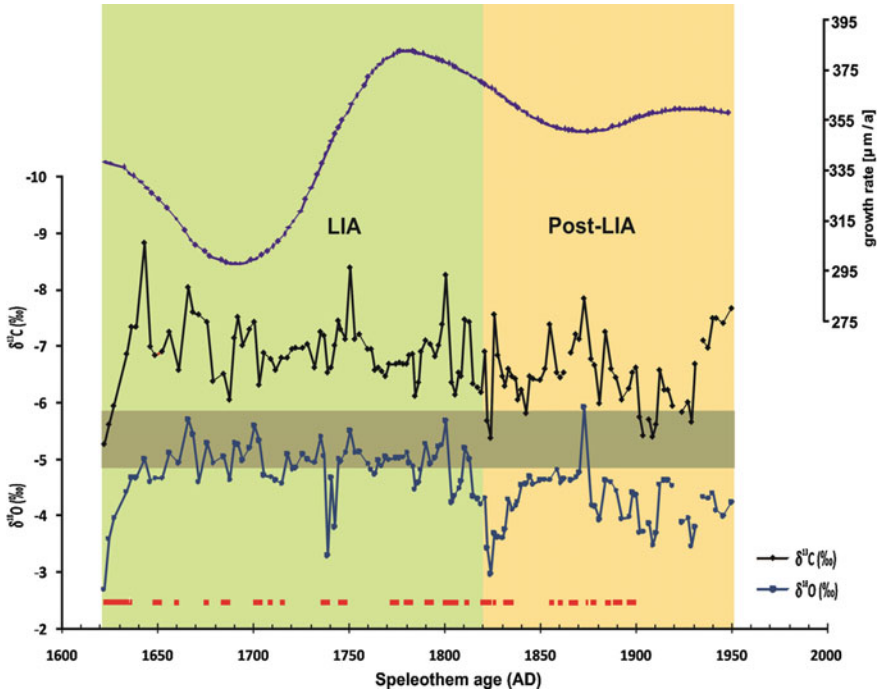

Fig. 5.6 $\delta^{18}O$ and $\delta^{13}C$ variations and growth rate in the CH-1 from ca. 1622–1950 AD. Lowermost red bars are historical north Indian droughts (after Clingingsmith and Williamson 2008). The grey horizontal panel in the background represents the $\delta^{18}O$ values of modern monsoon precipitation around CH-1 Cave site (after Kotlia et al. 2012)

(South China) reveals less precipitation during 1850–2000 AD (Yan et al. 2011). The Dasuopu ice core record in Central Himalaya also shows markedly weakened precipitation from early 1920 to present, mainly due to the increase in temperature in the Northern Hemisphere (Thompson et al. 2000; Keqin and Tandong 2003).

The CH-1 famine records can be well correlated with North Indian droughts. We compared low precipitation events of CH-1 with droughts of India from 1622 to 1900 AD (Clingingsmith and Williamson 2008). In CH-1, the 1622–1625 AD event is marked as driest event and is well linked with the Deccan famine (1630–1632 AD) of South India and is also considered as most devastating famines during the Mughal's empire (Ó Gráda 2007). The Ming Dynasty of North western china also experienced several droughts from 1627 AD onwards (Zheng et al. 2014). Likewise, Central china also underwent minor effect of this event during 1630s due to a low land-sea thermal gradient (Fang et al. 2012).

The heavier $\delta^{18}O$ values show drought events between 1740 and 1750 AD (Fig. 5.6). The well-known drought of ca. 1750 AD has also been recorded in the tree ring records from Southeast Asia (Buckley et al. 2010). Similarly, the dry events as 1700s, 1730s and 1790s–1820s have been documented through tree ring recon-

struction in the northwestern China (Wu et al. 1988; Fan et al. 2008). In fact, a major El Niño event was active in South Asia around 1791–1792 AD that forced a drought known as the Skull famine which caused the breakdown of the monsoon for four successive years starting from 1789 AD (Grove 2007).

The CH-1 record reflects prominent drought events around 1805 and 1820–1825 AD (Fig. 5.6) which may be connected with the North Indian droughts. In addition, 18th century drought events are synchronous in the western Himalaya (Singh et al. 2006) and in Mongolia (Pederson et al. 2001). The El Nino effects (scarcity around 1825–1828 AD) were responsible for a sequence of famines in north India shortly before the Agra famine (Sharma 1993). The $\delta^{18}O$ values shift suddenly towards positive values (dry events) from 1875 to 1880 AD and are well correlated with the frightful famine of 1876–1879 AD (also known as Great famine of Maharatna). The CH-1 record also documents three dry events at 1622–1625 AD, 1740–1750 AD and 1820–1825 AD (Fig. 5.6). We compared this record with tree ring records of the nearby area of similar time period (Yadav et al. 2015) and found similar multiyear droughts at 1740–1750, 1780–1790, 1820–1825 AD and wet phases in 1720–1730, 1790–1800, 1910–1920 AD.

As already mentioned in the text, the Himalayan climate particularly during Holocene shows anti-correlation with that of the core monsoon zone. We compared $\delta^{18}O$ record of CH-1 with Akalagavi Cave data from core monsoon zone (Yadava and Ramesh 2006) and found almost anti-correlation (Fig. 5.7) with low value of correlation coefficient ($R^2 = 0.002$). Thus, the Ch-1 record also supports the additional role of WDs in the Himalayan region (Kotlia et al. 2012, 2015, 2016, 2017; Sanwal et al. 2013; Liang et al. 2015).

5.3 Conclusion

1. The thesis encompasses a study of past precipitation pattern using six cave stalagmites from different parts of the Indian Himalaya. All the studied caves are situated in subtropical climatic regime and have no or minimal effects of kinetic fractionation. The stalagmites examined were KL-3 from Jammu and Kashmir; TCS and BR-1 from Himachal Pradesh; and DH-1, SA-1 and CH-1 from Uttarakhand.
2. The chronology of stalagmites was constructed on the basis of 35 U/Th and 5 AMS dates. Usually, most cave stalagmites were found to consist of acceptable amount of Uranium and Thorium resulting in lower age errors. Most U/Th dates were carried out in Heidelberg Academy of Sciences, Germany. We used StalAge for Age/depth relationship for further interpretations. Other proxies used in this research were SEM analysis, XRD and Mg/Ca ratio in order to differentiate calcite from aragonite, in addition to about 1500 samples for $\delta^{18}O$ and $\delta^{13}C$ values for reconstructing precipitation model for the past.
3. Based on the above, high resolution palaeoclimatic reconstruction was obtained for the duration of the Pleistocene-Holocene transition (16.2–9.5 ka BP) and Mid

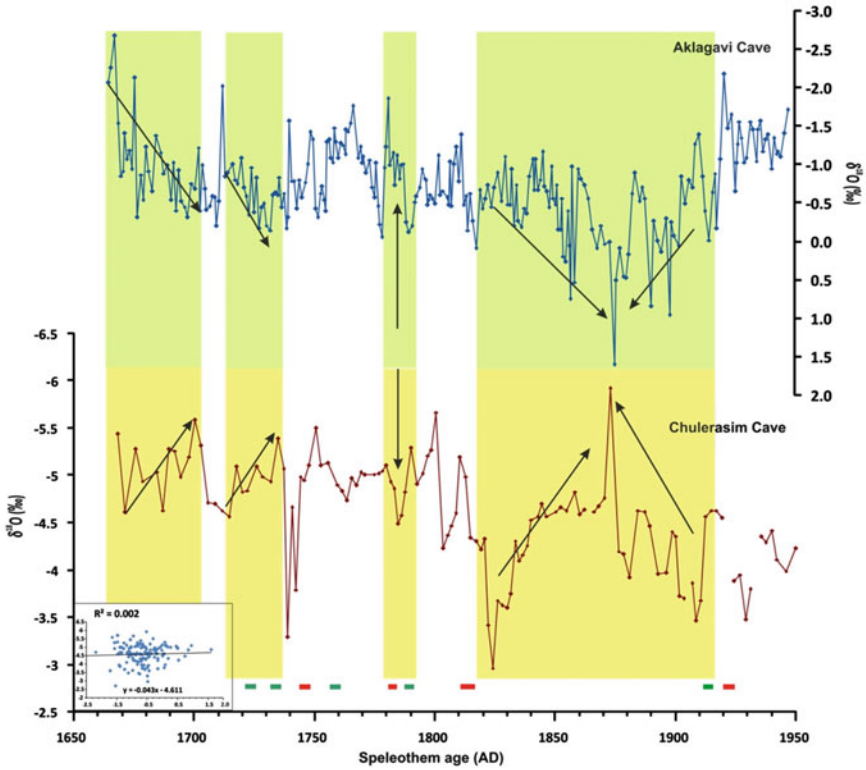

Fig. 5.7 Comparison of CH-1 $\delta^{18}O$ data with Akalagavi Cave (from core monsoon zone, Yadava and Ramesh 2006) during the same time bracket. Note the anti-correlation as the Himalaya receives additional precipitation from the WDs. The lowermost green and red colour bars are shown as wet and dry periods respectively by using tree ring data (Yadav et al. 2015)

Holocene—Present (ca. 4.0 ka BP—Present), leaving a gap between 9.5 and 4.0 ka BP.

4. Three major events were identified, e.g., Older Dryas (OD), Bølling–Allerød (BA) period and Younger Drays (YD) at ca. 14.3–13.9, 13.9–12.7 and 12.7–12.2 ka BP respectively. We compared KL-3 stalagmite records (NW Himalaya) with Timta Cave (Central Himalaya) and observed a similar trend in general but a slight shift in the duration of the YD event.
5. This is the first speleothem study in Indian Himalaya that shows a direct relationship of the past precipitation with collapse of civilization. The study showed a gradual reduction in the precipitation from 4 ka BP onwards for about a millennium with a peak arid period between 3.2 and 3.1 ka BP with age uncertainties. Such a declining pattern in precipitation is correlated with fall of the Harrapan-Indus civilization which, as we suggest, finally collapsed due to severe scarcity of

water reserves at 3.1 ka BP. However, the climate became favorable after 3.0 ka BP indicating enhanced precipitation for another millennium with a few arid pulses.

6. Considering a very high variability in the $\delta^{18}O$ and $\delta^{13}C$ values particularly from SA-1, DH-1 and TCS, we believe that the precipitation in the Himalayan foothills was a result of two sources of moisture and therefore we suggest that the WDs contributed significantly in the total rainfall during the Holocene period in the Himalaya. This must be a reason for anti-correlation in the climatic pattern from Mid-Holocene onwards between Himalaya and Peninsular India, the former received substantial precipitation from WDs.
7. In our records, the LIA covers a time span of 1622 to 1820 AD during which the climate was wetter compared to that in the post-LIA period (1820–1950 AD). During ISM break conditions, the moisture winds moved directly from the south to the Himalayan foothills and the WDs extended to the southern edge of the Tibet Plateau. As a result, during this period, the Himalayan southern slopes received high precipitation than the core monsoon zone. Thus, it is very much possible that the continuous ISM break conditions were responsible for the wet LIA in the Himalayan foot hills.
8. We compared isotope records of the CH-1 with the tree ring chronologies of the nearby area for the same duration and found that decadal scale droughts (1740–1750, 1780–1790, 1820–1825 AD) and wetter periods (1720–1730, 1790–1800, 1910–1920 AD) are positively correlated.

References

Adams J, Maslin M, Thomas E (1999) Sudden climate transitions during the Quaternary. Prog Phys Geogr 23:1–36

Agnihotri R, Dutta K, Bhushan R, Somayajulu BLK (2002) Evidence for solar forcing on the Indian monsoon during the last millennium. Earth Planet Sci Lett 198:521–527

Alley RB (2000) The Younger Dryas cold interval as viewed from Central Greenland. Quatern Sci Rev 19:213–226

Alley RB, Meese DA, Shuman CA, Gow AJ, Taylor KC, Grootes PM, White JWC, Ram M, Waddington ED, Maylewski PA, Zielinski GA (1993) Abrupt increase in Greenland snow accumulation at the end of the Younger Dryas event. Nature 362:527–529

Anderson DM, Overpeck J, Gupta AK (2002) Increase in the Asian southwest monsoon during the past four centuries. Science 297:596–599

Bar-Matthews M, Ayalon A, Gilmour M, Matthews A, Hwkesworth CJ (2003) Sea-land oxygen isotopic relationships from planktonic foraminifera and speleothems in the Eastern Mediterranean region and their implication for paleorainfall during interglacial intervals. Geochim Cosmochim Acta 67:3181–3199

Basavaiah N, Juyal N, Pant RK, Yadava MG, Singhvi AK (2004) Late Quaternary climate changes reconstructed from mineral magnetic studies from proglacial lake deposits of Higher Central Himalaya. J Geophys Union 8(1):27–37

Berkelhammer M, Sinha A, Mudelsee M, Cheng H, Edwards RL, Cannariato K (2010) Persistent multidecadal power of the Indian Summer Monsoon. Earth Planet Sci Lett 290:166–172

Bond G, Broecker W, Johnsen S, McManus J, Labeyrie L, Jouzel J, Bonani G (1993) Correlations between climate records from North Atlantic sediments and Greenland ice. Nature 365:143–147

Bookhagen B, Thiede RC, Strecker MR (2005) Late Quaternary intensified monsoon phases control landscape evolution in the northwest Himalaya. Geology 33:149–152
Bradley RS, Jones PD (1993) 'Little Ice Age' summer temperature variations: their nature and relevance to recent global warming trends. Holocene 3:367–376
Bradley RS (1992) When was the "Little Ice Age"? In: Mikami T (eds) Proceedings of the international symposium on the little ice age climate. Tokyo Metropolitan University, Tokyo, pp 1–4
Broecker WS (2001) Was the medieval warm period global? Science 291:1497–1499
Buckley BM, Anchukaitis KJ, Penny D, Fletcher R, Cook ER, Sano M, Nam LC, Wichienkeeo A, Minh TT, Hong TM (2010) Climate as a contributing factor in the demise of Angkor, Cambodia. Proc Natl Acad Sci USA 107(15):6748–6752
Carlson AE (2013) The younger Dryas climate event In: Elias SA (eds) The encyclopedia of quaternary science. Elsevier, Amsterdam, vol 3, pp 126–134
Chauhan MS, Sharma C (1996) Pollen analysis of mid-Holocene sediments from Kumaon Himalaya. Geol Surv India Spec Publ 21:257–269
Chauhan MS, Mazari RK, Rajagopalan G (2000) Vegetation and climate in upper Spiti region, Himachal Pradesh during late Holocene. Curr Sci 79(3):373–377
Chen FH, Chen JH, Homes JA, Boomer I, Austin P, Gates JB, Wang NL, Brooks SJ, Zhang JW (2010) Moisture changes over the last millennium in arid central Asia: a review, synthesis and comparison with monsoon region. Quatern Sci Rev 29:1055–1068
Chen J, Chen F, Zhang E, Brooks SJ, Zhou A, Zhang J (2009) A 1000-year chironomid-based salinity reconstruction from varved sediments of Sugan Lake, Qaidam Basin, arid Northwest China, and its palaeoclimatic significance. Chin Sci Bull 54(20):3749–3759
Chen J, Wan G, Zhang DD, Chen Z, Xu J, Xiao T, Huang R (2005) The 'Little Ice Age' recorded by sediment chemistry in Lake Erhai, southwest China. Holocene 15:925–931
Chen FH, Xiaozhong H, Jiawu Z, Holmes JA, Jianhui C (2006) Humid Little Ice Age in arid central Asia documented by Bosten Lake, Xinjiang, China. Sci China (Series D) 49(12):1280–1290
Cheng H, Edwards RL, Broecker WS, Denton GH, Kong X (2009) Ice age terminations. Science 326:248–252
Chu G, Liu J, Sun Q, Lu H, Gu Z, Wang W, Liu T (2002) The 'Mediaeval Warm Period' drought recorded in Lake Huguangyan, tropical South China. Holocene 12:511–516
Clark PU, Pisias NG, Stocker TF, Weaver AJ (2002) The role of thermohaline circulation in abrupt climate change. Nature 415:863–869
Clingingsmith D, Williamson JG (2008) Deindustrialization in 18th and 19th century India: Mughal decline, climate shocks, and British Industrial Ascent. Explor Econ Hist 45(3):209–234
Crowley TJ, Lowery TS (2000) How warm was the Medieval Warm Period? Ambio J Human Environ 29:1–51
Datte PS, Tyagi SK, Chandrasekharan H (1991) Factors controlling stable isotope composition of rainfall in New Delhi, India. J Hydrol 128:223–236
Denniston RF, Gonzalez LA, Asmerom Y, Sharma RH, Reagan MK (2000) Speleothem evidence for changes in Indian summer monsoon precipitation over the last ~2300 Years. Quatern Res 53(2):196–202
Dormoy I, Peyron I, Combourieu NO, Goring N, Kotthoff S, Magny U, Pross J (2009) Terrestrial climate variability and seasonality changes in the Mediterranean region between 15,000 and 4000 years BP deduced from marine pollen records. Clim Past 5:615–632
Dykoski C, Edwards RL, Cheng H, Yuan DX, Cai YJ, Zhang ML, Lin YS, Qing JM, An ZS, Revenaugh J (2005) A high resolution absolute dated Holocene and deglacial Asian monsoon record from Dongge cave, China. Earth Planet Sci Lett 233:71–86
Fan ZX, Bräuning A, Yang B, Cao KF (2008) Tree ring density-based summer temperature reconstruction for the central Hengduan Mountains in southern China. Global Planet Change 65(1–2):1–11
Fang K, Go X, Chen F, Liu C, Davi N, Li J, Zhao Z, Li Y (2012) Tree-ring based reconstruction of drought variability (1615–2009) in the Kongtong Mountain area, northern China. Global Planet Change 80–81:190–197

Fleitmann D, Burns SJ, Mangini A, Mudelsee M, Kramers J, Villa I, Neff U, Al Subbary AA, Buettner A, Hippler D, Matter A (2007) Holocene ITCZ and Indian monsoon dynamics recorded in stalagmites from Oman and Yemen (Socotra). Quat Sci Rev 26:170–188

Fleitmann D, Burns SJ, Neff U, Mangini A, Matter A (2003) Changing moisture sources over the last 330,000 years in Northern Oman from fluid-inclusion evidence in speleothems. Quatern Res 60:223–232

Fontes JC, Gasse F, Gilbert E (1996) Holocene environmental changes in lake Bangong basin (western Tibet). Part I: chronology and stable isotopes of carbonates of Holocene lacustrine core. Palaeogeogr Palaeoclimatol Palaeoecol 120:25–47

GNIP, http://www.iaea.org/water

Gadgil S (2003) The Indian monsoon and its variability. Annu Rev Earth Planet Sci 31:429–467

Gasse F, Arnold M, Fontes JC, Fort M, Gilbert E, Hue A, Li Bingyan, Yuangang L, Qing L, Melieres F, Van Campo E, Fubao W, Qingsong Z (1991) A 13,000-year climate record from western Tibet. Nature 353:742–745

Gasse F, Fontes JC, Van Campo E, Wei K (1996) Holocene environmental changes in Bangong Co basin (western Tibet). Part 4. Discussions and conclusions. Palaeogeogr Palaeoecol Palaeoclimatol 120:79–92

Gonfiantini R, Roche MA, Olivry JC, Fontes JC, Zuppi GM (2001) The altitude effect on the isotopic composition of tropical rains. Chem Geol 181:147–167

Grove JM (2001) The initiation of the "Little Ice Age" in regions round the North Atlantic. Clim Change 48(1):53–82

Grove RH (2007) The great El Nino of 1789–93 and its global consequences: reconstructing an extreme climate event in world environmental history. Medieval History J 10(1–2):75–98

Grove JM (1988) The little ice age. Methuen, London, vol 22, pp 1–498

Grove JM (2004) Little ice ages: ancient and modern, vol 1. Routledge, London, p 2

Gupta A (2008) Late Quaternary vegetation and climate from temperate zone of the Kumaun Himalaya, India (with remarks on neotectonic disturbance). Acta Palaeobotanica 48(2):325–333

Gupta AK, Anderson DM, Overpeck JT (2003) Abrupt changes in the Asian southwest monsoon during the Holocene and their links to the North Atlantic Ocean. Nature 421:354–357

Hassan FA, Stucki BR (1987) Nile floods and climatic change. In: Rampino MR, Sanders JE, Newman WS, Konigsson LK (eds) climate: history, periodicity and predictability. Van Nostrand Reinhold, NewYork, pp 37–46

Hongchun LI, DeloIng GU, Tehlung KU, Stott LD, Wenji C (1998) Applications of interannual-resolution stable isotope records of speleothem: climatic changes in Beijing and Tianjin, China during the past 500 years—the $\delta^{18}O$ record. Sci China (Series D) 41(4):362–368

Jing Z, Sumin W, Guishan Y, Haifeng X (2007) Younger Dryas event and cold events in early Mid-Holocene: record from the sediment of Erhai Lake. Adv Clim Change Res 3:41–44

Kar R, Ranhotra PS, Bhattacharyya A, Sekar B (2002) Vegetation vis-a-vis climate and glacial fluctuations of the Gangotri glacier since the last 2000 years. Curr Sci 82:347–351

Keqin D, Tandong Y (2003) Monsoon variability in the Himalayas under the condition of global warming. J Meteorol Soc Jpn 81:251–257

Kotlia BS, Joshi LM (2013) Neotectonic and climatic impressions in the zone of Trans Himadri Fault (THF), Kumaun Tethys Himalaya, India: A case study from palaeolake deposits. Zeitschriftfür Geomorphologie 57(3):289–303

Kotlia BS, Bhalla MS, Sharma C, Rajagopalan G, Ramesh R, Chauhan MS, Mathur PD, Bhandari S, Chacko T (1997) Palaeoclimatic conditions in the upper Pleistocene and Holocene Bhimtal-Naukuchiatal lake basin in south-central Kumaun, North India. Palaeogeogr Palaeoclimatol Palaeoecol 130(1–4):307–322

Kotlia BS, Sanwal J, Phartiyal B, Joshi LM, Trivedi A, Sharma C (2010) Late Quaternary climatic changes in the eastern Kumaun Himalaya, India, as deduced from multi-proxy studies. Quatern Int 213:44–55

Kotlia BS, Ahmad SM, Zhao JX, Raza W, Collerson KD, Joshi LM, Sanwal J (2012) Climatic fluctuations during the LIA and post-LIA in the Kumaun Lesser Himalaya, India: evidence from a 400 yr old stalagmite record. Quatern Int 263:129–138

Kotlia BS, Singh AK, Joshi LM, Dhaila BS (2015) Precipitation variability in the Indian Central Himalaya during last ca. 4,000 years inferred from a speleothem record: impact of Indian Summer Monsoon (ISM) and Westerlies. Quatern Int 371:244–253

Kotlia BS, Singh AK, Sanwal J, Raza W, Ahmad SM, Joshi LM, Sirohi M, Sharma AK, Sagar N (2016) Stalagmite inferred high resolution climatic changes through Pleistocene-Holocene transition in Northwest Indian Himalaya. J Earth Sci Clim Change 7:338

Kotlia BS, Singh AK, Zhao Jian-Xin, Duan W, Tan M, Sharma AK, Raza W (2017) Stalagmite based high resolution precipitation variability for past four centuries in the Indian Central Himalaya: Chulerasim cave re-visited and data re-interpretation. Quat Int 444(A):35–43

Ku TL, Li HC (1998) Speleothems as high-resolution paleoenvironment archives: Records from northeastern China. J Earth Syst Sci 107(4):321–330

Lamb HH (1972) The cold little ice age climate of about 1550 to 1800. Climate: present, past and future. Methuen, London, p 107

Ledru M-P, Jomelli V, Samaniego P, Vuille M, Hidalgo S, Herrera M, Ceron C (2013) The medieval climate anomaly and the little ice age in the eastern Ecuadorian Andes. Clim Past 9:307–321

Leipe C, Demske D, Tarasov PE, HIMPAC Project Members (2014) A Holocene pollen record from the northwestern Himalayan lake Tso Moriri: implications for palaeoclimatic and archaeological research. Quat Int 348:93–112

Liang F, Brook GA, Kotlia BS, Railsback LB, Hardt B, Cheng H, Edwards RL, Kandasamy S (2015) Panigarh cave stalagmite evidence of climate change in the Indian Central Himalaya since AD 1256: Monsoon breaks and winter southern jet depressions. Quatern Sci Rev 124:145–161

Lister GS, Kelts K, Chen KZ, Jun-Qing Yu, Niessen F (1991) Lake Qinghai, China closed-basin lake levels and the oxygen isotope record for ostracoda since the latest Pleistocene. Palaeogeogr Palaeoclimatol Palaeoecol 84:141–162

Liu KB, Yao ZJ, Thompson LG (1998) A pollen record of Holocene climatic changes from the Dunde ice cap. Qinghai-Tibetan Plateau Geol 26:135–138

Lone MA, Ahmad SM, Dung NC, Shen CC, Raza W (2014) Speleothem based 1000-year high resolution record of Indian monsoon variability during the last deglaciation. Palaeogeogr Palaeoclimatol Palaeoecol 395:1–8

Ma L, Wu J, Yu H, Zeng H, Abuduwaili J (2011) The Medieval warm period and the little ice age from a sediment record of Lake Ebinur, northwest China. Boreas 40(3):518–524

MacDonald G (2011) Potential influence of the Pacific Ocean on the Indian summer monsoon and Harappan decline. Quatern Int 229:140–148

Madella M, Fuller DQ (2006) Palaeoecology and the Harappan civilisation of south Asia: a reconsideration. Quatern Sci Rev 25:1283–1301

Mann ME, Bradley RS, Hughes MK (1998) Global-scale temperature patterns and climate forcing over the past six centuries. Nature 392:779–787

Mann ME, Zhang Z, Rutherford S, Bradley RS, Hughes MK, Shindell D, Ammann C, Faluvegi G, Ni F (2009) Global signatures and dynamical origins of the little ice age and medieval climate anomaly. Science 326:1256–1260

Mazari RK, Bagati TN, Chauhan MS, Rajagopalan G (1995) Palaeoclimatic records of last 2000 years in Trans-Himalaya Lahaul-Spiti region. In: Proceedings Nagoya IGBP-Pages/REP-II symposium, pp 262–268

Mishra PK, Anoop A, Schettler G, Prasad S, Jehangi A, Menzel P, Naumann R, Yousuf AR, Basavaiah N, Deenadayalan K, Wiesner MG, Gaye B (2015) Reconstructed late Quaternary hydrological changes from Lake Tso Moriri, NW Himalaya. Quatern Int 371:76–86

Ó Gráda C (2007) Making famine history. J Econ Lit 65:5–38

Orland IJ, Bar-Matthews M, Kita NT, Ayalon A, Matthews A, Valley JW (2009) Climate deterioration in the eastern Mediterranean as revealed by ion microprobe analysis of a speleothem that grew from 2.2 to 0.9 ka in Soreq Cave, Israel. Quat Res 71:27–35

Pant GB (2003) Long-term climate variability and change over monsoon Asia. J Indian Geophys Union 7(3):125–134
Paulsen DE, Li HC, Ku TL (2003) Climate variability in central China over the last 1270 years revealed by high-resolution stalagmite records. Quatern Sci Rev 22:691–701
Pederson N, Jacoby GC, D'Arrigo RD, Cook ER, Buckley B (2001) Hydrometeorological reconstructions for Northeastern Mongolia derived from tree rings: 1651–1995. J Clim 14:872–881
Phadtare NR (2000) Sharp decrease in summer monsoon strength 4000-3500 cal yr B.P. in the central higher Himalaya of India based on pollen evidence from alpine peat. Quatern Res 53:122–129
Phadtare NR, Pant RK (2005) High resolution studies on the Holocene climate changes and monsoon variability in Kumaun-Garhwal Himalaya. DST project report, pp 42
Prasad VS, Hayashi T (2007) Active, weak and break spells in the Indian summer monsoon. Meteorol Atmos Phys 95:53–61
Raghavan K (1973) Break-monsoon over India. Mon Weather Rev 101:33–43
Rawat S, Gupta AK, Srivastava P, Sangode SJ, Nainwal HC (2015) A 13,000 year record of environmental magnetic variations in the lake and peat deposits from the Chandra valley, Lahaul: Implications to Holocene monsoonal variability in the NW Himalaya. Palaeogeogr Palaeoclimatol Palaeoecol 440:116–127
Rawat S, Phadtare NR, Sangode SJ (2012) The younger Dryas cold event in NW Himalaya based on pollen record from the Chandra Tal area in Himachal Pradesh, India. Curr Sci 102(8):1193–1198
Rühland K, Phadtare NR, Pant RK, Sangode SJ, Smol JP (2006) Accelerated melting of Himalayan snow and ice triggers pronounced changes in a valley peatland from northern India. Geophys Res Lett 33:L15709
Sanwal J, Kotlia BS, Rajendran C, Ahmad SM, Rajendran K, Sandiford M (2013) Climatic variability in central Indian Himalaya during the last 1800 years: evidence from a high resolution speleothem record. Quatern Int 304:183–192
Sarkar A, Ramesh R, Somayajulu BLK, Agnihotri A, Jull AJT, Burr GS (2000) High resolution Holocene monsoon record from the eastern Arabian Sea. Earth Planet Sci Lett 177:209–218
Shakun JD, Carlson AE (2010) A global perspective on last glacial maximum to Holocene climate change. Quatern Sci Rev 29:1801–1816
Sharma S (1993) The 1837–38 famine in Uttar Pradesh: Some dimensions of popular action. Indian Econ Social Hist Rev 30(3):337–372
Shekhar MS, Chand H, Kumar S, Srinivasan K, Ganju A (2010) Climate change studies in the western Himalaya. Ann Glaciol 51(54):105–112
Singh J, Park W-K, Yadav RR (2006) Tree-ring-based hydrological records for western Himalaya, India, since AD 1560. Clim Dyn 26:295–303
Sinha A, Berkelhammer M, Stott L, Mudelsee M, Cheng H, Biswas J (2011) The leading mode of Indian Summer Monsoon precipitation variability during the last millennium. Geophys Res Lett 38:L15703
Sinha A, Cannariato KG, Stott LD, Li HC, You CF, Cheng H, Edwards RL, Singh IB (2005) Variability of Southwest Indian summer monsoon precipitation during the Bølling–Ållerød. Geology 33:813–816
Sorrel P, Oberhänsli H, Boroffka N, Nourgaliev D, Dulski P, Röhl U (2007) Control of wind strength and frequency in the Aral Sea basin during the late Holocene. Quatern Res 67:371–382
Thompson LG, Yao T, Mosley-Thompson E, Davis ME, Henderson KA, Lin PN (2000) High-resolution millennial record of the South Asian monsoon from Himalayan ice cores. Science 289:1916–1919
Tripathi JK, Bock B, Rajamani V, Eisenhauer A (2004) Is river Ghaggar, Saraswati? geochemical constraints. Curr Sci 87(8):1141–1145
Van Campo E, Gasse F (1993) Pollen and diatom-inferred climatic and hydrological changes in Sumxi Co basin (Western Tibet) since 13,000 yr B.P. Quatern Res 39:300–313
Van Campo E, Cour P, Sixuan H (1996) Holocene environmental changes in Bangong Co basin (Western Tibet). Part 2: the pollen record. Palaeogeogr Palaeoclimatol Palaeoecol 120:49–62

von Rad U, Michels KH, Schulz H, Berger WH, Sirocko F (1999) A 5000-yr record of climate change in varved sediments from the oxygen minimum zone off Pakistan, northeastern Arabian Sea. Quatern Res 51:39–53

Wang YJ, Cheng H, Edwards RL, He YQ, Kong XG, An ZS, Wu JY, Kelly MJ, Dykoski CA, Li XD (2005) The Holocene Asian monsoon: links to solar changes and North Atlantic climate. Science 308:854–857

Weiss H, Courty MA, Wetterstrom W, Guichard F, Senior L, Meadow R, Curnow A (1993) The genesis and collapse of third millennium North Mesopotamian civilization. Science 261:995–1004

Wu JL, Liu JJ, Wang SM (2004) Climatic change record from stable isotopes in Lake Aibi, Xinjiang during the past 1500 years. Quatern Sci 24:585–590

Wu XD, Li ZY, Sun L (1988) A preliminary study on the climatic change of the Hengduan Mountains area since 1600 A.D. Adv Atmos Sci 5(4):437–443

Wünnemann B, Demske D, Tarasov P, Kotlia BS, Reinhardt C, Bloemendal J, Diekmann B, Hartmann K, Krois J, Riedel F, Arya N (2010) Hydrological evolution during the last 15 kyr in the Tso Kar lake basin (Ladakh, India), derived from geomorphological, sedimentological and palynological records. Quatern Sci Rev 29:1138–1155

Yadav RR, Singh J (2002) Tree-ring-based spring temperature patterns over the past four centuries in western Himalaya. Quatern Res 57:299–305

Yadav RR, Misra KG, Yadava AK, Kotlia BS, Misra S (2015) Tree-ring footprints of drought variability in last ~300 years over Kumaun Himalaya, India and its relationship with crop productivity. Quatern Sci Rev 117:113–123

Yadava MG, Ramesh R (2006) Stable oxygen and carbon isotope variations as monsoon proxies: a comparative study of speleothems from four different locations in India. J Geol Soc India 68:461–475

Yan H, Sun L, Oppo DW, Wang Y, Liu Z, Xie Z, Liu X, Cheng W (2011) South China Sea hydrological changes and Pacific Walker Circulation variations over the last millennium. Nat Commun 2:293

Yang B, Brauning A, Shi Y (2003) Late Holocene temperature fluctuations on the Tibetan Plateau. Quatern Sci Rev 22:2335–2344

Zhang J, Jin M, Chen F, Battarbee RW, Henderson G (2003) High-resolution precipitation variations in the Northeast Tibetan Plateau over the last 800 years documented by sediment cores of Qinghai Lake. Chin Sci Bull 48(14):1451–1456

Zhang Q, Kang S, Kaspari S, Li C, Qin D, Mayewski PA, Hou S (2009) Rare earth elements in an ice core from Mt. Everest: Seasonal variations and potential sources. Atmos Res 94:300–312

Zhao Y, Yu Z, Liu X, Zhao C, Chen F, Zhang K (2010) Late Holocene vegetation and climate oscillations in the Qaidam basin of the northeastern Tibetan Plateau. Quatern Res 73:59–69

Zheng J, Xiao L, Fang X, Hao Z, Ge Q, Li B (2014) How climate change impacted the collapse of the Ming Dynasty. Clim Change 127:169–182

Annexure A

See Table A.1.

Table A.1 $\delta^{18}O$ and $\delta^{13}C$ values in KL-3

S. No.	Code	StalAge (ka BP)	$\delta^{18}O$ (‰)	$\delta^{13}C$ (‰)
1.	KLI-1	9.646	−7.592	−7.087
2.	KLI-2	9.672	−6.604	−7.28
3.	KLI-3	9.695	−6.056	−7.615
4.	KLI-4	9.720	−6.858	−8.76
5.	KLI-5	9.746	−5.879	−8.442
6.	KLI-6	9.774	−6.572	−8.22
7.	KLI-7	9.800	−7.989	−8.586
8.	KLI-8	9.828	−7.936	−8.287
9.	KLI-9	9.860	−7.427	−7.817
10.	KLI-10	9.895	−6.91	−8.552
11.	KLI-11	9.927	−6.354	−9.508
12.	KLI-12	9.953	−6.724	−9.831
13.	KLI-13	9.975	−6.441	−10.069
14.	KLI-14	9.993	−6.984	−10.571
15.	KLI-15	10.010	−7.35	−10.749
16.	KLI-16	10.031	−7.391	−10.447
17.	KLI-17	10.058	−6.731	−10.053
18.	KLI-18	10.090	−6.514	−10.515
19.	KLI-19	10.125	−7.577	−10.573
20.	KLI-20	10.160	−7.705	−10.46
21.	KLI-21	10.194	−5.984	−10.231
22.	KLI-22	10.225	−6.278	−10.318
23.	KLI-23	10.252	−6.68	−10.06
24.	KLI-24	10.277	−7.16	−9.63
25.	KLI-25	10.301	−6.169	−10.412

(continued)

A. K. Singh, *High Resolution Palaeoclimatic Changes in Selected Sectors of the Indian Himalaya by Using Speleothems*, Springer Theses,
https://doi.org/10.1007/978-3-319-73597-9

Table A.1 (continued)

S. No.	Code	StalAge (ka BP)	$\delta^{18}O$ (‰)	$\delta^{13}C$ (‰)
26.	KLI-26	10.326	−6.803	−10.346
27.	KLI-27	10.353	−7.13	−10.08
28.	KLI-28	10.382	−8.148	−10.072
29.	KLI-29	10.412	−8.404	−9.388
30.	KLI-30	10.443	−7.167	−8.517
31.	KLI-31	10.473	−7.621	−8.678
32.	KLI-32	10.499	−7.868	−8.834
33.	KLI-33	10.523	−7.052	−8.075
34.	KLI-34	10.547	−6.575	−8.983
35.	KLI-35	10.571	−7.587	−9.281
36.	KLI-36	10.596	−6.716	−10.279
37.	KLI-37	10.621	−6.444	−10.369
38.	KLI-38	10.646	−6.632	−10.253
39.	KLI-39	10.670	−7.119	−9.17
40.	KLI-40	10.694	−6.256	−9.149
41.	KLI-41	10.718	−7.017	−9.342
42.	KLI-42	10.745	−6.909	−9.614
43.	KLI-43	10.774	−6.816	−9.703
44.	KLI-44	10.801	−6.345	−9.072
45.	KLI-45	10.828	−7.935	−9.747
46.	KLI-46	10.853	−8.097	−8.686
47.	KLI-47	10.877	−6.536	−9.296
48.	KLI-48	10.902	−6.555	−8.97
49.	KLI-49	10.927	−7.329	−8.602
50.	KLI-50	10.955	−7.038	−8.754
51.	KLI-51	10.983	−7.392	−9.346
52.	KLI-52	11.012	−8.168	−8.963
53.	KLI-53	11.040	−6.866	−9.851
54.	KLI-54	11.070	−6.944	−9.566
55.	KLI-55	11.100	−6.526	−9.401
56.	KLI-56	11.130	−7.03	−9.527
57.	KLI-57	11.160	−7.07	−9.858
58.	KLI-58	11.190	−7.458	−9.883
59.	KLI-59	11.219	−7.208	−8.487
60.	KLI-60	11.249	−7.107	−9.403
61.	KLI-61	11.279	−7.173	−9.239
62.	KLI-62	11.307	−6.59	−9.362
63.	KLI-63	11.333	−6.367	−8.164
64.	KLI-64	11.356	−6.287	−7.557
65.	KLI-65	11.377	−7.58	−7.933

(continued)

Table A.1 (continued)

S. No.	Code	StalAge (ka BP)	$\delta^{18}O$ (‰)	$\delta^{13}C$ (‰)
66.	KLI-66	11.399	−7.198	−7.841
67.	KLI-67	11.425	−7.987	−9.244
68.	KLI-68	11.453	−7.135	−9.763
69.	KLI-69	11.479	−7.202	−9.669
70.	KLI-70	11.504	−8.296	−10.34
71.	KLI-71	11.529	−8.486	−10.334
72.	KLI-72	11.556	−7.292	−9.815
73.	KLI-73	11.585	−8.248	−9.574
74.	KLI-74	11.613	−7.498	−9.283
75.	KLI-75	11.639	−7.851	−9.242
76.	KLI-76	11.665	−8.34	−8.743
77.	KLI-77	11.692	−7.65	−8.325
78.	KLI-78	11.720	−7.457	−9.475
79.	KLI-79	11.746	−6.588	−8.783
80.	KLI-80	11.771	−6.893	−9.407
81.	KLI-81	11.799	−6.803	−9.76
82.	KLI-82	11.831	−6.849	−9.811
83.	KLI-83	11.863	−8.824	−9.564
84.	KLI-84	11.892	−7.935	−9.601
85.	KLI-85	11.917	−7.814	−8.955
86.	KLI-86	11.941	−8.246	−9.254
87.	KLI-87	11.968	−8.611	−9.236
88.	KLI-88	11.995	−7.541	−9.574
89.	KLI-89	12.023	−7.845	−9.639
90.	KLI-90	12.049	−7.019	−9.647
91.	KLI-91	12.076	−6.799	−9.625
92.	KLI-92	12.104	−7.288	−8.601
93.	KLI-93	12.133	−7.49	−9.245
94.	KLI-94	12.162	−8.338	−9.765
95.	KLI-95	12.193	−7.642	−9.188
96.	KLI-96	12.224	−6.587	−8.79
97.	KLI-97	12.255	−5.654	−8.759
98.	KLI-98	12.285	−6.5	−8.498
99.	KLI-99	12.313	−5.648	−8.401
100.	KLI-100	12.340	−6.914	−8.645
101.	KLI-101	12.364	−5.409	−8.135
102.	KLI-102	12.389	−5.73	−8.055
103.	KLI-103	12.414	−5.688	−7.832
104.	KLI-104	12.442	−6.96	−8.659
105.	KLI-105	12.473	−5.682	−8.952

(continued)

Table A.1 (continued)

S. No.	Code	StalAge (ka BP)	$\delta^{18}O$ (‰)	$\delta^{13}C$ (‰)
106.	KLI-106	12.503	−7.029	−8.535
107.	KLI-107	12.531	−6.452	−8.717
108.	KLI-108	12.560	−6.697	−9.278
109.	KLI-109	12.591	−6.751	−9.025
110.	KLI-110	12.624	−6.269	−8.527
111.	KLI-111	12.657	−6.083	−8.563
112.	KLI-112	12.687	−7.049	−8.941
113.	KLI-113	12.713	−7.589	−9.05
114.	KLI-114	12.740	−8.186	−8.992
115.	KLI-115	12.766	−8.672	−9.223
116.	KLI-116	12.793	−8.178	−9.332
117.	KLI-117	12.819	−7.739	−9.431
118.	KLI-118	12.847	−7.758	−9.342
119.	KLI-119	12.876	−6.541	−9.396
120.	KLI-120	12.906	−6.303	−9.503
121.	KLI-121	12.937	−6.508	−9.202
122.	KLI-122	12.966	−6.28	−9.079
123.	KLI-123	12.994	−7.682	−9.68
124.	KLI-124	13.022	−7.643	−9.762
125.	KLI-125	13.049	−6.006	−10.349
126.	KLI-126	13.078	−6.309	−10.839
127.	KLI-127	13.108	−5.997	−10.439
128.	KLI-128	13.137	−6.494	−9.561
129.	KLI-129	13.165	−6.317	−9.509
130.	KLI-130	13.191	−7.848	−9.593
131.	KLI-131	13.218	−6.203	−9.917
132.	KLI-132	13.246	−6.65	−9.993
133.	KLI-133	13.276	−6.585	−10.396
134.	KLI-134	13.304	−6.826	−8.907
135.	KLI-135	13.329	−6.207	−9.255
136.	KLI-136	13.353	−6.868	−8.965
137.	KLI-137	13.376	−7.495	−9.542
138.	KLI-138	13.397	−7.823	−10.15
139.	KLI-139	13.420	−7.799	−10.137
140.	KLI-140	13.445	−6.697	−9.713
141.	KLI-141	13.471	−6.804	−8.879
142.	KLI-142	13.499	−7.354	−9.442
143.	KLI-143	13.529	−6.741	−10.074
144.	KLI-144	13.559	−6.761	−10.234
145.	KLI-145	13.589	−5.994	−10.138

(continued)

Table A.1 (continued)

S. No.	Code	StalAge (ka BP)	$\delta^{18}O$ (‰)	$\delta^{13}C$ (‰)
146.	KLI-146	13.617	−6.27	−9.782
147.	KLI-147	13.644	−6.342	−9.504
148.	KLI-148	13.670	−6.999	−9.478
149.	KLI-149	13.695	−7.685	−9.791
150.	KLI-150	13.720	−7.925	−10.211
151.	KLI-151	13.744	−7.533	−10.064
152.	KLI-152	13.764	−6.663	−9.626
153.	KLI-153	13.787	−6.592	−9.499
154.	KLI-154	13.815	−7.131	−8.881
155.	KLI-155	13.848	−7.58	−8.975
156.	KLI-156	13.881	−6.505	−8.372
157.	KLI-157	13.907	−6.956	−9.035
158.	KLI-158	13.930	−8.066	−8.576
159.	KLI-159	13.954	−6.811	−9.325
160.	KLI-160	13.98	−6.688	−8.738
161.	KLI-161	14.007	−6.267	−8.813
162.	KLI-162	14.035	−6.944	−8.948
163.	KLI-163	14.064	−6.678	−9.475
164.	KLI-164	14.094	−6.887	−9.332
165.	KLI-165	14.128	−6.848	−9.051
166.	KLI-166	14.161	−7.045	−8.198
167.	KLI-167	14.193	−6.681	−8.859
168.	KLI-168	14.223	−6.668	−8.825
169.	KLI-169	14.251	−6.009	−8.5
170.	KLI-170	14.276	−7.517	−8.906
171.	KLI-171	14.301	−7.257	−8.675
172.	KLI-172	14.326	−7.482	−8.998
173.	KLI-173	14.352	−8.205	−9.606
174.	KLI-174	14.378	−6.785	−9.941
175.	KLI-175	14.405	−7.418	−9.807
176.	KLI-176	14.432	−8.245	−9.983
177.	KLI-177	14.458	−7.899	−9.9
178.	KLI-178	14.483	−6.337	−9.392
179.	KLI-179	14.509	−5.914	−9.343
180.	KLI-180	14.536	−7.266	−9.55
181.	KLI-181	14.564	−7.178	−9.615
182.	KLI-182	14.593	−8.022	−8.761
183.	KLI-183	14.622	−6.3	−9.384
184.	KLI-184	14.652	−6.318	−9.108
185.	KLI-185	14.680	−6.843	−9.421

(continued)

Table A.1 (continued)

S. No.	Code	StalAge (ka BP)	$\delta^{18}O$ (‰)	$\delta^{13}C$ (‰)
186.	KLI-186	14.709	−7.05	−9.391
187.	KLI-187	14.738	−6.78	−9.12
188.	KLI-188	14.767	−6.915	−9.956
189.	KLI-189	14.794	−6.626	−8.784
190.	KLI-190	14.821	−6.422	−8.537
191.	KLI-191	14.849	−6.823	−8.976
192.	KLI-192	14.879	−7.655	−9.52
193.	KLI-193	14.911	−8.163	−9.558
194.	KLI-194	14.943	−7.279	−9.07
195.	KLI-195	14.974	−6.942	−8.769
196.	KLI-196	15.005	−6.327	−8.387
197.	KLI-197	15.034	−6.874	−8.288
198.	KLI-198	15.063	−6.596	−9.116
199.	KLI-199	15.092	−7.093	−8.734
200.	KLI-200	15.119	−7.172	−9.327
201.	KLI-201	15.147	−7.513	−9.936
202.	KLI-202	15.175	−7.596	−9.813
203.	KLI-203	15.202	−7.864	−9.784
204.	KLI-204	15.229	−7.638	−9.697
205.	KLI-205	15.255	−7.861	−9.57
206.	KLI-206	15.281	−6.885	−8.697
207.	KLI-207	15.309	−6.947	−8.71
208.	KLI-208	15.338	−6.961	−8.931
209.	KLI-209	15.367	−6.987	−9.415
210.	KLI-210	15.396	−6.898	−9.102
211.	KLI-211	15.426	−6.473	−8.609
212.	KLI-212	15.457	−7.044	−8.867
213.	KLI-213	15.487	−7.077	−8.643
214.	KLI-214	15.513	−7.453	−8.442
215.	KLI-215	15.535	−7.792	−8.289
216.	KLI-216	15.558	−6.795	−8.095
217.	KLI-217	15.584	−7.116	−8.028
218.	KLI-218	15.614	−7.62	−8.145
219.	KLI-219	15.645	−6.878	−7.799
220.	KLI-220	15.675	−6.717	−8.373
221.	KLI-221	15.705	−6.981	−8.532
222.	KLI-222	15.735	−6.996	−8.533
223.	KLI-223	15.764	−7.112	−8.043
224.	KLI-224	15.793	−7.503	−8.633
225.	KLI-225	15.821	−7.218	−8.78

(continued)

Table A.1 (continued)

S. No.	Code	StalAge (ka BP)	$\delta^{18}O$ (‰)	$\delta^{13}C$ (‰)
226.	KLI-226	15.848	−8.195	−8.888
227.	KLI-227	15.877	−6.853	−7.648
228.	KLI-228	15.905	−7.487	−8.007
229.	KLI-229	15.932	−7.579	−8.851
230.	KLI-230	15.959	−7.612	−8.998
231.	KLI-231	15.986	−7.779	−9.302
232.	KLI-232	16.013	−7.538	−9.566
233.	KLI-233	16.041	−7.83	−9.676
234.	KLI-234	16.068	−7.727	−10.067
235.	KLI-235	16.094	−7.928	−10.18
236.	KLI-236	16.118	−7.513	−9.528
237.	KLI-237	16.140	−6.613	−9.673
238.	KLI-238	16.161	−6.275	−9.755
239.	KLI-239	16.184	−6.659	−9.684
240.	KLI-240	16.208	−7.48	−8.999
241.	KLI-241	16.231	−7.996	−10.01
242.	KLI-242	16.253	−7.738	−10.326
243.	KLI-243	16.275	−7.284	−10.154
244.	KLI-244	16.298	−7.06	−9.439
245.	KLI-245	16.323	−6.732	−8.39

Annexure B

See Table B.1.

Table B.1 $\delta^{18}O$ and $\delta^{13}C$ values in SA-1

S. No.	Code	StalAge (ka BP)	$\delta^{18}O$ (‰)	$\delta^{13}C$ (‰)
1.	SAI-1	0.179	−7.447	−4.119
2.	SAI-2	0.192	−7.825	−3.366
3.	SAI-3	0.206	−6.917	−2.745
4.	SAI-4	0.219	−7.066	−2.017
5.	SAI-5	0.232	−6.928	−1.885
6.	SAI-6	0.245	−6.733	−1.574
7.	SAI-7	0.258	−7.578	−1.668
8.	SAI-8	0.271	−8.916	−1.829
9.	SAI-9	0.284	−8.812	−1.759
10.	SAI-10	0.297	−8.447	−1.444
11.	SAI-11	0.311	−7.622	−1.078
12.	SAI-12	0.324	−6.901	−0.734
13.	SAI-13	0.338	−6.840	0.108
14.	SAI-14	0.351	−6.537	0.036
15.	SAI-15	0.364	−5.903	0.899
16.	SAI-16	0.377	−5.424	0.890
17.	SAI-17	0.390	−6.276	0.763
18.	SAI-18	0.403	−5.873	0.955
19.	SAI-19	0.416	−5.713	0.827
20.	SAI-20	0.430	−5.694	0.615
21.	SAI-21	0.443	−5.910	0.783
22.	SAI-22	0.456	−6.427	0.834
23.	SAI-23	0.470	−6.706	0.943
24.	SAI-24	0.482	−6.148	0.756
25.	SAI-25	0.496	−5.884	0.578

(continued)

A. K. Singh, *High Resolution Palaeoclimatic Changes in Selected Sectors of the Indian Himalaya by Using Speleothems*, Springer Theses,
https://doi.org/10.1007/978-3-319-73597-9

Table B.1 (continued)

S. No.	Code	StalAge (ka BP)	$\delta^{18}O$ (‰)	$\delta^{13}C$ (‰)
26.	SAI-26	0.509	−5.758	0.438
27.	SAI-27	0.520	−5.498	0.279
28.	SAI-28	0.529	−5.590	0.073
29.	SAI-29	0.539	−5.295	0.334
30.	SAI-30	0.550	−5.651	0.477
31.	SAI-31	0.564	−5.902	0.351
32.	SAI-32	0.577	−5.741	0.425
33.	SAI-33	0.591	−5.635	0.452
34.	SAI-34	0.617	–	–
35.	SAI-35	0.631	−5.144	0.315
36.	SAI-36	0.644	−5.317	0.262
37.	SAI-37	0.658	−5.037	0.401
38.	SAI-38	0.671	−5.152	0.681
39.	SAI-39	0.684	−5.084	0.992
40.	SAI-40	0.696	−4.976	1.028
41.	SAI-41	0.709	−5.034	1.022
42.	SAI-42	0.721	−5.456	0.516
43.	SAI-43	0.734	−5.240	0.716
44.	SAI-44	0.746	−5.380	0.840
45.	SAI-45	0.759	−5.180	0.681
46.	SAI-46	0.772	−5.351	0.407
47.	SAI-47	0.785	−5.269	0.416
48.	SAI-48	0.798	−5.191	1.256
49.	SAI-49	0.810	−4.403	1.543
50.	SAI-50	0.823	−3.859	1.587
51.	SAI-51	0.837	−4.946	0.765
52.	SAI-52	0.850	−5.588	0.542
53.	SAI-53	0.863	−5.128	0.230
54.	SAI-54	0.877	−4.924	0.071
55.	SAI-55	0.891	−5.074	0.082
56.	SAI-56	0.904	−5.141	0.080
57.	SAI-57	0.918	−5.034	0.353
58.	SAI-58	0.932	−5.278	0.142
59.	SAI-59	0.945	−4.897	0.608
60.	SAI-60	0.959	−5.080	0.637
61.	SAI-61	0.973	−4.966	0.869
62.	SAI-62	0.987	−5.459	0.987
63.	SAI-63	1.001	−6.017	1.037
64.	SAI-64	1.015	−5.274	1.238
65.	SAI-65	1.029	−4.991	1.446

(continued)

Table B.1 (continued)

S. No.	Code	StalAge (ka BP)	$\delta^{18}O$ (‰)	$\delta^{13}C$ (‰)
66.	SAI-66	1.042	−5.257	1.622
67.	SAI-67	1.056	−5.156	2.023
68.	SAI-68	1.070	−4.654	2.039
69.	SAI-69	1.084	−3.926	2.203
70.	SAI-70	1.098	−3.879	2.225
71.	SAI-71	1.111	−3.718	2.405
72.	SAI-72	1.125	−5.384	2.389
73.	SAI-73	1.139	−5.059	2.525
74.	SAI-74	1.153	−5.013	2.518
75.	SAI-75	1.167	−5.194	2.522
76.	SAI-76	1.181	−5.049	2.636
77.	SAI-77	1.195	−4.905	2.611
78.	SAI-78	1.209	−5.276	2.618
79.	SAI-79	1.223	−5.034	2.596
80.	SAI-80	1.237	−5.300	2.481
81.	SAI-81	1.251	−6.395	2.322
82.	SAI-82	1.265	−5.612	1.992
83.	SAI-83	1.279	−5.503	2.427
84.	SAI-84	1.293	−4.928	2.717
85.	SAI-85	1.307	−5.337	2.470
86.	SAI-86	1.322	−5.300	2.455
87.	SAI-87	1.336	−5.775	2.628
88.	SAI-88	1.350	−5.194	2.565
89.	SAI-89	1.364	−5.130	2.386
90.	SAI-90	1.379	−5.386	2.216
91.	SAI-91	1.407	−4.868	2.324
92.	SAI-92	1.422	–	–
93.	SAI-93	1.436	−4.765	2.352
94.	SAI-94	1.451	−5.676	2.080
95.	SAI-95	1.465	−5.685	2.196
96.	SAI-96	1.480	−5.596	2.189
97.	SAI-97	1.494	−5.798	2.043
98.	SAI-98	1.509	−4.515	2.480
99.	SAI-99	1.523	−4.745	2.244
100.	SAI-100	1.538	−4.640	2.487
101.	SAI-101	1.582	−5.716	2.196
102.	SAI-102	1.597	−5.815	2.269
103.	SAI-103	1.612	–	–
104.	SAI-104	1.627	–	–
105.	SAI-105	1.671	−5.409	2.324

(continued)

Table B.1 (continued)

S. No.	Code	StalAge (ka BP)	$\delta^{18}O$ (‰)	$\delta^{13}C$ (‰)
106.	SAI-106	1.686	−5.143	2.419
107.	SAI-107	1.701	−4.981	1.848
108.	SAI-108	1.716	−5.838	2.025
109.	SAI-109	1.731	–	–
110.	SAI-110	1.746	–	–
111.	SAI-111	1.775	−6.722	2.244
112.	SAI-112	1.790	−6.505	2.124
113.	SAI-113	1.804	−5.995	1.923
114.	SAI-114	1.819	−6.222	1.590
115.	SAI-115	1.834	−5.653	1.784
116.	SAI-116	1.848	−6.099	1.802
117.	SAI-117	1.863	–	–
118.	SAI-118	1.878	−6.050	2.173
119.	SAI-119	1.892	−6.074	2.215
120.	SAI-120	1.922	−5.438	2.416
121.	SAI-121	1.951	−6.476	2.401
122.	SAI-122	1.965	−6.653	2.199
123.	SAI-123	1.980	−6.419	2.323
124.	SAI-124	1.995	−6.426	2.253
125.	SAI-125	2.024	−6.242	2.175
126.	SAI-126	2.038	−5.306	2.447
127.	SAI-127	2.053	–	–
128.	SAI-128	2.067	−6.152	2.242
129.	SAI-129	2.082	–	–
130.	SAI-130	2.096	−6.345	2.361
131.	SAI-131	2.111	−6.986	2.179
132.	SAI-132	2.125	−6.126	2.318
133.	SAI-133	2.168	−5.055	2.273
134.	SAI-134	2.183	–	–
135.	SAI-135	2.197	−5.720	2.073
136.	SAI-136	2.212	−5.677	2.166
137.	SAI-137	2.227	−7.025	1.843
138.	SAI-138	2.241	−6.982	1.735
139.	SAI-139	2.256	−7.050	1.544
140.	SAI-140	2.271	−5.793	1.956
141.	SAI-141	2.286	−5.880	1.988
142.	SAI-142	2.300	−5.298	2.474
143.	SAI-143	2.315	–	–
144.	SAI-144	2.330	–	–
145.	SAI-145	2.345	−6.296	2.510

(continued)

Table B.1 (continued)

S. No.	Code	StalAge (ka BP)	$\delta^{18}O$ (‰)	$\delta^{13}C$ (‰)
146.	SAI-146	2.388	−6.051	2.204
147.	SAI-147	2.403	−6.350	1.941
148.	SAI-148	2.417	−6.140	2.472
149.	SAI-149	2.460	−6.041	2.427
150.	SAI-150	2.474	−5.944	2.515
151.	SAI-151	2.503	−5.540	2.500
152.	SAI-152	2.518	−5.143	2.325
153.	SAI-153	2.547	−5.140	2.573
154.	SAI-154	2.576	−6.110	2.164
155.	SAI-155	2.591	−4.861	2.429
156.	SAI-156	2.607	−5.489	2.342
157.	SAI-157	2.622	−5.537	2.259
158.	SAI-158	2.637	–	–
159.	SAI-159	2.652	–	–
160.	SAI-160	2.681	−5.598	2.411
161.	SAI-161	2.696	−5.007	2.377
162.	SAI-162	2.711	−4.808	2.299
163.	SAI-163	2.725	–	–
164.	SAI-164	2.740	–	–
165.	SAI-165	2.755	−4.852	2.667
166.	SAI-166	2.770	−5.439	2.292
167.	SAI-167	2.785	–	–
168.	SAI-168	2.800	−4.873	2.198
169.	SAI-169	2.815	−4.923	2.117
170.	SAI-170	2.844		
171.	SAI-171	2.860	−5.895	2.409
172.	SAI-172	2.875	–	–
173.	SAI-173	2.891	−5.419	2.338
174.	SAI-174	2.908	−4.419	2.093
175.	SAI-175	2.926	−5.192	2.742
176.	SAI-176	2.944	−5.394	2.127
177.	SAI-177	2.962	−4.960	2.123
178.	SAI-178	2.982	−4.915	2.274
179.	SAI-179	3.002	–	–
180.	SAI-180	3.023	−4.876	2.045
181.	SAI-181	3.044	−4.319	1.911
182.	SAI-182	3.065	−4.849	1.679
183.	SAI-183	3.085	−4.671	1.975
184.	SAI-184	3.105	−5.903	1.942
185.	SAI-185	3.124	−5.377	1.900

(continued)

Table B.1 (continued)

S. No.	Code	StalAge (ka BP)	$\delta^{18}O$ (‰)	$\delta^{13}C$ (‰)
186.	SAI-186	3.142	−4.487	1.776
187.	SAI-187	3.160	−4.295	1.851
188.	SAI-188	3.178	−4.846	2.040
189.	SAI-189	3.194	−4.966	2.041
190.	SAI-190	3.210	–	–
191.	SAI-191	3.226	−4.705	2.499
192.	SAI-192	3.242	−4.547	2.520
193.	SAI-193	3.258	−4.291	2.691
194.	SAI-194	3.273	−3.488	2.880
195.	SAI-195	3.289	−4.536	2.722
196.	SAI-196	3.305	−4.277	2.856
197.	SAI-197	3.320	−4.506	2.846
198.	SAI-198	3.336	−4.820	2.991
199.	SAI-199	3.351	−4.840	2.636
200.	SAI-200	3.366	−5.341	2.872
201.	SAI-201	3.382	−4.982	2.641
202.	SAI-202	3.398	−4.598	2.549
203.	SAI-203	3.414	−5.171	2.616
204.	SAI-204	3.429	−4.155	2.722
205.	SAI-205	3.445	−3.510	2.562
206.	SAI-206	3.460	−3.120	2.706
207.	SAI-207	3.476	−2.199	3.023
208.	SAI-208	3.491	−2.085	2.592
209.	SAI-209	3.507	−4.170	2.478
210.	SAI-210	3.522	−4.636	2.348
211.	SAI-211	3.538	−5.801	2.279
212.	SAI-212	3.554	−4.179	2.244
213.	SAI-213	3.569	−4.632	1.890
214.	SAI-214	3.585	−3.857	2.496
215.	SAI-215	3.601	−4.489	2.747
216.	SAI-216	3.616	−5.307	2.987
217.	SAI-217	3.631	−5.274	2.726
218.	SAI-218	3.647	−5.900	3.035
219.	SAI-219	3.662	−5.124	2.997
220.	SAI-220	3.677	−4.979	3.068
221.	SAI-221	3.692	−5.491	3.181
222.	SAI-222	3.708	−6.078	2.920
223.	SAI-223	3.723	−5.383	3.023
224.	SAI-224	3.738	−6.347	3.109
225.	SAI-225	3.753	−6.412	3.239

(continued)

Table B.1 (continued)

S. No.	Code	StalAge (ka BP)	$\delta^{18}O$ (‰)	$\delta^{13}C$ (‰)
226.	SAI-226	3.769	−5.221	2.859
227.	SAI-227	3.784	−5.531	2.769
228.	SAI-228	3.799	−6.421	2.831
229.	SAI-229	3.815	−4.974	3.138
230.	SAI-230	3.830	−5.691	2.364
231.	SAI-231	3.845	−5.075	3.094
232.	SAI-232	3.861	−6.392	2.756
233.	SAI-233	3.877	−4.387	2.053
234.	SAI-234	3.893	−5.390	1.686
235.	SAI-235	3.909	−6.365	2.148
236.	SAI-236	3.924	−6.135	2.526
237.	SAI-237	3.939	−6.245	1.934
238.	SAI-238	3.954	−5.853	2.192
239.	SAI-239	3.969	−5.301	2.231
240.	SAI-240	3.983	−6.020	1.722
241.	SAI-241	0.179	−5.507	1.711
242.	SAI-242	0.192	−5.311	1.603
243.	SAI-243	0.206	−6.205	1.596
244.	SAI-244	0.219	−6.744	1.749
245.	SAI-245	0.232	−7.357	1.621
246.	SAI-246	0.245	−6.155	2.058
247.	SAI-247	0.258	−6.324	2.969
248.	SAI-248	0.271	−6.006	2.601
249.	SAI-249	0.284	−6.563	2.970
250.	SAI-250	0.297	−5.588	2.917
251.	SAI-251	0.311	−5.642	3.188
252.	SAI-252	0.324	−6.640	2.128
253.	SAI-253	0.338	−6.662	2.927
254.	SAI-254	0.351	−6.496	2.272
255.	SAI-255	0.364	−7.111	2.172
256.	SAI-256	0.377	−6.684	2.057
257.	SAI-257	0.390	−7.355	2.163
258.	SAI-258	0.403	−7.006	2.288
259.	SAI-259	0.416	−7.034	2.034
260.	SAI-260	0.430	−6.772	1.943
261.	SAI-261	0.443	−6.518	2.019

Annexure C

See Table C.1.

Table C.1 $\delta^{18}O$ and $\delta^{13}C$ values in DH-1

S. No.	Code	StalAge (ka BP)	$\delta^{18}O$ (‰)	$\delta^{13}C$ (‰)
1.	DHI-1	1.953	−6.866	−7.707
2.	DHI-2	1.962	−7.618	−8.595
3.	DHI-3	1.971	−7.015	−8.029
4.	DHI-4	1.981	−6.405	−6.849
5.	DHI-5	1.990	−6.606	−7.439
6.	DHI-6	2.000	−6.902	−8.294
7.	DHI-7	2.009	−7.039	−8.722
8.	DHI-8	2.019	−7.494	−8.835
9.	DHI-9	2.028	−8.109	−9.695
10.	DHI-10	2.038	−7.981	−9.057
11.	DHI-11	2.048	−8.271	−9.966
12.	DHI-12	2.058	−8.231	−10.42
13.	DHI-13	2.067	−7.687	−8.872
14.	DHI-14	2.077	−8.024	−9.635
15.	DHI-15	2.087	−8.139	−9.447
16.	DHI-16	2.097	−7.830	−9.911
17.	DHI-17	2.106	−7.109	−7.956
18.	DHI-18	2.116	−6.446	−7.313
19.	DHI-19	2.126	−6.282	−7.059
20.	DHI-20	2.136	−6.137	−6.916
21.	DHI-21	2.145	−6.136	−6.902
22.	DHI-22	2.155	−6.549	−8.516
23.	DHI-23	2.165	−6.654	−7.779
24.	DHI-24	2.174	−6.431	−6.815
25.	DHI-25	2.184	−5.727	−5.671

(continued)

A. K. Singh, *High Resolution Palaeoclimatic Changes in Selected Sectors of the Indian Himalaya by Using Speleothems*, Springer Theses,
https://doi.org/10.1007/978-3-319-73597-9

Table C.1 (continued)

S. No.	Code	StalAge (ka BP)	$\delta^{18}O$ (‰)	$\delta^{13}C$ (‰)
26.	DHI-26	2.194	−5.426	−5.246
27.	DHI-27	2.203	−5.596	−5.514
28.	DHI-28	2.213	−6.349	−7.435
29.	DHI-29	2.222	−7.535	−10.14
30.	DHI-30	2.232	−8.047	−10.57
31.	DHI-31	2.241	−7.982	−9.685
32.	DHI-32	2.251	−7.625	−7.541
33.	DHI-33	2.261	−7.235	−7.678
34.	DHI-34	2.270	−7.108	−7.371
35.	DHI-35	2.280	−7.504	−7.564
36.	DHI-36	2.290	–	–
37.	DHI-37	2.300	−7.661	−8.798
38.	DHI-38	2.309	−7.028	−8.318
39.	DHI-39	2.319	−7.363	−7.491
40.	DHI-40	2.329	−8.582	−9.445
41.	DHI-41	2.339	−7.036	−6.618
42.	DHI-42	2.349	−8.176	−8.905
43.	DHI-43	2.359	−7.811	−8.619
44.	DHI-44	2.370	−8.838	−9.934
45.	DHI-45	2.380	−8.684	−9.638
46.	DHI-46	2.390	−9.341	−9.514
47.	DHI-47	2.400	−9.722	−10.742
48.	DHI-48	2.410	−9.037	−10.310
49.	DHI-49	2.421	−8.360	−8.411
50.	DHI-50	2.431	−7.522	−8.017
51.	DHI-51	2.441	−6.791	−6.564
52.	DHI-52	2.451	−7.050	−7.232
53.	DHI-53	2.461	−7.542	−8.608
54.	DHI-54	2.471	−8.108	−10.64
55.	DHI-55	2.480	−7.190	−8.475
56.	DHI-56	2.490	–	–
57.	DHI-57	2.499	−7.227	−9.129
58.	DHI-58	2.509	−7.259	−9.788
59.	DHI-59	2.518	−7.813	−10.47
60.	DHI-60	2.527	−7.638	−10.19
61.	DHI-61	2.536	−6.758	−9.362
62.	DHI-62	2.544	−7.375	−9.182
63.	DHI-63	2.553	−7.205	−9.235
64.	DHI-64	2.561	–	–
65.	DHI-65	2.569	−6.208	−8.268

(continued)

Table C.1 (continued)

S. No.	Code	StalAge (ka BP)	$\delta^{18}O$ (‰)	$\delta^{13}C$ (‰)
66.	DHI-66	2.577	−6.036	−8.194
67.	DHI-67	2.584	−5.447	−7.476
68.	DHI-68	2.592	−5.554	−7.664
69.	DHI-69	2.599	−5.771	−7.623
70.	DHI-70	2.606	−6.226	−7.408
71.	DHI-71	2.613	−5.892	−7.536
72.	DHI-72	2.620	−5.714	−7.525
73.	DHI-73	2.627	−5.225	−6.838
74.	DHI-74	2.634	−5.727	−7.130
75.	DHI-75	2.640	−5.425	−6.514
76.	DHI-76	2.646	−5.608	−6.815
77.	DHI-77	2.653	−6.174	−6.465
78.	DHI-78	2.659	−5.929	−6.998
79.	DHI-79	2.665	−5.971	−7.063
80.	DHI-80	2.671	−5.599	−7.233
81.	DHI-81	2.677	−5.311	−6.772
82.	DHI-82	2.682	−6.504	−6.611
83.	DHI-83	2.688	−5.807	−5.913
84.	DHI-84	2.694	−6.329	−5.554
85.	DHI-85	2.699	−8.059	−6.475
86.	DHI-86	2.705	−7.592	−8.507
87.	DHI-87	2.710	−7.988	−9.599
88.	DHI-88	2.716	−7.363	−9.371
89.	DHI-89	2.721	−7.309	−9.542
90.	DHI-90	2.726	−7.844	−9.873
91.	DHI-91	2.731	−7.754	−9.720
92.	DHI-92	2.736	−7.944	−9.744
93.	DHI-93	2.742	−8.246	−10.237
94.	DHI-94	2.747	−7.901	−9.995
95.	DHI-95	2.752	−7.515	−9.861
96.	DHI-96	2.757	−8.049	−9.990
97.	DHI-97	2.762	−8.027	−9.402
98.	DHI-98	2.767	−8.235	−9.888
99.	DHI-99	2.772	−8.346	−9.971
100.	DHI-100	2.777	−7.946	−10.09
101.	DHI-101	2.782	−7.700	−9.930
102.	DHI-102	2.787	−8.216	−9.539
103.	DHI-103	2.792	−8.288	−9.827
104.	DHI-104	2.797	−8.067	−10.062
105.	DHI-105	2.802	−7.850	−10.339

(continued)

Table C.1 (continued)

S. No.	Code	StalAge (ka BP)	$\delta^{18}O$ (‰)	$\delta^{13}C$ (‰)
106.	DHI-106	2.807	−7.931	−10.244
107.	DHI-107	2.812	−7.822	−9.870
108.	DHI-108	2.817	−7.563	−10.156
109.	DHI-109	2.822	−7.087	−10.37
110.	DHI-110	2.827	–	–
111.	DHI-111	2.832	−7.318	−10.120
112.	DHI-112	2.837	−7.947	−10.181
113.	DHI-113	2.842	−8.204	−10.243
114.	DHI-114	2.848	−7.953	−10.144
115.	DHI-115	2.853	−8.751	−10.573
116.	DHI-116	2.858	−8.919	−10.411
117.	DHI-117	2.863	–	–
118.	DHI-118	2.868	−8.242	−10.288
119.	DHI-119	2.874	−8.647	−10.272
120.	DHI-120	2.879	−8.848	−10.070
121.	DHI-121	2.884	−8.038	−9.030
122.	DHI-122	2.890	−6.558	−7.694
123.	DHI-123	2.895	−8.172	−9.341
124.	DHI-124	2.901	−8.270	−9.874
125.	DHI-125	2.906	−8.616	−10.172
126.	DHI-126	2.912	−8.420	−10.414
127.	DHI-127	2.917	−7.825	−10.423
128.	DHI-128	2.923	−7.939	−10.445
129.	DHI-129	2.928	−8.812	−10.355
130.	DHI-130	2.934	−8.436	−10.290
131.	DHI-131	2.939	–	–
132.	DHI-132	2.945	−7.654	−10.059
133.	DHI-133	2.950	−7.625	−9.752
134.	DHI-134	2.956	−7.376	−9.172
135.	DHI-135	2.961	−7.772	−8.488
136.	DHI-136	2.967	−7.470	−8.360
137.	DHI-137	2.972	−7.508	−9.033
138.	DHI-138	2.978	−6.949	−8.419
139.	DHI-139	2.983	−7.067	−9.304
140.	DHI-140	2.989	−7.016	−9.107
141.	DHI-141	2.994	−7.630	−9.901
142.	DHI-142	2.999	−7.668	−9.163
143.	DHI-143	3.004	−7.787	−8.895
144.	DHI-144	3.010	–	–
145.	DHI-145	3.015	−6.587	−8.676

(continued)

Table C.1 (continued)

S. No.	Code	StalAge (ka BP)	$\delta^{18}O$ (‰)	$\delta^{13}C$ (‰)
146.	DHI-146	3.020	−6.520	−8.030
147.	DHI-147	3.025	−7.117	−8.125
148.	DHI-148	3.029	−7.177	−7.831
149.	DHI-149	3.034	−7.120	−7.664
150.	DHI-150	3.039	−6.795	−7.813
151.	DHI-151	3.043	−6.726	−7.524
152.	DHI-152	3.047	−6.748	−7.723
153.	DHI-153	3.051	−6.883	−7.546
154.	DHI-154	3.055	−6.380	−7.480
155.	DHI-155	3.059	−6.355	−7.487
156.	DHI-156	3.062	−6.631	−7.455
157.	DHI-157	3.066	−6.796	−8.334
158.	DHI-158	3.069	−7.049	−8.866
159.	DHI-159	3.072	−7.111	−9.193
160.	DHI-160	3.074	−7.341	−8.779
161.	DHI-161	3.076	−7.030	−8.237
162.	DHI-162	3.078	−7.382	−8.199
163.	DHI-163	3.080	−7.074	−8.069
164.	DHI-164	3.082	−6.616	−8.561
165.	DHI-165	3.083	−6.562	−8.811
166.	DHI-166	3.084	−7.498	−8.454
167.	DHI-167	3.085	−7.475	−8.230
168.	DHI-168	3.085	−7.395	−8.080
169.	DHI-169	3.085	−7.581	−8.162
170.	DHI-170	3.085	−7.338	−8.299
171.	DHI-171	3.086	−7.369	−8.392
172.	DHI-172	3.086	−7.079	−8.339
173.	DHI-173	3.086	−7.631	−7.461
174.	DHI-174	3.086	−8.162	−7.631
175.	DHI-175	3.086	−7.796	−8.281
176.	DHI-176	3.086	−7.378	−8.733
177.	DHI-177	3.086	–	–
178.	DHI-178	3.086	−7.224	−8.058
179.	DHI-179	3.086	−7.349	−7.453
180.	DHI-180	3.086	−6.923	−7.262
181.	DHI-181	3.086	−6.557	−7.972
182.	DHI-182	3.086	−7.055	−8.572
183.	DHI-183	3.086	−7.146	−8.366
184.	DHI-184	3.086	−6.686	−7.400
185.	DHI-185	3.086	−6.958	−7.412

(continued)

Table C.1 (continued)

S. No.	Code	StalAge (ka BP)	$\delta^{18}O$ (‰)	$\delta^{13}C$ (‰)
186.	DHI-186	3.086	–	–
187.	DHI-187	3.086	−7.064	−7.664
188.	DHI-188	3.086	−6.311	−7.720
189.	DHI-189	3.086	−6.766	−8.100
190.	DHI-190	3.086	–	–
191.	DHI-191	3.086	−6.636	−8.126
192.	DHI-192	3.086	−6.649	−8.042
193.	DHI-193	3.086	−7.133	−8.152
194.	DHI-194	3.087	−7.313	−8.023
195.	DHI-195	3.087	–	–
196.	DHI-196	3.088	−7.116	−8.009
197.	DHI-197	3.088	−6.632	−7.742
198.	DHI-198	3.089	−6.593	−7.315
199.	DHI-199	3.090	−6.737	−7.561
200.	DHI-200	3.091	−6.982	−7.821
201.	DHI-201	3.092	−6.778	−7.406
202.	DHI-202	3.094	−6.786	−7.495
203.	DHI-203	3.095	−6.938	−7.514
204.	DHI-204	3.096	−6.936	−7.548
205.	DHI-205	3.098	−6.421	−7.506
206.	DHI-206	3.100	−5.652	−7.567
207.	DHI-207	3.101	−6.058	−7.721
208.	DHI-208	3.103	−6.475	−7.712
209.	DHI-209	3.105	−6.603	−7.736
210.	DHI-210	3.107	−7.240	−7.889
211.	DHI-211	3.109	−6.864	−7.804
212.	DHI-212	3.111	−6.881	−7.961
213.	DHI-213	3.113	−6.759	−8.003
214.	DHI-214	3.115	–	–
215.	DHI-215	3.117	–	–
216.	DHI-216	3.119	−7.330	−7.991
217.	DHI-217	3.122	−7.435	−7.693
218.	DHI-218	3.124	−6.847	−7.413
219.	DHI-219	3.126	–	–
220.	DHI-220	3.128	−6.696	−7.706
221.	DHI-221	3.131	−7.021	−7.639
222.	DHI-222	3.133	−7.215	−7.653
223.	DHI-223	3.135	−7.695	−7.904
224.	DHI-224	3.137	−7.839	−8.125
225.	DHI-225	3.139	−7.522	−7.963

(continued)

Table C.1 (continued)

S. No.	Code	StalAge (ka BP)	$\delta^{18}O$ (‰)	$\delta^{13}C$ (‰)
226.	DHI-226	3.142	−6.828	−7.832
227.	DHI-227	3.144	–	–
228.	DHI-228	3.146	−7.206	−7.776
229.	DHI-229	3.148	−6.464	−7.395
230.	DHI-230	3.150	−6.980	−7.617
231.	DHI-231	3.152	−6.478	−7.508
232.	DHI-232	3.154	−6.683	−6.977
233.	DHI-233	3.156	−6.031	−6.830
234.	DHI-234	3.158	−6.392	−7.119
235.	DHI-235	3.161	−6.681	−7.645
236.	DHI-236	3.163	−7.279	−8.585
237.	DHI-237	3.165	−7.374	−8.875
238.	DHI-238	3.166	−7.370	−8.897
239.	DHI-239	3.168	−6.941	−8.757
240.	DHI-240	3.170	−7.085	−8.776
241.	DHI-241	3.172	–	–
242.	DHI-242	3.174	−6.812	−8.150
243.	DHI-243	3.176	−6.938	−8.396
244.	DHI-244	3.178	−7.103	−7.980
245.	DHI-245	3.179	−7.004	−7.875
246.	DHI-246	3.181	–	–
247.	DHI-247	3.183	–	–
248.	DHI-248	3.185	−7.388	−8.134
249.	DHI-249	3.186	−7.156	−8.089
250.	DHI-250	3.188	−7.169	−7.751
251.	DHI-251	3.190	−7.111	−8.371
252.	DHI-252	3.191	−7.383	−7.711
253.	DHI-253	3.193	−7.240	−8.155
254.	DHI-254	3.195	−6.967	−7.971
255.	DHI-255	3.196	−7.199	−8.081
256.	DHI-256	3.198	−7.263	−8.277
257.	DHI-257	3.199	–	–
258.	DHI-258	3.201	−6.840	−7.980
259.	DHI-259	3.203	–	–
260.	DHI-260	3.204	−7.168	−8.100
261.	DHI-261	3.206	–	–
262.	DHI-262	3.207	−7.113	−8.163
263.	DHI-263	3.209	−6.963	−8.424
264.	DHI-264	3.211	−7.232	−8.805
265.	DHI-265	3.212	−7.011	−8.143

(continued)

Table C.1 (continued)

S. No.	Code	StalAge (ka BP)	$\delta^{18}O$ (‰)	$\delta^{13}C$ (‰)
266.	DHI-266	3.214	−7.328	−7.421
267.	DHI-267	3.215	−6.880	−7.143
268.	DHI-268	3.217	−6.372	−6.285
269.	DHI-269	3.218	−6.482	−6.781
270.	DHI-270	3.220	−6.420	−6.694
271.	DHI-271	3.221	−7.372	−7.207
272.	DHI-272	3.223	−6.304	−6.348
273.	DHI-273	3.224	−6.839	−7.461
274.	DHI-274	3.226	−6.567	−7.889
275.	DHI-275	3.227	−6.851	−8.407
276.	DHI-276	3.228	−6.619	−8.157
277.	DHI-277	3.230	−6.744	−8.201
278.	DHI-278	3.231	−6.991	−7.909
279.	DHI-279	3.232	−6.692	−7.766
280.	DHI-280	3.233	−7.140	−8.249
281.	DHI-281	3.233	−6.694	−8.182
282.	DHI-282	3.234	−6.863	−8.143
283.	DHI-283	3.234	−7.626	−7.803
284.	DHI-284	3.235	−7.920	−9.278
285.	DHI-285	3.236	−7.039	−9.398
286.	DHI-286	3.236	−7.456	−9.516
287.	DHI-287	3.237	−6.685	−8.528
288.	DHI-288	3.237	−6.563	−7.811
289.	DHI-289	3.238	−7.427	−9.531
290.	DHI-290	3.238	−7.340	−9.607
291.	DHI-291	3.238	−6.985	−8.579
292.	DHI-292	3.239	−7.235	−9.310
293.	DHI-293	3.239	−8.120	−9.434
294.	DHI-294	3.239	−8.134	−9.624
295.	DHI-295	3.239	−7.193	−9.566
296.	DHI-296	3.239	−7.098	−9.290
297.	DHI-297	3.239	−7.130	−8.190
298.	DHI-298	3.239	−7.720	−8.447
299.	DHI-299	3.239	−7.732	−8.198
300.	DHI-300	3.239	−7.713	−8.185
301.	DHI-301	3.239	−7.313	−8.219
302.	DHI-302	3.239	−6.938	−8.002
303.	DHI-303	3.239	−7.146	−8.145
304.	DHI-304	3.239	−6.738	−8.018
305.	DHI-305	3.239	−6.893	−8.019

(continued)

Table C.1 (continued)

S. No.	Code	StalAge (ka BP)	$\delta^{18}O$ (‰)	$\delta^{13}C$ (‰)
306.	DHI-306	3.239	−6.635	−7.821
307.	DHI-307	3.239	−6.381	−7.981
308.	DHI-308	3.239	−6.622	−8.066
309.	DHI-309	3.239	−7.182	−8.153
310.	DHI-310	3.239	−7.299	−8.139
311.	DHI-311	3.239	–	–
312.	DHI-312	3.239	−7.017	−8.180
313.	DHI-313	3.239	−6.822	−7.993
314.	DHI-314	3.239	–	–
315.	DHI-315	3.239	−7.216	−7.949
316.	DHI-316	3.239		
317.	DHI-317	3.239	−6.519	−8.050
318.	DHI-318	3.239	−6.374	−8.046
319.	DHI-319	3.240	−6.504	−7.767
320.	DHI-320	3.240	−6.827	−7.757
321.	DHI-321	3.240	–	–
322.	DHI-322	3.241	–	–
323.	DHI-323	3.242	–	–
324.	DHI-324	3.243	−7.022	−7.772
325.	DHI-325	3.244	–	–
326.	DHI-326	3.246	−6.608	−6.857
327.	DHI-327	3.247	−6.049	−6.150
328.	DHI-328	3.250	−6.023	−5.620
329.	DHI-329	3.254	−7.475	−6.844
330.	DHI-330	3.258	−6.830	−5.582
331.	DHI-331	3.262	−6.953	−5.512
332.	DHI-332	3.267	−8.035	−7.244
333.	DHI-333	3.272	−7.329	−6.466
334.	DHI-334	3.277	−7.185	−6.268
335.	DHI-335	3.282	−7.158	−6.198
336.	DHI-336	3.288	−7.098	−5.690
337.	DHI-337	3.294	−6.873	−5.135
338.	DHI-338	3.300	−6.955	−5.447
339.	DHI-339	3.306	−6.941	−5.486
340.	DHI-340	3.313	−7.225	−5.855
341.	DHI-341	3.320	−6.907	−5.053
342.	DHI-342	3.327	−6.467	−4.319
343.	DHI-343	3.335	−6.573	−6.438
344.	DHI-344	3.342	−6.467	−4.820
345.	DHI-345	3.350	−6.682	−5.484

(continued)

Table C.1 (continued)

S. No.	Code	StalAge (ka BP)	$\delta^{18}O$ (‰)	$\delta^{13}C$ (‰)
346.	DHI-346	3.358	−6.976	−6.068
347.	DHI-347	3.366	–	–
348.	DHI-348	3.375	−6.878	−5.464
349.	DHI-349	3.384	−6.863	−5.433
350.	DHI-350	3.393	−6.451	−5.371
351.	DHI-351	3.402	−6.213	−5.402
352.	DHI-352	3.411	−6.031	−5.018
353.	DHI-353	3.421	−6.659	−5.676
354.	DHI-354	3.431	−6.504	−4.897
355.	DHI-355	3.441	−6.477	−5.297
356.	DHI-356	3.451	−6.882	−4.042
357.	DHI-357	3.462	−7.105	−3.912
358.	DHI-358	3.473	−6.955	−2.934
359.	DHI-359	3.484	−7.322	−2.920
360.	DHI-360	3.496	−7.288	−5.945
361.	DHI-361	3.507	−6.948	−4.080
362.	DHI-362	3.519	−7.086	−3.603
363.	DHI-363	3.531	−7.260	−3.099
364.	DHI-364	3.543	−7.620	−3.117
365.	DHI-365	3.556	−7.909	−3.513
366.	DHI-366	3.569	−7.800	−3.680
367.	DHI-367	3.581	−8.496	−3.661
368.	DHI-368	3.594	−7.613	−3.513
369.	DHI-369	3.607	−6.621	−3.499
370.	DHI-370	3.620	−6.628	−3.810
371.	DHI-371	3.633	−7.942	−3.880
372.	DHI-372	3.646	−7.459	−3.767
373.	DHI-373	3.659	−7.321	−3.494
374.	DHI-374	3.672	−8.080	−3.604
375.	DHI-375	3.685	−7.769	−3.511
376.	DHI-376	3.698	−7.515	−3.698
377.	DHI-377	3.710	−7.631	−3.286
378.	DHI-378	3.723	−8.101	−2.872
379.	DHI-379	3.735	−9.080	−3.611
380.	DHI-380	3.747	−8.763	−3.861
381.	DHI-381	3.759	−9.230	−4.103
382.	DHI-382	3.771	−9.240	−4.178
383.	DHI-383	3.783	−8.826	−5.055
384.	DHI-384	3.794	−8.707	−5.501
385.	DHI-385	3.805	−8.321	−5.578

(continued)

Table C.1 (continued)

S. No.	Code	StalAge (ka BP)	$\delta^{18}O$ (‰)	$\delta^{13}C$ (‰)
386.	DHI-386	3.816	−8.075	−6.270
387.	DHI-387	3.826	−8.210	−6.316
388.	DHI-388	3.837	−7.814	−6.410
389.	DHI-389	3.847	−8.044	−6.370
390.	DHI-390	3.858	−7.927	−6.190
391.	DHI-391	3.868	−7.825	−6.583
392.	DHI-392	3.878	−7.340	−5.721
393.	DHI-393	3.888	−7.097	−6.453
394.	DHI-394	3.898	−7.084	−5.782
395.	DHI-395	3.908	−7.228	−6.004
396.	DHI-396	3.918	−7.429	−6.091
397.	DHI-397	3.928	−7.199	−5.763
398.	DHI-398	3.938	−7.523	−5.944
399.	DHI-399	3.948	−7.516	−6.100
400.	DHI-400	3.958	−7.707	−6.116
401.	DHI-401	3.968	−7.800	−6.195
402.	DHI-402	3.978	−7.657	−6.284
403.	DHI-403	3.989	−7.648	−6.261
404.	DHI-404	3.999	−7.770	−6.326
405.	DHI-405	4.009	−7.821	−6.024
406.	DHI-406	4.020	−7.608	−5.807
407.	DHI-407	4.030	−7.455	−5.973
408.	DHI-408	4.041	−7.368	−5.912
409.	DHI-409	4.051	−7.521	−6.076
410.	DHI-410	4.062	−7.302	−6.041
411.	DHI-411	4.072	−7.316	−5.911
412.	DHI-412	4.083	−7.280	−5.977
413.	DHI-413	4.094	−7.197	−5.704
414.	DHI-414	4.104	−7.727	−6.129
415.	DHI-415	4.115	−7.754	−5.757

Annexure D

See Table D.1.

Table D.1 $\delta^{18}O$ and $\delta^{13}C$ values in CH-1

S. No.	Code	StalAge (kaBP)	$\delta^{18}O$ (‰)	$\delta^{13}C$ (‰)
1.	CHI-1	1622.18	−2.71	−5.27
2.	CHI-2	1624.54	−3.604	−5.606
3.	CHI-3	1626.91	−3.94	−5.93
4.	CHI-4	1634.04	−4.44	−6.86
5.	CHI-5	1636.44	−4.67	−7.35
6.	CHI-6	1638.84	−4.67	−7.35
7.	CHI-7	1643.07	−4.995	−8.831
8.	CHI-8	1646.12	−4.61	−7
9.	CHI-9	1648.57	−4.68	−6.83
10.	CHI-10	1652.28	−4.68	−6.9
11.	CHI-11	1656.34	−5.11	−7.25
12.	CHI-12	1661.09	−4.928	−6.577
13.	CHI-13	1665.91	−5.7	−8.04
14.	CHI-14	1668.51	−5.44	−7.6
15.	CHI-15	1671.46	−4.61	−7.56
16.	CHI-16	1676.07	−5.28	−7.42
17.	CHI-17	1678.73	−4.94	−6.38
18.	CHI-18	1684.74	−5.04	−6.5
19.	CHI-19	1687.42	−4.63	−6.04
20.	CHI-20	1689.76	−5.28	−7.14
21.	CHI-21	1692.11	−5.26	−7.51
22.	CHI-22	1694.46	−4.981	−7.01
23.	CHI-23	1698.14	−5.2	−7.29
24.	CHI-24	1700.47	−5.59	−7.42
25.	CHI-25	1703.14	−5.32	−6.32

(continued)

A. K. Singh, *High Resolution Palaeoclimatic Changes in Selected Sectors of the Indian Himalaya by Using Speleothems*, Springer Theses,
https://doi.org/10.1007/978-3-319-73597-9

Table D.1 (continued)

S. No.	Code	StalAge (kaBP)	$\delta^{18}O$ (‰)	$\delta^{13}C$ (‰)
26.	CHI-26	1705.79	−4.71	−6.89
27.	CHI-27	1709.09	−4.7	−6.78
28.	CHI-28	1711.71	−4.63	−6.58
29.	CHI-29	1714.65	−4.56	−6.79
30.	CHI-30	1717.87	−5.09	−6.79
31.	CHI-31	1720.11	−4.83	−6.95
32.	CHI-32	1722.34	−4.84	−6.97
33.	CHI-33	1726.10	−5.09	−6.96
34.	CHI-34	1728.57	−4.99	−7.04
35.	CHI-35	1731.92	−4.93	−6.62
36.	CHI-36	1734.92	−5.39	−7.26
37.	CHI-37	1737.29	−5.07	−7.19
38.	CHI-38	1739.04	−3.29	−6.53
39.	CHI-39	1740.79	−4.663	−6.62
40.	CHI-40	1742.52	−3.79	−7.01
41.	CHI-41	1744.23	−4.99	−7.45
42.	CHI-42	1745.94	−4.95	−7.29
43.	CHI-43	1747.91	−5.103	−7.129
44.	CHI-44	1750.70	−5.501	−8.38
45.	CHI-45	1752.91	−5.105	−7.13
46.	CHI-46	1755.65	−5.133	−7.201
47.	CHI-47	1759.72	−4.904	−6.941
48.	CHI-48	1761.60	−4.833	−6.938
49.	CHI-49	1763.74	−4.733	−6.565
50.	CHI-50	1765.60	−4.969	−6.624
51.	CHI-51	1767.46	−4.894	−6.561
52.	CHI-52	1769.30	−5.035	−6.464
53.	CHI-53	1771.15	−5.009	−6.689
54.	CHI-54	1774.82	−5.014	−6.68
55.	CHI-55	1776.65	−5.02	−6.706
56.	CHI-56	1778.22	−5.05	−6.678
57.	CHI-57	1780.05	−5.107	−6.68
58.	CHI-58	1781.62	−4.933	−6.839
59.	CHI-59	1783.19	−4.863	−6.855
60.	CHI-60	1784.76	−4.485	−6.117
61.	CHI-61	1786.33	−4.58	−6.36
62.	CHI-62	1787.90	−4.83	−6.91
63.	CHI-63	1790.26	−5.29	−7.09
64.	CHI-64	1792.62	−4.91	−7.03
65.	CHI-65	1794.99	−5.02	−6.82

(continued)

Table D.1 (continued)

S. No.	Code	StalAge (kaBP)	$\delta^{18}O$ (‰)	$\delta^{13}C$ (‰)
66.	CHI-66	1797.09	−5.21	−7.02
67.	CHI-67	1798.68	−5.27	−7.39
68.	CHI-68	1800.53	−5.67	−8.25
69.	CHI-69	1803.70	−4.23	−6.35
70.	CHI-70	1805.56	−4.37	−6.13
71.	CHI-71	1807.16	−4.47	−6.53
72.	CHI-72	1808.76	−4.6	−6.47
73.	CHI-73	1810.36	−5.19	−7.46
74.	CHI-74	1813.03	−4.99	−7.43
75.	CHI-75	1814.91	−4.34	−6.34
76.	CHI-76	1817.33	−4.3	−6.27
77.	CHI-77	1819.21	−4.22	−6.17
78.	CHI-78	1820.84	−4.33	−6.91
79.	CHI-79	1822.46	−3.42	−5.67
80.	CHI-80	1824.09	−2.965	−5.371
81.	CHI-81	1825.99	−3.68	−7.55
82.	CHI-82	1827.90	−3.622	−6.839
83.	CHI-83	1830.09	−3.6	−6.454
84.	CHI-84	1831.74	−3.75	−6.28
85.	CHI-85	1833.39	−4.31	−6.6
86.	CHI-86	1835.04	−4.1	−6.47
87.	CHI-87	1836.70	−4.16	−6.42
88.	CHI-88	1838.36	−4.26	−6.04
89.	CHI-89	1840.03	−4.53	−6.22
90.	CHI-90	1842.82	−4.56	−5.81
91.	CHI-91	1844.50	−4.697	−6.458
92.	CHI-92	1846.46	−4.57	−6.43
93.	CHI-93	1850.12	−4.62	−6.39
94.	CHI-94	1852.37	−4.66	−6.59
95.	CHI-95	1854.63	−4.621	−7.376
96.	CHI-96	1858.32	−4.83	−6.54
97.	CHI-97	1860.31	−4.59	−6.45
98.	CHI-98	1862.29	−4.64	−6.53
99.	CHI-99	1864.29	–	–
100.	CHI-100	1866.28	−4.62	−6.88
101.	CHI-101	1868.27	−4.67	−7.21
102.	CHI-102	1870.27	−4.76	−7.12
103.	CHI-103	1872.83	−5.92	−7.85
104.	CHI-104	1876.26	−4.2	−6.78
105.	CHI-105	1878.54	−4.17	−6.66

(continued)

Table D.1 (continued)

S. No.	Code	StalAge (kaBP)	$\delta^{18}O$ (‰)	$\delta^{13}C$ (‰)
106.	CHI-106	1880.81	−3.92	−5.98
107.	CHI-107	1884.23	−4.63	−7.26
108.	CHI-108	1887.07	−4.61	−6.59
109.	CHI-109	1889.34	−4.46	−6.44
110.	CHI-110	1892.74	−3.96	−6.06
111.	CHI-111	1896.13	−3.97	−6.24
112.	CHI-112	1898.38	−4.41	−6.52
113.	CHI-113	1900.07	−4.36	−6.61
114.	CHI-114	1901.76	−3.72	−5.74
115.	CHI-115	1903.44	−3.70	−5.41
116.	CHI-116	1905.12	–	–
117.	CHI-117	1906.80	−3.86	−5.71
118.	CHI-118	1908.48	−3.46	−5.39
119.	CHI-119	1910.43	−3.68	−5.62
120.	CHI-120	1912.39	−4.57	−6.57
121.	CHI-121	1914.90	−4.63	−6.22
122.	CHI-122	1916.85	−4.63	−6.22
123.	CHI-123	1919.35	−4.55	−5.95
124.	CHI-124	1921.86	–	–
125.	CHI-125	1924.36	−3.88	−5.83
126.	CHI-126	1926.86	−3.95	−6.01
127.	CHI-127	1929.09	−3.48	−5.65
128.	CHI-128	1931.04	−3.8	−6.68
129.	CHI-129	1933.26	–	–
130.	CHI-130	1935.48	−4.35	−7.1
131.	CHI-131	1937.43	−4.29	−6.97
132.	CHI-132	1940.22	−4.42	−7.5
133.	CHI-133	1942.17	−4.11	−7.49
134.	CHI-134	1945.79	−3.99	−7.4
135.	CHI-135	1949.98	−4.23	−7.66

Annexure E

See Table E.1.

Table E.1 $\delta^{18}O$ and $\delta^{13}C$ values in TCS

S. No	Code	StalAge (kaBP)	$\delta^{18}O$ (‰)	$\delta^{13}C$ (‰)
1.	TCI-1	1.580	−8.114	−0.721
2.	TCI-2	1.592	−8.727	−0.596
3.	TCI-3	1.601	−8.083	−2.124
4.	TCI-4	1.613	−8.909	−2.854
5.	TCI-5	1.630	−9.439	−2.799
6.	TCI-6	1.651	−9.095	−4.17
7.	TCI-7	1.674	−9.099	−1.883
8.	TCI-8	1.693	−9.55	−2.028
9.	TCI-9	1.714	−9.302	−2.357
10.	TCI-10	1.736	−9.603	−1.686
11.	TCI-11	1.760	−9.285	−2.485
12.	TCI-12	1.784	−9.326	−2.225
13.	TCI-13	1.809	−9.334	−2.982
14.	TCI-14	1.834	−8.464	−3.002
15.	TCI-15	1.859	−8.781	−3.332
16.	TCI-16	1.884	−8.358	−6.648
17.	TCI-17	1.910	−8.04	−7.129
18.	TCI-18	1.935	−9.816	−7.579
19.	TCI-19	1.960	−9.702	−7.185
20.	TCI-20	1.984	−9.86	−7.675
21.	TCI-21	2.008	−10.142	−9.132
22.	TCI-22	2.031	−10.42	−9.433
23.	TCI-23	2.053	−9.9	−9.097
24.	TCI-24	2.074	−9.267	−8.464
25.	TCI-25	2.095	−9.416	−7.132
26.	TCI-26	2.113	−9.355	−7.909

(continued)

A. K. Singh, *High Resolution Palaeoclimatic Changes in Selected Sectors of the Indian Himalaya by Using Speleothems*, Springer Theses,
https://doi.org/10.1007/978-3-319-73597-9

Table E.1 (continued)

S. No	Code	StalAge (kaBP)	$\delta^{18}O$ (‰)	$\delta^{13}C$ (‰)
27.	TCI-27	2.129	−10.368	−7.57
28.	TCI-28	2.142	−10.426	−7.902
29.	TCI-29	2.156	−9.016	−8.010
30.	TCI-30	2.171	−9.111	−8.084
31.	TCI-31	2.190	−8.743	−7.811
32.	TCI-32	2.250	−9.68	−4.674
33.	TCI-33	2.265	−9.095	−5.723
34.	TCI-34	2.282	−9.225	−6.185
35.	TCI-35	2.298	−9.509	−6.385
36.	TCI-36	2.320	−9.421	−5.119
37.	TCI-37	2.351	−9.44	−4.539
38.	TCI-38	2.385	−9.018	−3.913
39.	TCI-39	2.423	−9.273	−3.891
40.	TCI-40	2.461	−9.544	−4.024
41.	TCI-41	2.502	−9.742	−4.396
42.	TCI-42	2.542	−9.792	−4.224
43.	TCI-43	2.584	−9.621	−3.492
44.	TCI-44	2.626	−9.247	−2.357
45.	TCI-45	2.669	−9.694	−1.415
46.	TCI-46	2.712	−10.181	−0.845
47.	TCI-47	2.755	−10.102	−0.659
48.	TCI-48	2.799	−9.956	−0.196
49.	TCI-49	2.842	−9.296	−2.311
50.	TCI-50	2.886	−9.181	−3.717
51.	TCI-51	2.929	−9.891	−1.646
52.	TCI-52	2.972	−9.121	−1.836
53.	TCI-53	3.014	−8.979	−1.344
54.	TCI-54	3.056	−10.215	−3.4
55.	TCI-55	3.098	−9.966	−2.845
56.	TCI-56	3.138	−9.88	−2.707
57.	TCI-57	3.178	−9.927	−2.438
58.	TCI-58	3.216	−10.056	−1.993
59.	TCI-59	3.252	−9.346	−1.597
60.	TCI-60	3.285	−9.733	−2.002
61.	TCI-61	3.320	−9.181	−0.198
62.	TCI-62	3.349	−9.1	−0.536
63.	TCI-63	3.367	−8.683	−0.929
64.	TCI-64	3.377	−8.74	−1.432
65.	TCI-65	3.391	−8.507	−0.924
66.	TCI-66	3.395	−8.119	−0.727

(continued)

Table E.1 (continued)

S. No	Code	StalAge (kaBP)	$\delta^{18}O$ (‰)	$\delta^{13}C$ (‰)
67.	TCI-67	3.401	−9.026	−0.52
68.	TCI-68	3.407	−8.561	−0.33
69.	TCI-69	3.413	−9.439	−1.168
70.	TCI-70	3.420	−9.233	−1.021
71.	TCI-71	3.426	−9.182	−0.788
72.	TCI-72	3.432	−8.886	−0.982
73.	TCI-73	3.438	−9.069	−1.147
74.	TCI-74	3.444	−8.659	−1.832
75.	TCI-75	3.450	−8.625	−1.486
76.	TCI-76	3.457	−8.441	−2.681
77.	TCI-77	3.464	−9.599	−3.774
78.	TCI-78	3.471	−9.448	−4.349
79.	TCI-79	3.478	−8.68	−5.196
80.	TCI-80	3.485	−10.332	−5.528
81.	TCI-81	3.492	−9.753	−7.126
82.	TCI-82	3.499	−9.204	−5.899
83.	TCI-83	3.506	−10.137	−6.887
84.	TCI-84	3.513	−9.926	−7.585
85.	TCI-85	3.520	−9.683	−8.214
86.	TCI-86	3.527	−10.255	−8.049
87.	TCI-87	3.534	−9.039	−6.834
88.	TCI-88	3.542	−8.835	−6.761
89.	TCI-89	3.549	−9.161	−7.396
90.	TCI-90	3.556	−10.137	−6.854
91.	TCI-91	3.562	−8.904	−7.684
92.	TCI-92	3.568	−8.975	−9.545
93.	TCI-93	3.573	−9.275	−9.208
94.	TCI-94	3.577	−8.72	−7.654
95.	TCI-95	3.589	−9.173	−8.109
96.	TCI-96	3.596	−9.537	−9.311
97.	TCI-97	3.604	−9.469	−9.413
98.	TCI-98	3.612	−8.948	−9.324
99.	TCI-99	3.621	−10.09	−9.445
100.	TCI-100	3.630	−9.946	−8.693
101.	TCI-101	3.639	−10.118	−10.377
102.	TCI-102	3.649	−9.777	−10.064
103.	TCI-103	3.660	−9.995	−10.247
104.	TCI-104	3.671	−9.961	−10.795
105.	TCI-105	3.683	−10.39	−10.879
106.	TCI-106	3.694	−10.366	−10.681

(continued)

Table E.1 (continued)

S. No	Code	StalAge (kaBP)	$\delta^{18}O$ (‰)	$\delta^{13}C$ (‰)
107.	TCI-107	3.706	−9.862	−10.777
108.	TCI-108	3.718	−10.318	−10.248
109.	TCI-109	3.730	−10.203	−10.063
110.	TCI-110	3.743	−9.834	−9.72
111.	TCI-111	3.755	−9.509	−9.035
112.	TCI-112	3.767	−9.842	−9.536
113.	TCI-113	3.780	−10.109	−9.125
114.	TCI-114	3.792	−10.457	−8.802
115.	TCI-115	3.804	−10.495	−8.625
116.	TCI-116	3.816	−9.632	−7.85
117.	TCI-117	3.828	−9.53	−9.212
118.	TCI-118	3.839	−10.078	−8.327
119.	TCI-119	3.850	−9.247	−8.915
120.	TCI-120	3.860	−10.174	−7.529
121.	TCI-121	3.871	−10.011	−7.98
122.	TCI-122	3.880	−9.873	−8.775
123.	TCI-123	3.889	−9.933	−10.57
124.	TCI-124	3.898	−9.053	−8.703
125.	TCI-125	3.907	−9.78	−8.521
126.	TCI-126	3.915	–	–
127.	TCI-127	3.923	–	–
128.	TCI-128	3.929	–	–
129.	TCI-129	3.944	–	–
130.	TCI-130	3.950	–	–

Annexure F

See Table F.1.

Table F.1 $\delta^{18}O$ and $\delta^{13}C$ values in BR-1

S. No.	Code	StalAge (kaBP)	$\delta^{18}O$ (‰)	$\delta^{13}C$ (‰)
1.	BRI-1	0.168	−8.848	−12.187
2.	BRI-2	0.211	−8.709	−11.8
3.	BRI-3	0.255	−9.038	−10.264
4.	BRI-4	0.296	−9.052	−10.801
5.	BRI-5	0.336	−7.691	−10.184
6.	BRI-6	0.377	−9.358	−10.13
7.	BRI-7	0.422	−9.253	−9.164
8.	BRI-8	0.467	−8.945	−9.189
9.	BRI-9	0.510	−9.528	−8.877
10.	BRI-10	0.550	−8.845	−9.776
11.	BRI-11	0.591	−8.924	−9.916
12.	BRI-12	0.633	−9.526	−9.317
13.	BRI-13	0.677	−9.825	−9.454
14.	BRI-14	0.722	−9.039	−9.623
15.	BRI-15	0.768	−9.411	−10.1
16.	BRI-16	0.814	−8.801	−10.174
17.	BRI-17	0.859	−8.848	−9.27
18.	BRI-18	0.905	−9.094	−10.097
19.	BRI-19	0.952	−9.205	−10.456
20.	BRI-20	0.999	−9.157	−10.048
21.	BRI-21	1.045	−8.876	−9.895
22.	BRI-22	1.091	−9.423	−9.593
23.	BRI-23	1.135	−9.105	−9.51
24.	BRI-24	1.178	−9.348	−9.72
25.	BRI-25	1.221	−8.5	−10.368
26.	BRI-26	1.265	−9.197	−10.026

(continued)

A. K. Singh, *High Resolution Palaeoclimatic Changes in Selected Sectors of the Indian Himalaya by Using Speleothems*, Springer Theses,
https://doi.org/10.1007/978-3-319-73597-9

Table F.1 (continued)

S. No.	Code	StalAge (kaBP)	$\delta^{18}O$ (‰)	$\delta^{13}C$ (‰)
27.	BRI-27	1.310	−8.315	−10.47
28.	BRI-28	1.358	−8.571	−10.361
29.	BRI-29	1.407	−7.372	−11.038
30.	BRI-30	1.457	−7.4	−10.63
31.	BRI-31	1.506	−8.189	−10.142
32.	BRI-32	1.551	−9.129	−10.062
33.	BRI-33	1.595	−8.428	−10.109
34.	BRI-34	1.638	−8.967	−10.287
35.	BRI-35	1.682	−8.02	−10.229
36.	BRI-36	1.728	−8.331	−10.296
37.	BRI-37	1.775	−8.764	−10.73
38.	BRI-38	1.823	−9.115	−10.522
39.	BRI-39	1.869	−8.402	−7.632
40.	BRI-40	1.912	−9.612	−8.327
41.	BRI-41	1.955	−8.274	−8.298
42.	BRI-42	1.998	−7.659	−8.624
43.	BRI-43	2.043	−7.895	−8.564
44.	BRI-44	2.089	−8.958	−8.572
45.	BRI-45	2.137	−8.691	−8.075
46.	BRI-46	2.183	−8.813	−8.383
47.	BRI-47	2.228	−8.242	−8.441
48.	BRI-48	2.271	−8.918	−7.634
49.	BRI-49	2.314	−9.028	−8.243
50.	BRI-50	2.358	−9.075	−6.957
51.	BRI-51	2.403	−8.745	−8.016
52.	BRI-52	2.449	−9.278	−8.71
53.	BRI-53	2.495	−10.777	−9.648
54.	BRI-54	2.541	−9.67	−8.789
55.	BRI-55	2.587	−9.006	−8.321
56.	BRI-56	2.632	−10.272	−7.38
57.	BRI-57	2.677	−9.661	−7.788
58.	BRI-58	2.721	−7.433	−7.606
59.	BRI-59	2.767	−9.397	−7.866
60.	BRI-60	2.813	−9.102	−8.48
61.	BRI-61	2.859	−9.218	−8.333
62.	BRI-62	2.904	−9.577	−9.414
63.	BRI-63	2.947	−7.975	−8.835
64.	BRI-64	2.991	−9.099	−9.254
65.	BRI-65	3.035	−9.647	−9.743
66.	BRI-66	3.080	−9.318	−9.46

(continued)

Table F.1 (continued)

S. No.	Code	StalAge (kaBP)	$\delta^{18}O$ (‰)	$\delta^{13}C$ (‰)
67.	BRI-67	3.124	−8.632	−7.679
68.	BRI-68	3.169	−9.127	−9.165
69.	BRI-69	–	–	–
70.	BRI-70	3.260	−9.727	−9.155
71.	BRI-71	3.307	−8.957	−9.171
72.	BRI-72	3.355	−10.192	−9.86
73.	BRI-73	3.402	−10.169	−8.533
74.	BRI-74	3.447	−8.241	−8.688
75.	BRI-75	3.490	−8.787	−9.36
76.	BRI-76	3.533	−9.63	−10.1
77.	BRI-77	3.576	−8.517	−7.516
78.	BRI-78	3.620	−8.313	−8.418
79.	BRI-79	3.664	−9.722	−8.367
80.	BRI-80	3.709	−9.857	−8.59
81.	BRI-81	3.754	−9.64	−6.96
82.	BRI-82	3.799	−9.77	−7.493
83.	BRI-83	3.843	−9.234	−8.824
84.	BRI-84	3.887	–	–
85.	BRI-85	3.931	−8.895	−8.467
86.	BRI-86	3.975	−8.409	−8.127
87.	BRI-87	4.020	−10.637	−9.51
88.	BRI-88	4.066	−9.955	−8.453
89.	BRI-89	4.112	−9.183	−7.839
90.	BRI-90	4.157	−8.627	−7.708
91.	BRI-91	4.201	−8.876	−7.086
92.	BRI-92	4.245	−9.416	−6.457
93.	BRI-93	4.289	−9.504	−6.442
94.	BRI-94	4.333	−10.192	−7.182
95.	BRI-95	4.376	−9.153	−6.915
96.	BRI-96	4.420	−9.293	−6.232
97.	BRI-97	4.465	−9.88	−6.002
98.	BRI-98	4.509	−10.457	−6.097
99.	BRI-99	4.553	−8.822	−5.703
100.	BRI-100	4.598	−9.249	−7.79
101.	BRI-101	4.643	−8.681	−6.748
102.	BRI-102	4.687	−10.112	−9.774
103.	BRI-103	4.732	−9.881	−10.13
104.	BRI-104	4.777	−9.324	−9.609
105.	BRI-105	4.822	−9.003	−10.228
106.	BRI-106	4.866	−9.307	−9.49

(continued)

Table F.1 (continued)

S. No.	Code	StalAge (kaBP)	$\delta^{18}O$ (‰)	$\delta^{13}C$ (‰)
107.	BRI-107	4.910	−10.379	−8.996
108.	BRI-108	4.955	−9.231	−9.047
109.	BRI-109	4.999	−10.545	−9.405
110.	BRI-110	5.043	−10.215	−9.736
111.	BRI-111	5.087	−8.777	−9.917
112.	BRI-112	5.132	−9.147	−9.727
113.	BRI-113	5.176	−9.524	−9.863
114.	BRI-114	5.220	−9.076	−10.448
115.	BRI-115	5.263	−9.383	−10.645
116.	BRI-116	5.307	−9.295	−10.974
117.	BRI-117	5.352	−8.981	−11.182
118.	BRI-118	5.399	−9.012	−10.728
119.	BRI-119	5.446	−9.619	−10.328
120.	BRI-120	5.492	−9.069	−9.827
121.	BRI-121	5.537	−9.758	−9.45
122.	BRI-122	5.581	−9.436	−8.754
123.	BRI-123	5.626	−9.783	−9.783
124.	BRI-124	5.671	−9.057	−9.781
125.	BRI-125	5.715	−10.606	−10.138
126.	BRI-126	5.760	−10.228	−10.156
127.	BRI-127	5.805	−9.712	−11.027
128.	BRI-128	5.849	−9.778	−10.272
129.	BRI-129	5.894	−10.327	−9.266
130.	BRI-130	5.940	−10.408	−8.046
131.	BRI-131	5.985	−10.817	−9.758
132.	BRI-132	6.030	−10.254	−9.506
133.	BRI-133	6.075	−9.832	−9.770
134.	BRI-134	6.119	−9.701	−9.421
135.	BRI-135	6.164	−9.878	−8.991
136.	BRI-136	6.208	−10.246	−8.544
137.	BRI-137	6.253	−9.226	−8.666
138.	BRI-138	6.297	−10.002	−7.849
139.	BRI-139	6.341	−9.818	−6.162
140.	BRI-140	6.385	−9.851	−4.436
141.	BRI-141	6.429	−9.843	−4.328
142.	BRI-142	6.473	−9.805	−5.130
143.	BRI-143	6.517	−9.17	−6.353
144.	BRI-144	6.562	−9.837	−7.253
145.	BRI-145	6.606	−9.704	−7.064
146.	BRI-146	6.650	−10.13	−8.739

(continued)

Table F.1 (continued)

S. No.	Code	StalAge (kaBP)	$\delta^{18}O$ (‰)	$\delta^{13}C$ (‰)
147.	BRI-147	6.695	−9.859	−10.24
148.	BRI-148	6.739	−9.589	−10.334
149.	BRI-149	6.784	−9.742	−9.854
150.	BRI-150	6.828	−9.951	−8.009
151.	BRI-151	6.873	−9.896	−7.116
152.	BRI-152	6.917	−9.603	−6.853
153.	BRI-153	6.961	−10.533	−6.594
154.	BRI-154	7.006	−9.183	−6.315
155.	BRI-155	7.050	–	–
156.	BRI-156	7.095	−9.769	−7.671
157.	BRI-157	7.139	−9.339	−6.204
158.	BRI-158	7.184	−8.681	−7.793
159.	BRI-159	7.228	−9.416	−8.152
160.	BRI-160	7.272	−9.389	−8.298
161.	BRI-161	7.317	−9.714	−8.359
162.	BRI-162	7.361	−9.707	−8.538
163.	BRI-163	7.406	−9.84	−8.809
164.	BRI-164	7.45	−10.952	−9.168
165.	BRI-165	7.494	−10.698	−7.214
166.	BRI-166	7.539	−10.195	−7.304
167.	BRI-167	7.583	−9.917	−7.347
168.	BRI-168	7.628	−9.698	−6.714
169.	BRI-169	7.672	−10.071	−6.798
170.	BRI-170	7.717	−10.047	−6.633
171.	BRI-171	7.761	−9.437	−5.332
172.	BRI-172	7.805	−9.891	−1.045
173.	BRI-173	7.850	−9.255	−1.667
174.	BRI-174	7.894	−8.909	−3.675
175.	BRI-175	7.939	−10.106	−8.231
176.	BRI-176	7.983	−10.314	−10.55
177.	BRI-177	8.028	−10.164	−9.652
178.	BRI-178	8.072	−9.002	−8.657
179.	BRI-179	8.116	−8.548	−8.438
180.	BRI-180	8.160	−9.051	−7.55
181.	BRI-181	8.205	−9.334	−7.734
182.	BRI-182	8.249	−9.851	−8.918
183.	BRI-183	8.293	−9.661	−7.922
184.	BRI-184	8.338	−9.226	−6.977
185.	BRI-185	8.382	−9.608	−6.787
186.	BRI-186	8.427	−10.359	−7.667

(continued)

Table F.1 (continued)

S. No.	Code	StalAge (kaBP)	$\delta^{18}O$ (‰)	$\delta^{13}C$ (‰)
187.	BRI-187	8.471	−9.118	−6.962
188.	BRI-188	8.516	−8.756	−7.184
189.	BRI-189	8.560	−10.006	−8.961
190.	BRI-190	8.605	−9.996	−8.113
191.	BRI-191	8.649	−9.747	−6.174
192.	BRI-192	8.694	−8.928	−4.417
193.	BRI-193	8.738	−10.56	−5.758
194.	BRI-194	8.783	−8.76	−7.748
195.	BRI-195	8.827	−8.877	−7.353
196.	BRI-196	8.872	−8.656	−6.746
197.	BRI-197	8.916	−11.178	−6.766
198.	BRI-198	8.961	−9.844	−7.502
199.	BRI-199	9.006	−9.319	−8.82
200.	BRI-200	9.051	−9.272	−8.883
201.	BRI-201	9.096	−8.681	−9.098
202.	BRI-202	9.142	−9.391	−9.728
203.	BRI-203	9.187	−10.063	−9.769
204.	BRI-204	9.232	−10.615	−9.979
205.	BRI-205	9.277	−9.01	−7.003
206.	BRI-206	9.323	−10.136	−9.626
207.	BRI-207	9.368	−9.415	−9.262
208.	BRI-208	9.413	−8.74	−8.962
209.	BRI-209	9.459	−7.868	−8.731
210.	BRI-210	9.504	−8.94	−8.892
211.	BRI-211	9.549	−9.532	−8.795
212.	BRI-212	9.594	−9.793	−8.79
213.	BRI-213	9.640	−9.92	−9.007
214.	BRI-214	9.685	−10.346	−9.191
215.	BRI-215	9.730	−10.382	−8.762
216.	BRI-216	9.775	−10.646	−8.238
217.	BRI-217	9.820	−9.649	−7.657
218.	BRI-218	9.865	−9.256	−7.333
219.	BRI-219	9.910	−10.036	−8.411
220.	BRI-220	9.954	−9.982	−6.684
221.	BRI-221	9.999	−9.008	−7.652
222.	BRI-222	10.043	−9.231	−8.715
223.	BRI-223	10.088	−9.312	−9.678
224.	BRI-224	10.132	−9.11	−9.911
225.	BRI-225	10.176	–	–
226.	BRI-226	10.221	−9.392	−7.649

(continued)

Table F.1 (continued)

S. No.	Code	StalAge (kaBP)	$\delta^{18}O$ (‰)	$\delta^{13}C$ (‰)
227.	BRI-227	10.265	−9.544	−7.572
228.	BRI-228	10.310	−10.347	−8.111
229.	BRI-229	10.356	–	–
230.	BRI-230	10.401	−9.522	−6.143
231.	BRI-231	10.446	−10.49	−9.454
232.	BRI-232	10.492	−9.802	−9.687
233.	BRI-233	10.537	−9.204	−8.563
234.	BRI-234	10.582	−9.814	−8.815
235.	BRI-235	10.627	−9.103	−8.609
236.	BRI-236	10.673	−9.433	−6.787
237.	BRI-237	10.719	−9.167	−8.069
238.	BRI-238	10.766	−9.174	−8.476
239.	BRI-239	10.811	−9.653	−8.235
240.	BRI-240	10.855	−9.009	−7.736
241.	BRI-241	10.899	−9.472	−7.994
242.	BRI-242	10.943	−10.656	−8.066
243.	BRI-243	10.987	−10.212	−8.06
244.	BRI-244	11.031	−9.123	−7.725
245.	BRI-245	11.075	−9.341	−9.883
246.	BRI-246	11.119	−9.619	−9.439
247.	BRI-247	11.163	−9.238	−9.196
248.	BRI-248	11.207	−9.199	−9.511
249.	BRI-249	11.251	−9.953	−9.557
250.	BRI-250	11.295	−9.901	−8.75
251.	BRI-251	11.340	−9.869	−8.546
252.	BRI-252	11.385	−9.724	−6.388
253.	BRI-253	11.43	−10.197	−5.966
254.	BRI-254	11.475	−9.618	−8.021
255.	BRI-255	11.519	−10.13	−8.198
256.	BRI-256	11.564	−10.13	−8.198
257.	BRI-257	11.609	−10.312	−7.471
258.	BRI-258	11.654	−9.845	−6.809
259.	BRI-259	11.699	−9.034	−6.399
260.	BRI-260	11.743	−9.769	−5.978
261.	BRI-261	11.788	−9.944	−5.841
262.	BRI-262	11.832	−10.166	−7.106
263.	BRI-263	11.877	−10.285	−6.053
264.	BRI-264	11.921	−10.261	−5.91
265.	BRI-265	11.965	−10.108	−5.793
266.	BRI-266	12.010	−9.742	−5.484

(continued)

Table F.1 (continued)

S. No.	Code	StalAge (kaBP)	$\delta^{18}O$ (‰)	$\delta^{13}C$ (‰)
267.	BRI-267	12.058	−9.578	−4.886
268.	BRI-268	12.106	−9.874	−4.902
269.	BRI-269	12.153	−10.011	−5.179
270.	BRI-270	12.199	−10.096	−4.809
271.	BRI-271	12.248	−10.069	−6.567
272.	BRI-272	12.301	−10.036	−7.319
273.	BRI-273	12.354	−10.049	−7.254
274.	BRI-274	12.401	−9.753	−6.996
275.	BRI-275	12.441	−9.7	−7.177
276.	BRI-276	12.480	−9.179	−7.542
277.	BRI-277	12.521	−9.249	−7.995
278.	BRI-278	12.563	−9.494	−7.929
279.	BRI-279	12.604	−9.633	−7.492
280.	BRI-280	12.646	−9.846	−7.406
281.	BRI-281	12.688	−9.82	−6.781
282.	BRI-282	12.732	−8.999	−7.399
283.	BRI-283	12.777	−9.251	−7.369
284.	BRI-284	12.822	−9.7	−7.346
285.	BRI-285	12.866	−9.582	−7.429
286.	BRI-286	12.911	−9.561	−7.463
287.	BRI-287	12.959	−9.135	−8.042
288.	BRI-288	13.007	−9.017	−8.844
289.	BRI-289	13.055	−8.893	−8.649
290.	BRI-290	13.101	−9.056	−8.761
291.	BRI-291	13.143	−9.343	−8.992
292.	BRI-292	13.180	−9.294	−8.687
293.	BRI-293	13.217	−9.533	−9.143
294.	BRI-294	13.262	−9.579	−9.114
295.	BRI-295	13.314	−9.744	−9.066
296.	BRI-296	13.367	−9.264	−8.878